University of Seville & University of Turin

PhD Thesis

SEMI-INCLUSIVE NEUTRINO-NUCLEUS REACTIONS AT INTERMEDIATE ENERGIES

by

JUAN MANUEL FRANCO PATIÑO

B.S., University of Seville, 2017
M.S., University of Seville, 2018

Supervised by: Juan Antonio Caballero and Maria Benedetta Barbaro

Submitted in partial fulfillment of the

requirements for the degree of

Doctor of Philosophy

2023

Para mi familia,
sin quien otra realidad sería impensable;
y esta realidad, intolerable.

Acknowledgments

Es un placer dedicar unas pocas palabras a todas las personas que me han dado su apoyo y consejo a lo largo de estos últimos cuatro años. Para empezar, me gustaría expresar mi eterna gratitud a mis directores de tesis, Juan Antonio y Maria, por darme la oportunidad de trabajar en un proyecto tan interesante, su continua orientación, apoyo y por un tener siempre *un segundito* para charlar. Siempre me he sentido como en casa tanto en Sevilla como en mis visitas a Turín y ha sido gracias a vosotros.

Quiero extener mis agradecimientos a todos los colaboradores a los que me he encontrado durante estos años, tanto en Sevilla y Madrid como en Turín y Ginebra, haciendo especial mención a Guille y a Raúl, quienes siempre han estado disponibles para discutir ideas y resultados. También quiero dar las gracias a Stephen por echarme un cable con las simulaciones de GENIE y por hacerme un hueco para discutir siempre que podía. Aprovecho también para agradecer por todo lo que he aprendido en el aspecto docente de todos los compañeros que he tenido en las prácticas de Cuántica y a los alumnos por sus preguntas que siempre te hacen mejorar y por su entusiasmo, incluso en los turnos de los viernes por la tarde. También quiero dar las gracias a mis amigos del campus por todos esos largos almuerzos, en especial a Gabri y Miguel.

Por supuesto, nunca habría llegado hasta aquí de no ser por mi familia. Gracias a mis padres, a los que jamás podré pagar su sacrificio para cambiar un futuro incierto en Colombia por una oportunidad en España para mi y para mi hermana. Espero que al leer esto sintáis tanto orgullo como he sentido yo al escribirlo.

Por último, quiero agradecer al instituto Carlos I de Física Teórica y Computacional de Granada el acceso al cluster de superordenadores PROTEUS en el cual se han hecho gran parte de los cálculos numéricos presentados en la tesis y la ayuda económica recibida del Ministerio de Ciencia e Innovación mediante el programa FPI.

Contents

List of Tables

List of Figures

List of Abbreviations

2p2h	.....	Two-particle-two-hole
CC	.....	Charged-current
CCQE	.....	Charged-current quasielastic
CP	.....	Charge-Parity
DIS	.....	Deep inelastic scattering
d.o.f.	.....	Degrees of freedom
EDAD	.....	Energy-dependent A-dependent
EDAI	.....	Energy-dependent A-independent
ED-RMF	.....	Energy-dependent relativistic mean field
FSI	.....	Final-state interactions
IA	.....	Impulse approximation
INC	.....	Intranuclear cascade
IPSM	.....	Independent-particle shell model
IV	.....	Inferred variables
LFG	.....	Local Fermi gas
MC	.....	Montecarlo
MEC	.....	Meson exchange current
NC	.....	Neutral current
NN	.....	Nucleon-nucleon
NO	.....	Natural orbitals
non-QE	.....	Non-quasielastic
PMNS	.....	Portecorvo-Maki-Nakagawa-Sakata
PWIA	.....	Plane-wave impulse approximation
QE	.....	Quasielastic
RDWIA	.....	Relativistic distorted-wave impulse approximation
RFG	.....	Relativistic Fermi gas
RMF	.....	Relativistic mean field
ROP	.....	Relativistic optical potential
RPA	.....	Random phase approximation
RPWIA	.....	Relativistic plane-wave impulse approximation
rROP	.....	Real part of a relativistic optical potential
SF	.....	Spectral function
SM	.....	Standard model
TKI	.....	Transverse kinematic imbalances

Chapter 1

Introduction

Neutrinos are the most abundant massive particles in the universe. When atomic nuclei are created in a star, like our sun, or break apart, like inside a nuclear reactor, neutrinos are created. The existence of neutrinos was proposed by Pauli almost one century ago as an alternative over the violation of energy conservation in β decay. The confirmation of its existence (or to be more precise, the existence of its antiparticle) came almost three decades after it was postulated [1]. Nowadays, the neutrino holds a distinguished place in the physics landscape, both inside and beyond the Standard Model. The main topic of this thesis is the description of a realistic theoretical model of semi-inclusive neutrino-nucleus reactions, namely, processes where a lepton and one ejected nucleon are detected in coincidence after the interaction of a neutrino with a nucleus. The ultimate goal of the thesis is to perform a systematic analysis of all the semi-inclusive neutrino-nucleus experimental data published until 2023 with a realistic, *i.e.* relativistic and quantum mechanical, model of the nuclear dynamics. The analysis, proper understanding and modeling of these reactions will help current and future neutrino oscillation experiments by reducing the systematic uncertainties associated to the modeling of neutrino-nucleus interactions.

This thesis is structured as follows: in this Chapter, an introduction to neutrino oscillations, accelerator-based neutrino experiments and neutrino-nucleus interactions is presented. Chapter 2 is mainly focused in the general definition of a semi-inclusive neutrino-nucleus reaction and the analysis, from a theoretical point of view, of semi-inclusive results using different

models of the nucleus, but neglecting the effects introduced by final state interactions (FSI). Chapter 3 is entirely dedicated to the description of the one-proton knockout process, a type of semi-inclusive reaction, using a fully relativistic and quantum mechanical model of the nuclear dynamics and including final-state interactions, while in Chapter 4 we summarize the current approach used by neutrino event generators to describe semi-inclusive reactions. Different approximations for the description of semi-inclusive reactions are compared with semi-inclusive cross section measurements performed by different international collaborations in Chapter 5. Finally, in Chapter 6 we present a summary and the conclusions of this thesis.

1.1 Neutrino oscillations

Bruno Pontecorvo, while looking for an analogous of neutral kaon mixing [2] for neutrinos in 1957, developed the concept of neutrino-antineutrino transitions [3]. Although no matter-antimatter oscillation has been observed to date in the leptonic sector, the concept formed the foundation of lepton mixing, which was developed by Maki, Nakagawa, and Sakata, on the basis of a neutrino flavour oscillation model by Pontecorvo. The observation of neutrino oscillations [4], which are only possible if neutrinos have mass, implied new physics beyond the Standard Model (SM).

Neutrinos, as particles that interact weakly with matter by exchanging $W^{\pm}$ and Z bosons, have a quantum number called lepton flavour which is the same as the other lepton in their SM doublet: $(\nu_e\ e^-)$, $(\nu_\mu\ \mu^-)$ and $(\nu_\tau\ \tau^-)$. Therefore, neutrinos (and equivalently their antiparticles called antineutrinos which are distinguished from the neutrinos by having opposite signs of chirality and lepton number) can be described by orthonormal flavour eigenstates $|\nu_\alpha\rangle$ with α the flavour of a neutrino (e, μ, τ). These flavour eigenstates do not correspond to neutrino mass eigenstates $|\nu_i\rangle$, *i.e.* neutrino states with definite mass m. Then, the neutrino flavour eigenstates can be expressed as a superposition of states with definite

mass

$$|\nu_\alpha\rangle = \sum_{i=1}^{3} U^*_{\alpha i}|\nu_i\rangle, \tag{1.1}$$

with U a unitary matrix ($UU^\dagger = \mathbb{1}$) denominated the leptonic mixing matrix or PMNS (Portecorvo-Maki-Nakagawa-Sakata) matrix. Eq. (1.1) can be inverted to yield

$$|\nu_i\rangle = \sum_{\alpha=e,\mu,\tau} U_{\alpha i}|\nu_\alpha\rangle. \tag{1.2}$$

The time evolution of each mass eigenstate $|\nu_i\rangle$ can be obtained by applying the time-dependent Schrödinger equation to the state $|\nu_i\rangle$

$$i\hbar\frac{\partial|\nu_i\rangle}{\partial t} = H|\nu_i\rangle. \tag{1.3}$$

The general solution of Eq. (1.3) can be written as a plane wave with a phase factor that depends on time:

$$|\nu_i\,(t)\rangle = e^{-iE_i t}|\nu_i\rangle, \tag{1.4}$$

with E_i the energy of a neutrino with mass m_i, that can be expressed as function of the neutrino momentum k_i as $E_i = \sqrt{k_i^2 + m_i^2}$. Then, using Eq. (1.2) the time evolution of each flavour state is given by

$$|\nu_\alpha\,(t)\rangle = \sum_\beta \sum_i U_{\beta i} U^*_{\alpha i} e^{-iE_i t}|\nu_\beta\rangle. \tag{1.5}$$

Eq. (1.5) tells us that, if the PMNS matrix is not diagonal (*i.e.* the mass eigenstates are different from the flavour states), then a neutrino produced initially (via a weak interaction) with a flavour α can be detected (via a weak interaction) some time later in a different flavour

β. This phenomenon, called neutrino oscillation, was discovered by the Super-Kamiokande (Super-K) experiment in 1998 [5]. The probability for an ultrarelativistic neutrino α with energy E to oscillate to a neutrino β after propagating for a distance L in vacuum is

$$P_{\nu_\alpha \to \nu_\beta} = |\langle \nu_\beta | \nu_\alpha \rangle|^2 = \sum_{ij} U^*_{\alpha i} U_{\beta i} U^*_{\beta j} U_{\alpha j} e^{-i \frac{\Delta m^2_{ij}}{2E} L}, \tag{1.6}$$

where $\Delta m^2_{ij} = m^2_i - m^2_j$ is the squared mass difference between the i and j neutrino masses. This means that neutrino oscillation experiments are only sensitive to the difference between squared masses, and not to the individual neutrino masses. The expression in Eq. (1.6) can also be rewritten in a general form using the unitarity property of the PMNS matrix:

$$\begin{aligned} P_{\nu_\alpha \to \nu_\beta} = \; & \delta_{\alpha\beta} - 4 \sum_{i>j} \mathfrak{Re} \left(U^*_{\alpha i} U_{\beta i} U_{\alpha j} U^*_{\beta j} \right) \sin^2 \left(\frac{\Delta m^2_{ij} L}{4E} \right) \\ & + 2 \sum_{i>j} \mathfrak{Im} \left(U^*_{\alpha i} U_{\beta i} U_{\alpha j} U^*_{\beta j} \right) \sin \left(\frac{\Delta m^2_{ij} L}{2E} \right). \end{aligned} \tag{1.7}$$

Since the matrix U is unitary, the oscillation probability $P_{\nu_\alpha \to \nu_\beta}$ yields unity when the sum over all the β flavors is performed. An equivalent oscillation probability for antineutrinos $P_{\bar{\nu}_\alpha \to \bar{\nu}_\beta}$ can be obtained by applying the charge and parity conjugation operators in Eq. (1.7) which yields a change of sign in the last term of the equation. Therefore, if the matrix U is complex, neutrinos and antineutrinos oscillate with different probabilities and the neutrino oscillation phenomenon is said to violate Charge-Parity (CP) symmetry. The PMNS matrix is commonly parametrized in the following way:

$$U = \begin{pmatrix} 1 & 0 & 0 \\ 0 & c_{23} & s_{23} \\ 0 & -s_{23} & c_{23} \end{pmatrix} \begin{pmatrix} c_{13} & 0 & s_{13} e^{-i\delta_{CP}} \\ 0 & 1 & 0 \\ -s_{13} e^{i\delta_{CP}} & 0 & c_{13} \end{pmatrix} \begin{pmatrix} c_{12} & s_{12} & 0 \\ -s_{12} & c_{12} & 0 \\ 0 & 0 & 1 \end{pmatrix} \begin{pmatrix} e^{i\alpha_1/2} & 0 & 0 \\ 0 & e^{i\alpha_2/2} & 0 \\ 0 & 0 & 1 \end{pmatrix}, \tag{1.8}$$

where $s_{ij} = \sin\theta_{ij}$ and $c_{ij} = \cos\theta_{ij}$ with θ_{ij} the three mixing angles and δ_{CP}, α_1 and

α_2 are complex phases. The parameters α_1 and α_2 are only non-zero if neutrinos are Majorana particles, *i.e.*, neutrinos coincide with their own antiparticles. At the current time it is still not clear if neutrinos are Majorana particles, but the effects of the parameters α_1 and α_2 cannot be observed in neutrino oscillation experiments. Instead, it is possible to determine if neutrinos are their own antiparticles in processes that violate total lepton number conservation such as neutrinoless double beta decay [6], but there is not yet experimental evidence of such process. The first and the third matrices in Eq. (1.8) contain the atmospheric mixing angle θ_{23}, which is sensitive to the oscillation of neutrinos created in the atmosphere, and the solar mixing angle θ_{12} which mostly controls solar neutrino oscillations. The second matrix contains the CP-violating phase δ_{CP} and the reactor mixing angle θ_{13}. After the confirmation of the existence of neutrino oscillations, experiments have mainly focused in the measurement of the oscillation parameters: the three mixing angles θ_{23}, θ_{13}, θ_{12}, two squared mass differences Δm^2_{12} and Δm^2_{32}, and the CP-violating phase δ_{CP}. Furthermore, the neutrino mass hierarchy, *i.e.*, the sign of the mass splitting between m_2 and m_3 mass eigenstates, is still unknown. A summary of the current value of the neutrino oscillation parameters obtained from a global fit [7, 8] is shown in Fig 1·1.

1.2 Accelerator neutrino experiments

The dependence of the oscillation probability on the ratio of the distance between the points where neutrinos are created and detected and the neutrino energy, L/E, can be clearly seen in Eq. (1.7). This distance, commonly referred as baseline, varies for the different types of neutrino oscillation experiments. For instance, in solar neutrino experiments the baseline is naturally fixed by the distance between the Sun and the Earth's surface. For atmospheric neutrino experiments the detector is localized in a specific place on the Earth, but the neutrinos produced in the entire atmosphere can be detected. In other kinds of experiments, the ratio L/E can be carefully selected to have an optimal sensitivity to some oscillation

NuFIT 5.2 (2022)

		Normal Ordering (best fit)		Inverted Ordering ($\Delta\chi^2 = 2.3$)	
		bfp $\pm 1\sigma$	3σ range	bfp $\pm 1\sigma$	3σ range
without SK atmospheric data	$\sin^2\theta_{12}$	$0.303^{+0.012}_{-0.011}$	$0.270 \to 0.341$	$0.303^{+0.012}_{-0.011}$	$0.270 \to 0.341$
	$\theta_{12}/^\circ$	$33.41^{+0.75}_{-0.72}$	$31.31 \to 35.74$	$33.41^{+0.75}_{-0.72}$	$31.31 \to 35.74$
	$\sin^2\theta_{23}$	$0.572^{+0.018}_{-0.023}$	$0.406 \to 0.620$	$0.578^{+0.016}_{-0.021}$	$0.412 \to 0.623$
	$\theta_{23}/^\circ$	$49.1^{+1.0}_{-1.3}$	$39.6 \to 51.9$	$49.5^{+0.9}_{-1.2}$	$39.9 \to 52.1$
	$\sin^2\theta_{13}$	$0.02203^{+0.00056}_{-0.00059}$	$0.02029 \to 0.02391$	$0.02219^{+0.00060}_{-0.00057}$	$0.02047 \to 0.02396$
	$\theta_{13}/^\circ$	$8.54^{+0.11}_{-0.12}$	$8.19 \to 8.89$	$8.57^{+0.12}_{-0.11}$	$8.23 \to 8.90$
	$\delta_{\rm CP}/^\circ$	197^{+42}_{-25}	$108 \to 404$	286^{+27}_{-32}	$192 \to 360$
	$\frac{\Delta m^2_{21}}{10^{-5}\ \text{eV}^2}$	$7.41^{+0.21}_{-0.20}$	$6.82 \to 8.03$	$7.41^{+0.21}_{-0.20}$	$6.82 \to 8.03$
	$\frac{\Delta m^2_{3\ell}}{10^{-3}\ \text{eV}^2}$	$+2.511^{+0.028}_{-0.027}$	$+2.428 \to +2.597$	$-2.498^{+0.032}_{-0.025}$	$-2.581 \to -2.408$
		Normal Ordering (best fit)		Inverted Ordering ($\Delta\chi^2 = 6.4$)	
		bfp $\pm 1\sigma$	3σ range	bfp $\pm 1\sigma$	3σ range
with SK atmospheric data	$\sin^2\theta_{12}$	$0.303^{+0.012}_{-0.012}$	$0.270 \to 0.341$	$0.303^{+0.012}_{-0.011}$	$0.270 \to 0.341$
	$\theta_{12}/^\circ$	$33.41^{+0.75}_{-0.72}$	$31.31 \to 35.74$	$33.41^{+0.75}_{-0.72}$	$31.31 \to 35.74$
	$\sin^2\theta_{23}$	$0.451^{+0.019}_{-0.016}$	$0.408 \to 0.603$	$0.569^{+0.016}_{-0.021}$	$0.412 \to 0.613$
	$\theta_{23}/^\circ$	$42.2^{+1.1}_{-0.9}$	$39.7 \to 51.0$	$49.0^{+1.0}_{-1.2}$	$39.9 \to 51.5$
	$\sin^2\theta_{13}$	$0.02225^{+0.00056}_{-0.00059}$	$0.02052 \to 0.02398$	$0.02223^{+0.00058}_{-0.00058}$	$0.02048 \to 0.02416$
	$\theta_{13}/^\circ$	$8.58^{+0.11}_{-0.11}$	$8.23 \to 8.91$	$8.57^{+0.11}_{-0.11}$	$8.23 \to 8.94$
	$\delta_{\rm CP}/^\circ$	232^{+36}_{-26}	$144 \to 350$	276^{+22}_{-29}	$194 \to 344$
	$\frac{\Delta m^2_{21}}{10^{-5}\ \text{eV}^2}$	$7.41^{+0.21}_{-0.20}$	$6.82 \to 8.03$	$7.41^{+0.21}_{-0.20}$	$6.82 \to 8.03$
	$\frac{\Delta m^2_{3\ell}}{10^{-3}\ \text{eV}^2}$	$+2.507^{+0.026}_{-0.027}$	$+2.427 \to +2.590$	$-2.486^{+0.025}_{-0.028}$	$-2.570 \to -2.406$

Figure 1·1: 3ν oscillation parameters obtained from different global analysis of neutrino data available in November 2022 [7, 8]. $\Delta m^2_{3l} \equiv \Delta m^2_{32} > 0$ for NO (normal ordering with $m_3 > m_2$) and $\Delta m^2_{3l} \equiv \Delta m^2_{31} < 0$ for IO (inverted ordering with $m_1 > m_3$). "bfp" stands for best fit points.

parameters. Reactor and accelerator neutrino experiments are examples of the latter case, which can be further categorized into long- ($L/E \gtrsim 100$ km GeV^{-1} which make them sensible to $\Delta m^2 \lesssim 10^{-2}$ eV^2) and short- ($L/E \lesssim 10$ km GeV^{-1} which explore $\Delta m^2 \gtrsim 10^{-1}$ eV^2) baseline experiments. For the purpose of this thesis we will focus specifically on accelerator neutrino oscillation experiments, which cover the intermediate range of neutrino energies

between several hundreds of MeV up to a few GeV.

Modern accelerator-based neutrino experiments can produce muon and electron neutrinos, as well as antineutrinos, from accelerated protons. Protons are accelerated using a particle accelerator and do interact with a heavy target producing a beam of secondary mesons. The target is usually located inside shaped magnetic fields, denominated horns, that are used to select mesons of a preferred charge (for example positive pions). If the positive (negative) mesons are selected then it is said that the accelerator is working on neutrino (antineutrino) mode. The beam of mesons is directed into a long decay volume, where mesons decay into a beam dominated by muon-neutrinos (neutrino mode) or muon-antineutrinos (antineutrino mode) and a large mass of material absorbs all the particles except the neutrinos at the end. Even with the focusing magnetic horns, the neutrino (antineutrino) beam is contaminated with antineutrinos (neutrinos). Also, there is a small contamination of electron neutrinos which come from the decay of kaons and muons present in the secondary beam. In addition to maximizing the flux of neutrinos with energies close to the maximum of the oscillation probability, neutrinos with energies far from this maximum should be avoided because they might result in unwanted background processes. The energy of neutrino from a pion decay is given by

$$E_\nu = \frac{m_\pi^2 - m_\mu^2}{2\left(E_\pi - p_\pi \cos\theta\right)}, \tag{1.9}$$

where E_π is the energy of the pion, θ is the angle between the pion and the neutrino direction, p_π is the pion momentum and m_π and m_μ are the pion and muon masses. Using this relation, a neutrino beam with narrow energy spectrum around the energy determined by θ, which is more convenient for oscillation analyses, can be obtained. Therefore, accelerator neutrino experiments can also be further classified as on-axis beam experiments, that have a wider beam energy spectrum, and off-axis beam experiments, which present a narrower spectrum.

Some accelerator experiments use two detectors to reduce the systematic uncertainties

coming from the neutrino flux and neutrino-nuclei interactions. The near detector, *i.e.* the one closer to the source of neutrinos, either uses the same technology as the far detector, *i.e.* the one localized far away from the neutrino source that measures the oscillated neutrino flux, or consists of sub-detectors with complementary functions to obtain detailed information of the neutrino beam and neutrino interactions with complex nuclei. The near detectors are used to characterize the neutrino flux, its energy distribution and the interaction cross sections, which are used as an input to make predictions of observables at the far detector. Deviations between the two energy spectra detected by both detectors may be used to infer the presence of neutrino oscillations, which manifest themselves as the disappearance of the ν_μ beam, or the appearance of a different neutrino flavor in the ν_μ beam. However, one should note that the neutrino flux is inevitably different between the near and the far detectors, even without considering neutrino oscillations, due to differences between detector technologies and targets used. The neutrino oscillations change the flavour composition of the neutrino beam quite significantly, as the design of a neutrino oscillation experiment requires. For the precision measurements of neutrino oscillations with accelerator experiments, the understanding of the neutrino-nucleus interaction becomes crucial. Because complex nuclei are used as targets, the nuclear effects complicate the understanding of the neutrino-nucleus interaction as it will be explained in the Section 1.3.

Current long-baseline neutrino oscillation experiments measure both the appearance (for instance $\nu_\mu \to \nu_e$) and the disappearance $\nu_\mu \to \nu_\mu$ channels, each of them sensitive to some oscillation parameters. We can consider these two specific cases that are relevant for long-baseline experiments. The first one corresponds to the $\nu_\mu \to \nu_e$ appearance channel with a

probability including matter effects [9] given by [10]

$$
\begin{aligned}
P\left(\nu_\mu \to \nu_e\right) = & \, 4c_{13}^2 s_{13}^2 s_{23}^2 \sin^2 \Delta_{31} \\
& + 8c_{13}^2 s_{12} s_{13} s_{23} \left(c_{12} c_{23} \cos\delta_{CP} - s_{12} s_{13} s_{23}\right) \cos\Delta_{32} \sin\Delta_{31} \sin\Delta_{21} \\
& - 8c_{13}^2 c_{12} c_{23} s_{12} s_{13} s_{23} \sin\delta_{CP} \sin\Delta_{32} \sin\Delta_{31} \sin\Delta_{21} \\
& + 4s_{12}^2 c_{13}^2 \left(c_{12}^2 c_{23}^2 + s_{12}^2 s_{23}^2 s_{13}^2 - 2c_{12} c_{23} s_{12} s_{23} s_{13} \cos\delta_{CP}\right) \sin^2 \Delta_{21} \\
& - 8c_{13}^2 s_{13}^2 s_{23}^2 \frac{aL}{4E_\nu} \left(1 - 2s_{13}^2\right) \cos\Delta_{32} \sin\Delta_{31} \\
& + 8c_{13}^2 s_{13}^2 s_{23}^2 \frac{a}{\Delta m_{31}^2} \left(1 - 2s_{13}^2\right) \sin^2 \Delta_{31}, \qquad (1.10)
\end{aligned}
$$

with $\Delta_{ij} = \Delta m_{ij}^2 L/4E_\nu$ and $a = 2\sqrt{2} G_F n_e E_\nu$, where n_e is the average electron density of the medium and G_F is the Fermi constant. The second case is the ν_μ survival probability

$$
P\left(\nu_\mu \to \nu_\mu\right) \approx 1 - \sin^2 2\theta_{23} \sin^2 \Delta_{32}. \qquad (1.11)
$$

To obtain the corresponding antineutrino oscillation probabilities one needs to replace $\delta_{CP} \to -\delta_{CP}$ and $a \to -a$, which only affects $\nu_\mu \to \nu_e$ probability given in Eq. (1.10). In particular, the third term in Eq. (1.10), which contains $\sin\delta_{CP}$, is the CP violating term that flips sign between ν and $\bar{\nu}$ and thus introduces CP asymmetry if $\sin\delta_{CP}$ is non-zero.

To extract oscillation parameters from neutrino oscillation experiments, experimentalists measure the event rate of reconstructed ν_μ/ν_e events as a function of some observable, for instance the reconstructed neutrino energy. The spectrum for the appearance and disappearance channels is then compared to Monte-Carlo (MC) simulations, in which oscillation parameters are varied until they are in agreement with the data. It is important to note that no single type of neutrino oscillation experiment is sensitive to all oscillation parameters at once, and not with the same precision, but the oscillation probability depends on all parameters at once. Because of this, the results from reactor experiments, which are more

sensitive to θ_{13}, or from solar neutrino experiments, that constrain better θ_{12} and Δm^2_{21}, are often used by accelerator experiments, and in particular by long-baseline experiments, to improve the measurements of $\sin^2\theta_{23}$, Δm^2_{32} and δ_{CP}.

The expected event rates at the near and far detectors can be expressed as function of the neutrino energy E_ν as follows

$$\begin{aligned} N^{near}_{\nu_\alpha}(E_\nu) &= \sigma^{near}_{\nu_\alpha}(E_\nu)\,\phi^{near}_{\nu_\alpha}(E_\nu)\,\epsilon^{near}(E_\nu) \\ N^{far}_{\nu_\beta}(E_\nu) &= \sigma^{far}_{\nu_\beta}(E_\nu)\,\phi^{far}_{\nu_\beta}(E_\nu)\,\epsilon^{far}(E_\nu)\,P_{\nu_\alpha\to\nu_\beta}(E_\nu)\,. \end{aligned} \tag{1.12}$$

They depend on the neutrino flux distributions ϕ_{ν_α}, the neutrino interaction cross-sections with the detector σ_{ν_α} (how probable it is that a neutrino interacts), the detector efficiencies ϵ (how well the detectors will be able to reconstruct the event signaling the neutrino) and, finally, on the oscillation probability $P_{\nu_\alpha\to\nu_\beta}$ (for instance how many of the initial ν_μ survived or how many ν_e appeared in the far detector). Since neutrinos interact weakly, the precision on the event rate is strongly limited by statistical errors. To give some idea about how weak the interaction is, we can imagine a neutrino traveling through a material with density $\rho \sim 10^{23}$ atoms/cm^3. Assuming an associated interaction cross section $\sigma \sim 10^{-38}$ cm^2 for a 1 GeV neutrino, then it would travel $\Delta x \sim \rho\sigma \sim 10^{10}$ km before interacting, a distance comparable to 1.5 million Earth radii or 66 times the distance between the Earth and the Sun. Moreover, effects related to the flux, neutrino interaction cross-sections and the detector efficiency are sources of systematic errors.

In general, for real experiments we find that near and far detectors can have different acceptances and use different technologies and nuclear targets. Additionally, the initial neutrino energy distribution is unknown because of the special method of producing neutrinos as secondary decay products of hadrons that were produced in a primary nuclear reaction between a beam of protons and a nuclear target. Therefore, the neutrino energy must be reconstructed on an event-by-event basis from the particles present in the final state after the

reaction of the neutrino with a nucleus assuming a nuclear model. Under these conditions, what is measured is an averaged oscillation probability as function of the reconstructed neutrino energy that can be expressed as

$$\left\langle P_{\nu_\alpha \to \nu_\beta}\left(E_\nu^{reco}\right)\right\rangle = \frac{\int dE_\nu \sigma_{\nu_\beta}^{far}\left(E_\nu\right)\phi_{\nu_\beta}^{far}\left(E_\nu\right)\epsilon^{far}\left(E_\nu\right)P_{\nu_\alpha \to \nu_\beta}\left(E_\nu\right)S\left(E_\nu^{reco}|E_\nu\right)}{\int dE_\nu \sigma_{\nu_\alpha}^{near}\left(E_\nu\right)\phi_{\nu_\alpha}^{near}\left(E_\nu\right)\epsilon^{near}\left(E_\nu\right)S\left(E_\nu^{reco}|E_\nu\right)}, \tag{1.13}$$

with $S\left(E_\nu^{reco}|E_\nu\right)$ a function that encodes the probability of a specific true neutrino energy E_ν to be reconstructed as E_ν^{reco}.

In what follows, we briefly summarize some of the past, present and future accelerator neutrino experiments dedicated not only to the measurement of oscillation parameters, but also to the determination of experimental neutrino-nucleus cross sections to test theoretical interaction models which are necessary to extract oscillation parameters.

NOMAD

The Neutrino Oscillation Magnetic Detector (NOMAD) [11], that used CERN wide-band neutrinos produced by the 450 GeV proton synchrotron, searched for $\nu_\mu \to \nu_\tau$ oscillation by detecting τ appearance between 1995 and 1998. Its goals were to measure the momenta of charged particles and identify and measure electrons, photons and muons. By the detector design, which used carbon as target, it was also possible to look for $\nu_\mu \to \nu_e$ oscillation [12]. The analysis of the full NOMAD data sample gave no evidence for ν_τ appearance and set with 90% confidence level (C.L.) that the upper limit on the two-flavour $\nu_\mu \to \nu_\tau$ oscillation probability was $P\left(\nu_\mu \to \nu_\tau\right) < 2.2 \times 10^{-4}$[13]. The NOMAD experiment applied for the first time a purely kinematical approach for the detection of ν_τ CC interactions. Unfortunately, oscillations were not discovered with the NOMAD experiment.

K2K

After the success of Super-Kamiokande, that provided the first experimental evidence of atmospheric neutrinos oscillation in 1998, the Japanese National Laboratory for High Energy Accelerator Research Organization (KEK) to Kamiokande (K2K) experiment [14, 15] was created with the main difference of using a well understood muon neutrino beam pointing at the Super-Kamiokande detector at a distance of 250 km. It was the first long-baseline neutrino oscillation experiment to observe the oscillation of ν_μ into ν_τ and found results of squared mass difference and mixing angle that were consistent with Super-Kamiokande results. The experiment, that ran from 1999 to 2004, used a neutrino beam with a wide energy spectrum ranging from 1 to 1.5 GeV and produced by a 12 GeV proton synchrotron beam interacting with an aluminum target. Since knowing the beam composition is required for looking at ν_μ disappearance, a 1-kiloton water Cherenkov near detector, a smaller version of Super-Kamiokande, was used to measure the neutrino beam spectrum. Then this distribution was extrapolated using Monte Carlo simulated data to predict the neutrino spectrum at Super-Kamiokande.

MINOS

The Main Injector Neutrino Oscillation Search (MINOS) was a neutrino oscillation experiment that used a beam from Fermilab and two detectors: one placed a few hundred meters away from the source of the neutrinos and the other 735 km away in Soudan mine in northern Minnesota. The neutrino beam was produced in the NuMI beamline [17] with 120 GeV protons from the Main Injector. Both MINOS detectors were iron-scintillator tracking calorimeters with toroidal magnetic fields [18] designed to be as similar as possible to minimize any systematic errors in comparing the observed neutrino spectra in the two detectors. The NuMI beamline could alter the neutrino energy spectrum by changing the relative position of target and horns. Most of MINOS data were taken with the "low energy"

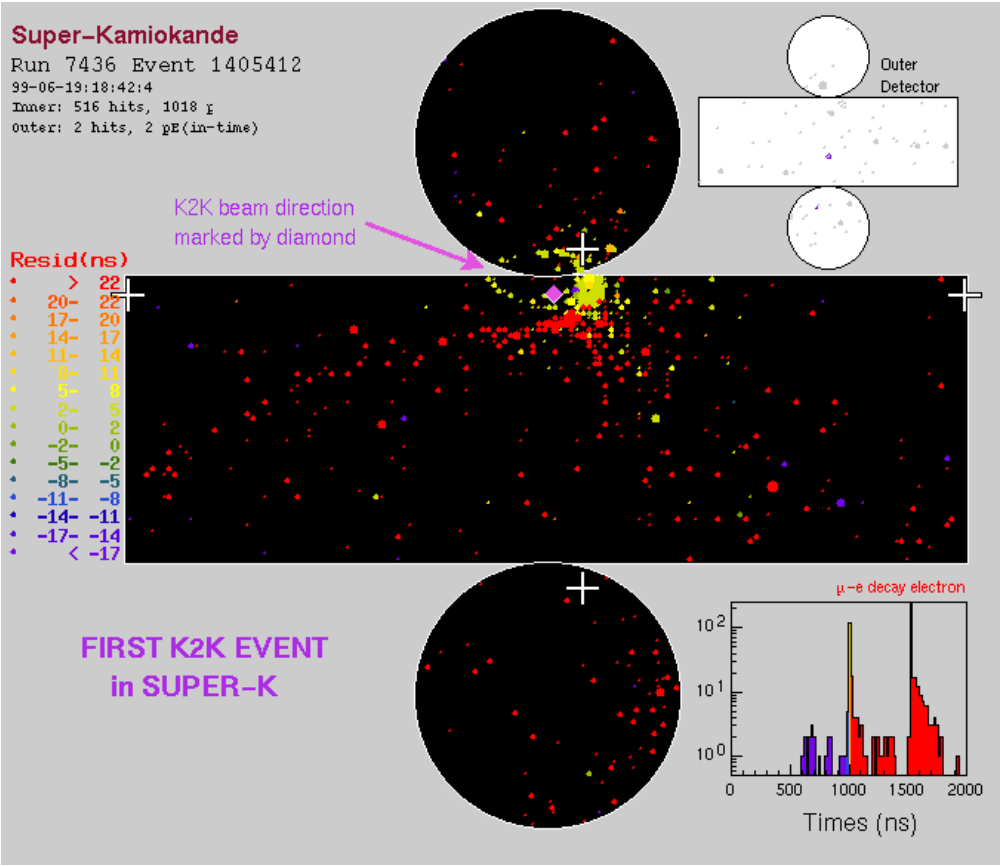

Figure 1·2: First neutrino event detected in June 1999 inside the Super-Kamiokande water Cherenkov detector due to the KEK neutrino beam. The crosses give the reconstructed neutrino interaction vertex and the diamond marks the neutrino beam direction from the vertex. The probability that the event came from an atmospheric neutrino interaction, instead of from a neutrino produced at KEK, was estimated to be 0.01%. Picture taken from [16].

configuration with the peak energy of around 3 GeV. MINOS combined accelerator and atmospheric neutrino data taken from 2005 to 2012 in both disappearance and appearance modes to measure oscillation parameters [19] that were consistent with K2K and Super-Kamiokande measurements of mixing angle and squared mass difference.

NOvA

The NOvA experiment [20, 21] uses the NuMI beamline with an off-axis configuration. The 14 kt NOvA far detector is located near Ash River, Minnesota, 810 km away from the muon neutrinos source, and uses mineral oil as target. The neutrino energy spectrum at the far detector has a peak around 2 GeV, the energy at which oscillation from muon neutrinos to electron neutrinos is expected to be at a maximum for a 810 km baseline. NOvA aims to measure disappearance $\nu_\mu \rightarrow \nu_\mu$ and appearance $\nu_\mu \rightarrow \nu_e$ in both ν_μ and $\bar{\nu}_\mu$ beams to extract θ_{23}, Δm^2_{32} and δ_{CP} parameters. The mass ordering affects the rates of $\nu_\mu \rightarrow \nu_e$ and $\bar{\nu}_\mu \rightarrow \bar{\nu}_e$ oscillations when neutrinos travel through the Earth as compared to the vacuum [9]. These matter effects are important for NOvA due to the large baseline used by the experiment. Depending on the value of δ_{CP} and the mass ordering itself, NOvA may be able to exploit the resulting neutrino-antineutrino asymmetry to measure the sign of Δm^2_{32} and thus determine the mass ordering.

MINERνA

The MINERνA (Main INjector ExpeRiment ν-A) experiment [22] studies neutrino-nucleus scattering to improve models describing the process in order to reduce systematic uncertainties in results from oscillation experiments. It measures neutrino reactions covering an energy range from 1 to 20 GeV. The detector, shown in Fig 1·3, is placed on-axis of the NuMI neutrino beam and it is equipped with different targets (C, CH, Fe, H_2O, Pb) in order to achieve precise measurements of the nuclear effects [23]. The high energetic muons created in neutrino interactions are capable of escaping the MINERνA detector and entering MINOS, located only 2 meters away from MINERνA. MINERνA uses data collected by MINOS to identify and measure these muons.

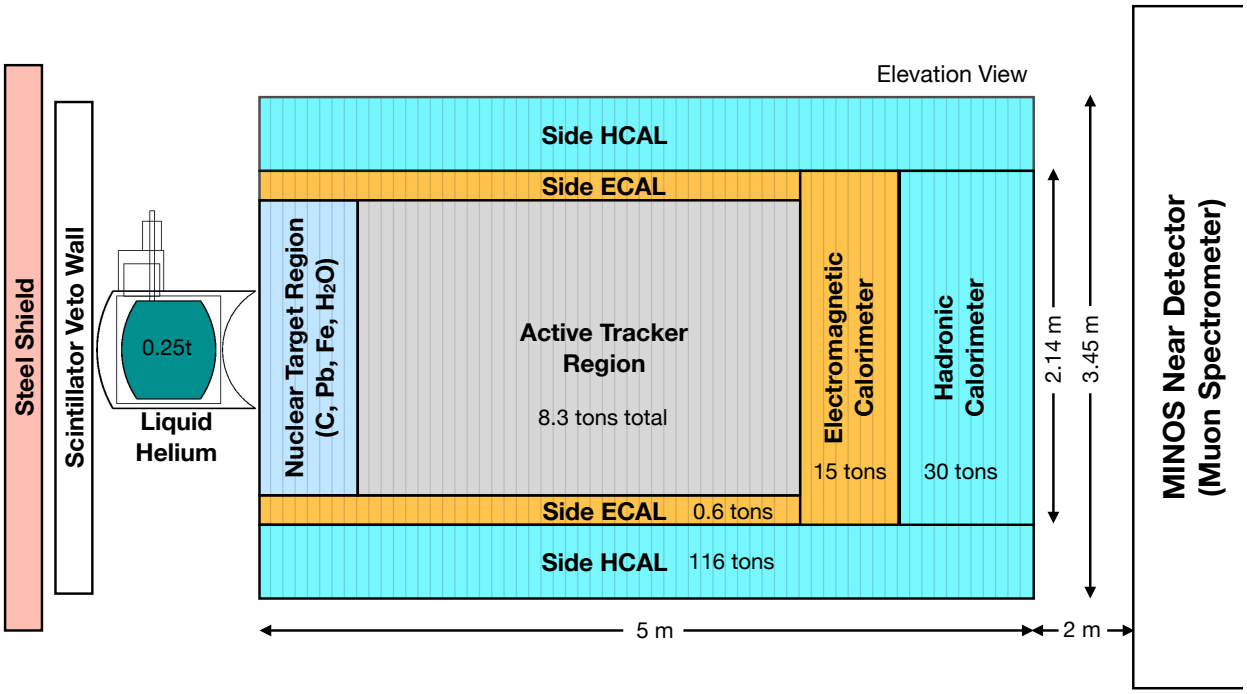

Figure 1·3: Side view of the MINERνA detector showing the different nuclear targets, the fully-active tracking region and the surrounding calorimeters [22].

T2K

After the great success of K2K, the Tōkai-To-Kamioka (T2K) experiment [24, 25] started in 2010 using a newly constructed high-intensity proton synchrotron from the Japanese Proton Accelerator Research Complex (J-PARC) facility at Tōkai. It is the first long-baseline experiment to employ an off-axis neutrino beam. The off-axis angle of 2.5° was chosen to set the peak of neutrino energy spectrum at 0.6 GeV, matching the first maximum of oscillation probability at the 295 km baseline for $\Delta m^2 \approx 2.5 \times 10^{-3}$ eV^2. T2K employs a set of near detectors at about 280 m from the production target. The on-axis detector, called INGRID, is an array of iron-scintillator sandwich trackers to monitor the beam intensity, direction and profile. The off-axis detector, called ND280, consists of several sub-detectors inside a magnet and is placed in the direction of far detector to measure the neutrino beam properties and to study neutrino interactions on hydrocarbon-based or a hybrid water-hydrocarbon targets.

An upgrade of the ND280 is outgoing right now with the aim of reducing the flux and cross-section systematic uncertainties to establish CP violation at 3σ level for a significant fraction of the possible δ_{CP} values [26]. The ND280 measurements are used to predict the number of muon neutrinos that would be seen in Super-Kamiokande if there were no oscillations. Additionally, since it is a magnetized detector, ND280 can measure the wrong sign background in the flux, which is not possible at the far detector. Finally, it is able to precisely reconstruct the exclusive final states of ν_μ and $\bar{\nu}_\mu$ interactions, therefore its data is used as one of the main inputs in the oscillation analysis in order to constrain the neutrino flux and neutrino interaction systematic uncertainties.

In the long term, the Tōkai-To-Hyper-Kamiokande (T2HK) experiment has been proposed as successor [27] of the current T2K program. The Hyper-K experiment is a next-generation, large-scale water Cherenkov neutrino detector that will receive neutrinos from J-PARC accelerator facility like T2K. Due to the large size of the Hyper-K detector (60 m in height and 74 m in diameter) and its improved detection techniques, the long-baseline neutrino oscillations program with the Hyper-K detector will benefit from an improved sensitivity to neutrino oscillation parameters, inaccessible to the current T2K experiment, most notably enabling a 5σ sensitivity to CP violation discovery for a large number of δ_{CP} values.

MiniBooNE & **MicroBooNE**

The Mini Booster Neutrino Experiment (MiniBooNE) collected data from 2002 up to 2012 at Fermilab using a muon neutrino beam to search for ν_e and $\bar{\nu}_e$ appearance in the same parameter region as the Liquid Scintillator Neutrino Detector (LSND) [28, 29] experiment that ran between 1993 and 1998. The Booster Neutrino Beamline (BNB) with a magnetic horn uses a 8 GeV proton beam from the Fermilab booster to produce a neutrino (antineutrino) beam with energy spectrum peak of 0.6 (0.4) GeV. MiniBooNE, as well as LSND, used a single detector setup. It consisted of a 12.2 m diameter sphere filled with 818 t of mineral

oil (CH_2) located around half kilometer from the target. The MiniBooNE collaboration reported ν_e and $\bar{\nu}_e$ event excess in both neutrino and antineutrino running modes. In total, 460.5 ± 99.0 excess events were observed over the expected backgrounds, corresponding to 4.7σ significance [30]. The MicroBooNE Collaboration [31], a further step into the BooNE experiment that began in 2015, is currently operating a large Liquid Argon Time Projection Chamber (LArTPC) that is located on the BNB at Fermilab. MicroBooNE will measure neutrino cross sections with reconstructed neutrino energy between 200 and 475 MeV to investigate the low energy excess events observed by the MiniBooNE experiment. The detector also serves as a next step in a phase program towards the construction of massive kiloton scale LArTPC detectors for future long-baseline neutrino physics (DUNE).

DUNE

DUNE [32] is a new experiment currently under construction, with the goal of discovering CP violation in neutrinos with more than 5σ sensitivity, determining the ordering of the neutrino masses as well as searching for neutrinos beyond the currently known three. DUNE, which is planned to start taking data in 2030's, will be a 1300 km long-baseline experiment based in US with a far detector that will consist of four modules of at least 10 kt fiducial mass LArTPC, located 1.5 km underground at the Sanford Underground Research Facility in South Dakota, and the near detector installed in the Long-Baseline Neutrino Facility (LBNF) at Fermilab.

1.3 Neutrino-nucleus interactions

Neutrino interaction with matter occurs via the weak and gravitational forces, the latter being negligible due to the very small neutrino mass. The corresponding cross sections are very small, of the order of 10^{-38} cm^2/GeV. The type of interaction can be identified exclusively through the particles produced after the reaction. Neutrino weak interactions can

be classified broadly as charged-current (CC) or neutral-current (NC) processes depending on whether a $W^{\pm}$ or a Z boson is exchanged. In the former case there is a charge exchange and a charged lepton is emitted after the interaction, whilst the neutrino preserves its nature in the latter one. The experimental study of NC neutrino interactions is a very demanding task compared with CC reactions due to the difficulties of collecting data of reactions with cross sections even smaller than those of CC processes and in which the outgoing neutrino is not detected, therefore the event identification depends on the detection of one or more hadrons.

A generic scheme showing the nuclear response in a neutrino-nucleus reaction for a fixed value of the momentum transfer q as function of the energy transfer ω is shown in Fig. 1·4. At very small momentum and energy transfer, the only available channel is the elastic one where the neutrino probes the entire nucleus as a single coherent object that recoils intact. At higher energies of a few MeV the neutrino can scatter the nucleus to low-lying excited nucleus states and excite high-frequency collective states of the nucleus called giant resonances. The region of highest interest for our work, that covers the intermediate range of energies between hundreds of MeV up to a few GeV, starts from and is dominated by the quasielastic (QE) scattering where a neutrino scatters off a single bound nucleon which is ejected from the nuclear target. In the QE scattering the boson exchanged in the process is absorbed by a single nucleon, which is knocked out, leading to one-particle-one-hole (1p1h) excitations. However, this is only one possibility and one must also consider the coupling of the exchanged boson to nucleons belonging to correlated pairs, commonly known as nucleon-nucleon (NN) correlations, and to meson-exchange currents (MEC), involving two nucleons interacting via the exchange of a virtual pion or heavier meson. Both these processes may lead to the excitation of two-particle-two-hole (2p2h) as well as one-particle-one-hole states. With increasing ω, the neutrino has enough energy to excite a nucleon into a resonance like Δ or a heavier resonance (generically denoted by N^*) depending on the energy transfer. These

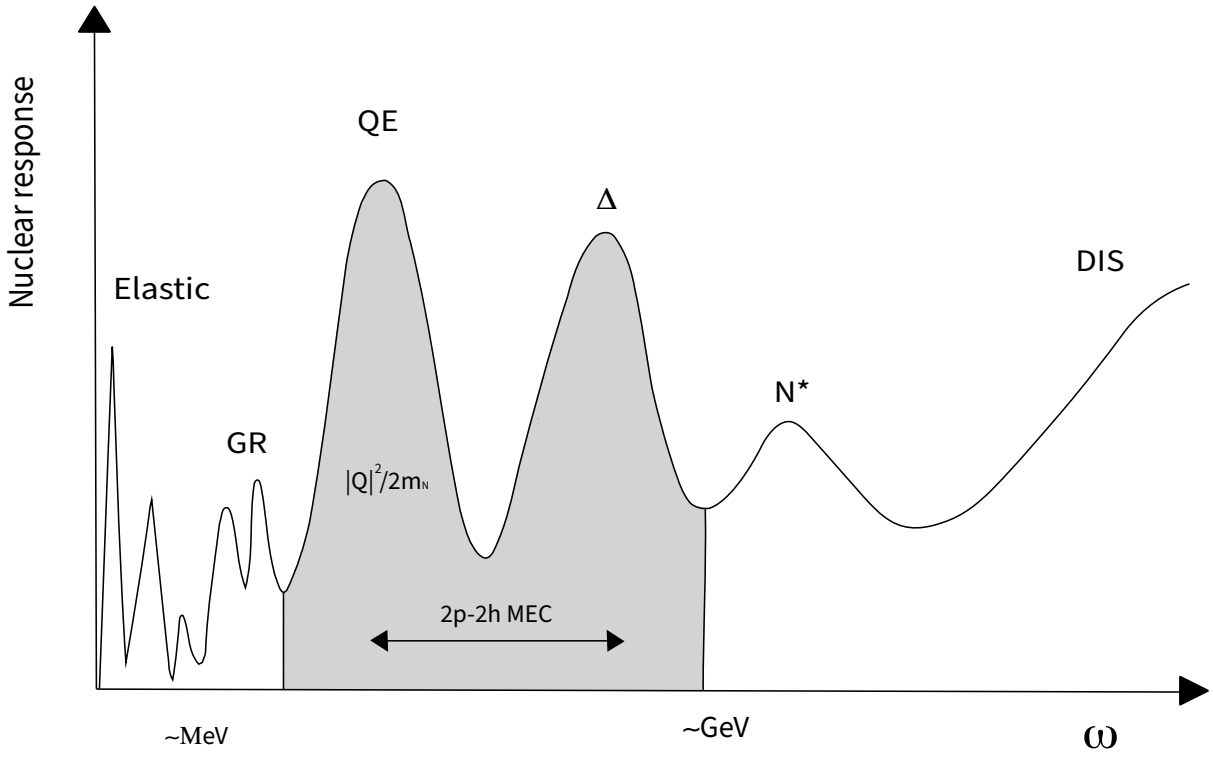

Figure 1·4: Nuclear response as function of the energy transferred to the nucleus for some fixed value of the transferred momentum.

resonances then decay into a variety of final states with different combinations of nucleons and mesons. At even higher values of ω, the relevant interaction channel is the deep inelastic scattering (DIS) where the neutrino has enough energy to probe the inner structure of nucleons and interacts with quarks.

To help reduce the statistical uncertainty of neutrino experiments it is common to use relatively large and complex nuclei as targets, for instance accelerator neutrino experiments often use carbon (T2K, MINERνA, NOνA), oxygen (T2K) or argon (MicroBooNE, DUNE). Using nuclei as targets introduces an additional complexity: the particles that are produced in neutrino interactions, for instance a nucleon ejected from the target or a pion created in

the decay of a nuclear resonance, can interact with the nuclear medium before exiting the residual nucleus. These interactions, known as final-state interactions (FSI), include charge exchange, production of new particles, elastic scattering by a nucleon or absorption by the nuclear medium. FSI can modify the identity and kinematics of the particles created in the primary interaction vertex and limit our ability to identify which reaction channel took place by changing the composition of the hadronic final state. Therefore experimentalists need to rely on theoretical models that describe FSI and other nuclear effects to know which channel was the true interaction mode at the interaction vertex and reconstruct the unknown initial neutrino energy. Since the primary neutrino-nucleon interaction can be determined only in a model-dependent way, neutrino-nucleus data samples are usually presented by topologies, *i.e.*, a specific combination of particles detected in the final state, rather than theoretical interaction modes. This definition used by experimentalists, while in some sense unavoidable, requires a very accurate theoretical input. For instance, a commonly used topology like CC0π defined by one muon, no pions and any number of protons in the final state is populated by multiple reaction channels like QE scattering, 2p2h and pion production followed by absorption in the nuclear medium. All these reaction channels can produce a final state compatible with the CC0π signal definition, consequently they all need to be considered and modeled from a theoretical point of view. Because of the special way to produce neutrinos in accelerator-based experiments, measurements of differential neutrino-nucleus cross sections are commonly presented as function of direct observables like muon or proton kinematics, making necessary to integrate the theoretical cross sections over the specific neutrino flux of the experiment and include all the relevant processes to compare with experimental results.

Previously, we have mentioned that the oscillation probability depends on the neutrino energy. However, the initial neutrino energy is unknown, therefore it has to be reconstructed from final-state particles that are detected. Two different reconstruction methods are typically used in modern accelerator neutrino experiments:

- Kinematic method: this method is extensively used by low-energy experiments like T2K or MiniBooNE. In the case of T2K, Super-Kamiokande is a water Cherenkov detector, hence protons with energy below $\sim$ 1.5 GeV and neutrons are invisible. Because of this, the neutrino energy needs to be reconstructed using only lepton kinematics. Since the dominant interaction channel for low-energy neutrino experiments like T2K (the neutrino energy distribution peaks at 0.6 GeV) is charged-current quasielastic (CCQE) scattering, the neutrino energy is usually reconstructed from the final lepton kinematics using the following expression

$$E_{\nu}^{reco} = \frac{m_p^2 - m_l^2 + 2E_l\left(m_n - E_b\right) - \left(m_n - E_b\right)^2}{2\left(m_n - E_b - E_l + k'\cos\theta_l\right)}, \tag{1.14}$$

where m_n, m_l and m_p are the masses of the neutron, detected lepton (electron or muon) and proton involved in the interaction, E_l, k' and θ_l are the detected lepton energy, momentum and scattering angle, and E_b is the binding or removal energy, defined as the energy necessary to remove one bound nucleon from a nucleus. Notice that Eq. (1.14) has been obtained under the assumptions that the initial single nucleon that interacts with the neutrino is at rest and bound with some fixed biding energy E_b and that the interaction is a true CCQE event. This is a crude approximation, since in fact nucleons inside the nucleus are hardly at rest but in constant movement (known as Fermi motion) and, as discussed above, not only the CCQE channel contributes to the CC0π topology but non-CCQE processes, such as pion production and reabsorption and 2p2h, are also relevant. Those effects can lead to misidentification of the number of CCQE events registered in the detectors and introduce a bias in the reconstructed neutrino energy if Eq. (1.14) is used [33, 34], therefore it is essential for the analysis of neutrino oscillation data to model correctly all those effects. A historical example of why non-CCQE channels need to be taken into account came from the first MiniBooNE CCQE-like (CC0π with pion absorption subtracted) measurements of neutrinos interactions

on ^{12}C [35, 36] where a disagreement between the experimental measurements and theoretical CCQE predictions, that underestimated the data, was found. The discrepancy was prematurely explained by increasing the value of the nucleon axial mass, which is a parameter that appears in the axial nucleon form factor of the nuclear current, to $\sim$ 1.35 GeV, in conflict with the previous established value of 1.03 GeV from bubble chamber experiments [37, 38, 39] and NOMAD measurements [40]. This conflict was solved first by *Martini et al.* [41, 42, 43] who pointed out that 2p2h excitations with RPA corrections could explain the experimental discrepancies without increasing the value of the axial mass. MiniBooNE overestimation of the theoretical models was also explained by *Amaro et al.* [44, 45] and *Nieves et al.* [46] following a similar approach of including 2p2h excitations.

- Calorimetric method: some neutrino detectors like liquid scintillator, magnetized iron detectors, or LArTPC may be able to collect the majority of the calorimetric deposition in a neutrino event and be sensitive to the hadronic part of the interaction [47]. Assuming the typical CC0π signal definition with one lepton and exactly one proton detected in the final state, the calorimetric energy E_{cal} can be used as a measurement of the initial neutrino energy using the conservation of the total energy

$$E_{\nu}^{reco} \approx E^{cal} = E_l + T_N + \epsilon, \tag{1.15}$$

with T_N the kinetic energy of the ejected proton and ϵ the average nucleon separation energy. This reconstruction method is not free from systematic uncertainties since multi-nucleon interactions, FSI and pion absorption take away some of the initial energy of the neutrino. Furthermore, neutrons typically escape detection. A recent study [48] has shown that using the calorimetric reconstruction method, which depends on the detection of both a lepton and an ejected proton, improves the reconstructed

energy resolution and the sensitivity to possible bias in the removal energy estimation compared with the kinematic method, that requires only the detection of the lepton. Note however that his analysis has been performed neglecting in the calorimetric method the nuclear removal energy and the loss of energy due to nuclear FSI.

Chapter 2

General semi-inclusive neutrino-nucleus scattering formalism

As discussed in Secs. 1.2 and 1.3, accelerator neutrino experiments use large amount of target material to increase the probability of interaction of the incoming neutrinos. The targets commonly used by the experimental collaborations are hydrocarbons and water hence neutrinos (or antineutrinos) typically interact with hydrogen, carbon or oxygen nuclei. However, other heavier nuclei such as iron or argon are also used. In particular, argon is used in many present programs, like MicroBooNE, and future experiments, including DUNE, which employ LArTPC detectors. In order to extract the oscillation parameters it is necessary to reconstruct the incident neutrino energy from the reaction products because the neutrino production mechanism typically results in neutrino beams with a very broad flux distribution (for instance see Fig. 2·4). Moreover, this reconstruction method requires basic understanding of nuclear reactions and the nuclear structure of the target nucleus. With the aim of increasing the number of events that are detected, experimental collaborations usually measure inclusive CC or CC0π cross sections where only a final-state charged lepton (*i.e.* an electron or a muon) is detected in presence or not of pions in the final state, respectively. Since these inclusive cross sections are completely integrated over the hadronic degrees of freedom, they are relatively insensitive to the model chosen for the description of the nuclear state. This means that simple models of the nucleus can provide CC inclusive cross section results that are not very different from those found in more elaborated models [49, 50, 51,

52]. However, comparison with these neutrino scattering data is not sufficient to test the validity of the different models. The wide nature of the neutrino beam makes the separation of true QE events from contributions of other elemental processes a very complicated task and the cross section uncertainties are usually too large to discriminate between different nuclear models. Therefore, it is important to compare the different model predictions to the much more accurate electron scattering data for which the incoming electron energy is known. The connection between electron and neutrino scattering has been analyzed in the past (see [53] and references therein) and it is commonly accepted within the neutrino community that any nuclear model that aims to describe the neutrino-nucleus interaction for oscillation experiments must be first validated against electron scattering data. In addition, in the last years a number of cross section measurements have been performed by different neutrino collaborations where not only the final charged lepton is detected but also some hadron as well. This is driven by the goal of constraining the incident neutrino energy much better compared with the case where only the final charged lepton is detected. One of these reactions corresponds to the interaction of an incoming neutrino with a bound neutron of the target nucleus and the detection in coincidence of a charged lepton and a proton in the final state. This reaction, which will be the focus of this thesis, is not an inclusive one but a *semi-inclusive* reaction [49, 50, 51, 54]. Although the theoretical description of semi-inclusive reactions is more complicated than modeling inclusive processes, the richer structure of the cross sections allows one to better discriminate between different nuclear models and improve the reconstruction of the neutrino energy.

In this chapter, the focus will be in the theoretical description of the semi-inclusive CC neutrino-nucleus reaction where a charged lepton and an ejected nucleon are detected in the final state. We will start by describing in general the kinematics of the reaction and later the analytic expressions of the semi-inclusive CC cross section in the plane-wave impulse approximation for different models of the initial nuclear state will be given.

2.1 Semi-inclusive neutrino-nucleus kinematics

The general semi-inclusive CC neutrino[1]-nucleus reaction [54], schematically shown in Fig. 2·1, involves an incident neutrino $K^\mu = (\epsilon, \mathbf{k})$ that interacts with a target nucleus $P_A^\mu = (M_A, 0)$, considered at rest in the laboratory system with rest mass M_A, by exchanging energy ω and momentum $\mathbf{q}$ via an intermediate boson $Q^\mu = (\omega, \mathbf{q})$. We assume that the final state is composed by a charged lepton $K'^\mu = (E_l, \mathbf{k}')$, an ejected nucleon $P_N^\mu = (E_N, \mathbf{p_N})$ and the residual nucleus $P_{A-1}^\mu = (E_{A-1}, \mathbf{p_{A-1}})$. Generally, the residual nucleus could be in its ground state or in some discrete excited state with invariant mass W_{A-1}. Given that the energies involved in the typical accelerator neutrino experiments are of the order of GeV, in this chapter the treatment of the kinematics, and later of the nuclear models, will be completely relativistic. The energy and momentum conservation in the hadronic vertex yields

$$\begin{aligned} M_A + \omega &= E_N + E_{A-1} \\ \mathbf{p_{A-1}} &= \mathbf{q} - \mathbf{p_N} = -\mathbf{p_m}, \end{aligned} \tag{2.1}$$

[1]This thesis is focused in neutrino-nucleus semi inclusive cross sections. Of course the formalism is also valid for reactions with antineutrinos. However there is not semi-inclusive antineutrino-nucleus experimental data available at the time of writing because the additional difficulty of detecting neutrons in the final state.

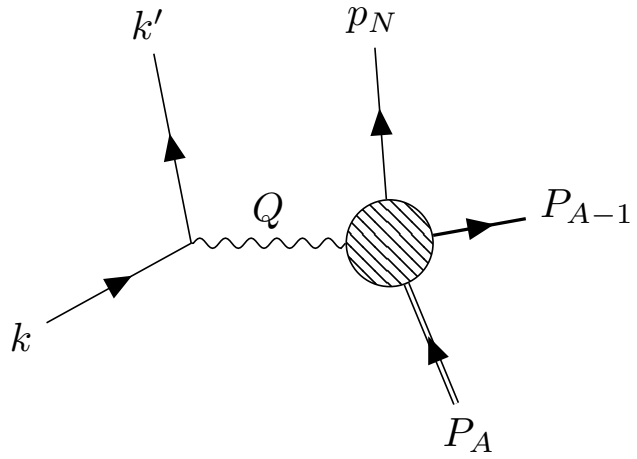

Figure 2·1: Schematic representation of the reaction A$(\nu, l\, N)$A-1 in the Born approximation, *i.e.* one boson exchange.

where we have defined the missing momentum $\mathbf{p_m}$ as minus the momentum of the residual nucleus, hence the total energy of the residual nucleus can be expressed as $E_{A-1} = \sqrt{p_m^2 + W_{A-1}^2}$. It is convenient to introduce a variable that measures the degree of internal excitation of the residual nucleus. The excitation energy of the residual nucleus $\mathcal{E}$ is defined as

$$\mathcal{E} = E_{A-1} - E_{A-1}^0 = \sqrt{p_m^2 + W_{A-1}^2} - \sqrt{p_m^2 + M_{A-1}^2} \geq 0 \tag{2.2}$$

with M_{A-1} the rest mass of the residual nucleus. We can also define the so-called missing energy E_m as

$$E_m = W_{A-1} + m_N - M_A \tag{2.3}$$

and easily relate it with the excitation energy $\mathcal{E}$ in the limit $p_m << M_{A-1}$

$$E_m = \mathcal{E} + E_s, \tag{2.4}$$

where $E_s = M_{A-1} + m_N - M_A$ is the separation energy, namely the minimum energy necessary to remove a nucleon from a nucleus A. Using the conservation of energy and momentum in Eq. (2.1) and the definition of $\mathcal{E}$ we have

$$\mathcal{E} = M_{A-1} - E_s + m_N + \omega - \sqrt{m_N^2 + p_m^2 + q^2 + 2p_m q\cos\theta} - \sqrt{p_m^2 + M_{A-1}^2}, \tag{2.5}$$

with θ the angle between the missing and transfer momenta. This relation, for some fixed values of q and ω, gives a curve $\mathcal{E}\,(p_m)$ for each value of θ. Since the value of θ is limited to the range $-1 \leq \cos\theta \leq 1$, not all the plane $(\mathcal{E}, p_m)$ is accessible and the maximum and minimum values of p_m that are allowed will depend on the specific state of the residual nucleus, q and ω [55, 56]. The advantage of using $(\mathcal{E}, p_m)$ or (E_m, p_m) as dynamic variables of the process, in addition to q and ω, instead of experimental-accessible variables like the ejected proton

momentum and polar angle respect to the neutrino beam is that these variables are more appropriate to describe the nuclear dynamics. The most relevant contributions of the semi-inclusive cross section are localized at relatively small values of $\mathcal{E}$, where one typically finds distributions as functions of p_m that reflect the shell structure of the target nucleus. For instance, in a simple shell model of the nucleus one sees features that reflect the knockout of nucleons from the valence shell, the next-to-valence shell and so on. These momentum distributions fall relatively fast with increasing p_m. Nevertheless for the analysis of exclusive $(e, e'p)$ measurements these simple models have been proven not to be adequate and one requires overall suppression of these momentum distributions by factors of typically 30% via the so-called spectroscopic factors [57]. Additionally, from past $(e, e'p)$ studies one knows that part of this missing strength is moved to higher values of $\mathcal{E}$, partially through nuclear interactions that make both initial and final nuclear states more complex than the simple shell model. For instance, the NN interaction has both long- and short-range contributions, and especially the latter can promote strength to higher values of $\mathcal{E}$ and p_m [57, 58]. Around $20\% - 30\%$ of the strength is known to occupy this high $\mathcal{E}$ and p_m region, although the actual contributions are not very well determined.

2.2 Plane-wave impulse approximation

In the previous section we have described in a generic way the semi-inclusive CC neutrino-nucleus reaction and its kinematics. However due to the complexity of the interaction of the exchanged boson with a many-body system, *i.e.* the initial nucleus, we will make use of the impulse approximation (IA), only valid for high values of q, to describe the hadronic vertex. In the IA, the boson exchanged in the process is absorbed by a single bound nucleon of the initial nucleus, therefore the hadronic current is constructed only by one-body operators and two-body currents are not considered. If one neglects FSI, the nucleon ejected from the nucleus and detected in the final state is the one that interacted directly with the

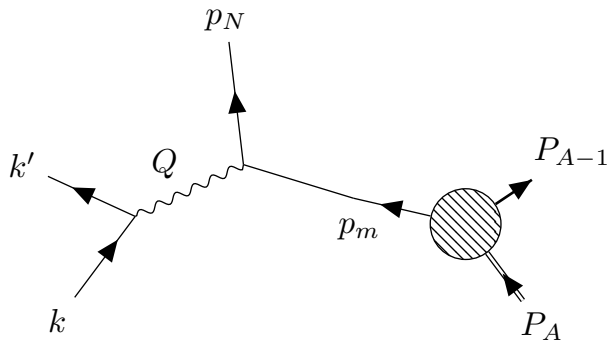

Figure 2·2: Semi-inclusive neutrino-nucleus interaction in the IA.

exchanged boson, while the rest of the nucleons inside the nucleus participate in the reaction as spectators. The semi-inclusive reaction in this approximation is schematically represented in Fig. 2·2 and two new variables are introduced, the momentum p and energy E of the bound nucleon, which can be related with the rest through conservation

$$\begin{aligned} E &= E_N - \omega = M_A - E_{A-1} \\ \mathbf{p} &= \mathbf{p_N} - \mathbf{q} = \mathbf{p_m}. \end{aligned} \tag{2.6}$$

Notice that the momentum of the bound nucleon is equal to the missing momentum and, since a nucleon bound inside a nucleus is off-shell, in general its energy and momentum are not related through the usual on-shell relativistic expression of the energy: $E \neq \overline{E} = \sqrt{p_m^2 + m_N^2}$. Regarding the description of the ejected nucleon, to start we assume a further simplification by considering the ejected nucleon as a plane-wave, *i.e.*, the distortion caused by the residual nucleus is neglected. This corresponds to the plane-wave impulse approximation (PWIA) and allows us to greatly simplify the description of the hadronic vertex by factorizing the nuclear hadronic tensor $H^{\mu\nu}$ in the product of two objects. On of them is the single-nucleon hadronic tensor $\mathcal{W}^{\mu\nu}$ that is constructed by considering that the neutrino interacts with a single off-shell nucleon described by Dirac spinors with positive energy. And the other is the so-called spectral function $S(p_m, E_m)$ that depends on the specific nuclear model used

to describe the initial nuclear state and is defined as the probability of finding a nucleon in the initial nucleus with energy E_m and momentum p_m compatible with the kinematics of the process. This exact factorization can also be found in the analysis of exclusive $(e, e'p)$ processes [59] under similar approximations. Although PWIA is a severe oversimplification of the semi-inclusive neutrino-nucleus scattering and will certainly fail to describe precisely the experimental data, this approximation allow us to get an analytic expression of the hadronic tensor for some simple nuclear models and reduce the numerical complexity of the calculation for more realistic nuclear models. Hence PWIA calculations will allow us later to check the impact on the semi-inclusive cross section of the different models of the initial nuclear state without complications introduced by FSI, that will be included in a fully quantum and relativistic fashion in later chapters when the comparison with data from different accelerator neutrino experiments is presented.

Since in accelerator-based neutrino experiments the direction of the neutrino is known, we will work in a coordinate system where the neutrino direction is fixed along the z-axis as shown in Fig. 2·3. The sixth-differential CC neutrino-nucleus cross section as function of the neutrino energy and the detected lepton and nucleon kinematics is given by [49, 54]

$$\frac{d\sigma}{dk'd\Omega_{k'}dp_Nd\Omega_N^L} = \frac{(G_F\cos\theta_c k'p_N)^2 m_N}{8k\varepsilon' E_N(2\pi)^6}\int_0^\infty d\mathcal{E}\int d^3p_m \upsilon_0 \mathcal{F}_\chi^2 S\big(p_m, E_m(\mathcal{E}, p_m)\big) \\ \times\delta(M_A + k - \varepsilon' - E_N - \sqrt{p_m^2 + M_{A-1}^2} - \mathcal{E})\delta(\mathbf{k} - \mathbf{k}' - \mathbf{p}_N + \mathbf{p}_m) \tag{2.7}$$

with the final lepton and nucleon solid angles $\Omega_{k'} = (\theta_l, \phi_l)$ and $\Omega_N^L = \big(\theta_N^L, \phi_N^L\big)$, G_F and θ_c the Fermi constant and the Cabibbo angle respectively, $\mathcal{F}_\chi^2 = \frac{2}{\upsilon_0}L_{\mu\nu}\mathcal{W}^{\mu\nu}$ the Lorentz invariant resulting from the contraction of the leptonic tensor $L_{\mu\nu}$ and the single-nucleon hadronic tensor $\mathcal{W}^{\mu\nu}$, $\upsilon_0 = (k + E_l)^2 - q^2$ a kinematical factor and $S\left(p_m, E_m\right)$ the spectral function. The two $\delta-$functions guarantee the energy and momentum conservation (see Eq. (2.1)). Notice that in Eq. (2.7) an integration over unmeasured quantities related with the residual

nucleus is done and that, as pointed out before, in the PWIA there is a clear factorization of the cross section into a part that describes the elementary neutrino-nucleon interaction, contained in $\mathcal{F}_\chi^2$, and the spectral function $S(p_m, E_m)$, that depends on the nuclear model used for the description of the initial state. The single-nucleon hadronic tensor $\mathcal{W}^{\mu\nu}$ in PWIA can be constructed supposing that the initial and final nucleons are described by free positive-energy Dirac spinors. The detailed calculation of $\mathcal{W}^{\mu\nu}$ can be found in Appendix A. Additionally, in Appendix B we provide the analytic expression of $\mathcal{F}_\chi^2$ and the nuclear responses it depends on. The spectral function $S(E_m, p_m)$ in Eq. (2.7) can be related to the nuclear momentum distribution $n(p_m)$ using its definition

$$n(p_m) = \int_0^\infty dE_m S(E_m, p_m), \tag{2.8}$$

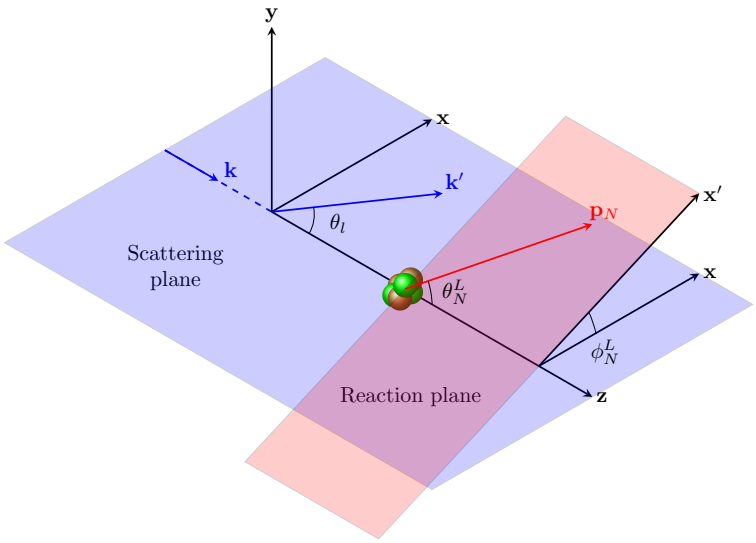

Figure 2·3: Definition of the coordinate system where the direction of the incoming neutrino k is fixed along the z-axis. The leptons are contained in the denominated scattering plane, while the ejected nucleon with momentum p_N and polar angle with respect to the neutrino direction θ_N^L is contained in the so-called reaction plane, which forms an angle ϕ_N^L with the scattering plane.

and taking into account that the momentum distribution is normalized as follows

$$\mathcal{N} = \frac{1}{(2\pi)^3} \int_0^\infty dp_m p_m^2 n\left(p_m\right) \tag{2.9}$$

with $\mathcal{N}$ the number of nucleons that participate in the scattering. In our case, since we will focus in the analysis of CCν reactions, this is the number of neutrons in the target nucleus.

The Eq. (2.7) depends on the kinematics of the final lepton and nucleon detected and assumes that the neutrino energy k is known, hence ω and q are also known and fixed. However, to compare theoretical semi-inclusive predictions with experimental measurements it is necessary to take into account that in accelerator-based neutrino experiments the neutrino beam does not have a well-defined energy. In Fig. 2·4 we show ν_μ flux predictions for different neutrino experiments, which can be separated in low-energy, *i.e.* T2K, MiniBooNE, or NINJA, and high-energy, *i.e.* MINERνA or DUNE, experiments. As a consequence of these broad neutrino fluxes, one needs to integrate the cross section over all the possible energies weighted by the normalized experimental neutrino flux $P(k)$ in order to compare with the experimental data. Using the energy and momentum conservation to integrate over $\mathcal{E}$ and $\mathbf{p_m}$ in Eq. (2.7), the flux-averaged semi-inclusive cross section can be expressed as

$$\left\langle \frac{d\sigma}{dk' d\Omega_{k'} dp_N d\Omega_N^L} \right\rangle = \frac{(G_F \cos\theta_c k' p_N)^2 m_N}{8\varepsilon' E_N (2\pi)^6} \int_0^\infty dk \frac{P(k)}{k} v_0 \mathcal{F}_\chi^2 S\big(p_m, E_m(\mathcal{E}, p_m)\big), \tag{2.10}$$

where

$$\begin{aligned} p_m &= \left|\mathbf{k'} + \mathbf{p_N} - \mathbf{k}\right|, \\ \mathcal{E} &= M_A + k - E_l - E_N - \sqrt{p_m^2 + M_{A-1}} \\ &\approx k - E_l - E_N + m_N - E_s, \end{aligned} \tag{2.11}$$

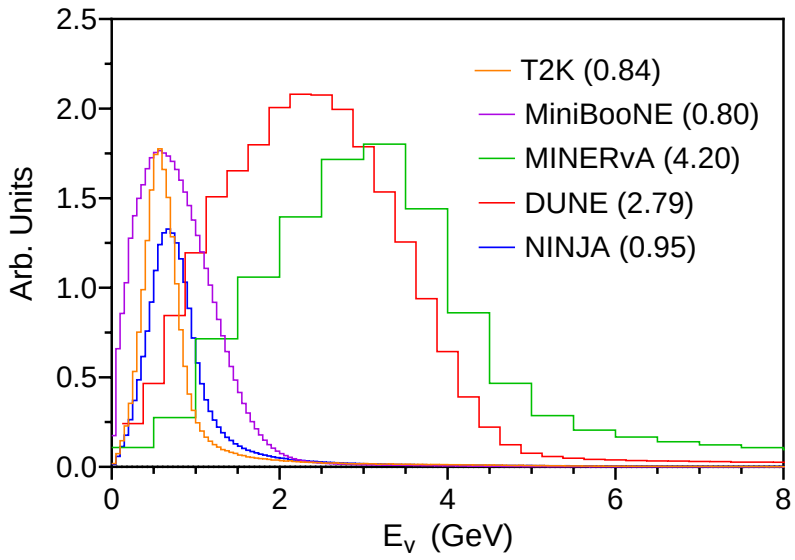

Figure 2·4: ν_μ flux predictions of different neutrino experiments normalized to arbitrary units. The mean neutrino energy (in GeV) for each experiment is given in brackets.

are fixed by conservation. The last ingredient necessary to fully characterize the flux-averaged semi-inclusive neutrino-nucleus cross section in PWIA given in Eq. (2.10) is the spectral function $S(E_m, p_m)$ which incorporates all the initial nuclear state dynamics of the reaction. In the next section, we discuss different nuclear models spanning from the most simple one, where the nucleons do not interact, to more realistic models of nuclear structure that include spectroscopic factors, shell structure and depletion of energy levels due to NN correlations.

2.3 Nuclear models

2.3.1 Relativistic Fermi Gas model

The Relativistic Fermi Gas (RFG) model is the simplest nuclear model, but it is fully relativistic. In this model the nucleus is described as an infinite gas of non-interacting on-shell nucleons. In its ground state, all the single-particle levels are occupied by the nucleons up to the Fermi momentum k_F, while all the states above k_F are empty. The separation

energy of the RFG model is given [60]

$$E_s^{RFG} = -T_F = -E_F + m_N, \tag{2.12}$$

with $E_F = \sqrt{k_F^2 + m_N^2}$ the Fermi energy and T_F the corresponding kinetic energy. The separation energy defined above is nonphysical because it is negative, however one can shift the RFG energies by a constant to move the top of the Fermi sea, *i.e.* the occupied Fermi level, to coincide with a separation energy $-E_s$ [49]. This is equivalent to breaking the on-shell condition of the RFG nucleons by modifying their energies as follows

$$\overline{E} = \sqrt{p_m^2 + m_N^2} \to \overline{E} - (E_F + E_s)\,. \tag{2.13}$$

Considering that the intermediate boson transfers an energy ω to an off-shell nucleon within the Fermi sea which is knocked out of the nucleus with energy $\sqrt{p_N^2 + m_N^2}$, then the energy conservation dictates

$$\omega + \overline{E} - E_F - E_s = \sqrt{p_N^2 + m_N^2} - m_N. \tag{2.14}$$

Taking the limit $p_m << M_{A-1}$ in Eq. (2.5) allow us to identify $\mathcal{E} = E_F - \sqrt{p_m^2 + m_N^2}$ for the RFG model which, since $0 \leq p_m \leq k_F$, is non-negative as it should be. Within the RFG model, it is possible to construct the full $A-$body, covariant, antisymmetrized wave function that describes the ground state of the target nucleus, and the same goes for the residual nucleus left after removing a nucleon. Hence one can evaluate the matrix elements necessary to compute the spectral function of the RFG model that yields [49, 60]

$$S_{RFG}\left(p_m, \mathcal{E}\right) = \frac{3\left(2\pi\right)^3 \mathcal{N}}{k_F^3} \theta\left(k_F - p_m\right) \delta\left(\mathcal{E} - E_F + \sqrt{p_m^2 + m_N^2}\right), \tag{2.15}$$

where the step function $\theta\left(k_F - p_m\right)$ is one for zero or positive arguments and zero for negative arguments, therefore in this case it ensures that the Fermi condition $p_m \leq k_F$ is satisfied. Using the relation between the spectral function and the momentum distribution given in Eq. (2.8), it is trivial to prove that the momentum distribution of the RFG model is

$$n_{RFG}\left(p_m\right) = \frac{3\left(2\pi\right)^3 \mathcal{N}}{k_F^3}\theta\left(k_F - p_m\right), \tag{2.16}$$

which is a constant up to $p_m = k_F$ and then drops to zero. Once known the expression of the spectral function of the RFG model, we can insert Eq. (2.15) into Eq. (2.7), and calculate the flux-averaged semi-inclusive cross section for the RFG model that yields

$$\begin{aligned}\left\langle \frac{d\sigma}{dk' d\Omega_{k'} dp_N d\Omega_N^L} \right\rangle =& \frac{3\mathcal{N}(G_F \cos\theta_c m_N k' p_N)^2}{8(2\pi k_F)^3 \varepsilon' E_N} \int_0^\infty dk \frac{P(k)}{k} \frac{\upsilon_0 \mathcal{F}_\chi^2}{\sqrt{p_m^2 + m_N^2}} \\ &\times \delta\left(\omega - E_s - T_F - \sqrt{p_N^2 + m_N^2} + \sqrt{p_m^2 + m_N^2}\right)\theta(k_F - p_m)\theta(p_N - k_F)\,,\end{aligned} \tag{2.17}$$

where the relativistic factor $m_N/\overline{E}$ [49] and the θ-function $\theta\left(p_N - k_F\right)$ that imposes the Pauli principle, *i.e.* since all the states below k_F are occupied the ejected nucleon momentum must be necessarily bigger or equal than k_F, have been included. Defining the following variables

$$\mathbf{p}_B = \mathbf{k}' + \mathbf{p}_N, \tag{2.18}$$

$$E_B = E_l + E_s + T_F + E_N, \tag{2.19}$$

the delta function can be recast into

$$\delta\left(k - E_B + \sqrt{(\mathbf{p}_B - \mathbf{k})^2 + m_N^2}\right) = \frac{\sqrt{(\mathbf{p}_B - \mathbf{k})^2 + m_N^2}}{E_B - p_B \cos\theta_B}\delta(k - k_0) \tag{2.20}$$

with

$$k_0 = \frac{E_B^2 - p_B^2 - m_N^2}{2\big(E_B - p_B \cos\theta_B\big)}, \tag{2.21}$$

$$\cos\theta_B = \frac{k' \cos\theta_l + p_N \cos\theta_N^L}{p_B}\,. \tag{2.22}$$

Then the flux-averaged semi-inclusive cross section of the RFG model is reduced to

$$\left\langle \frac{d\sigma}{dk' d\Omega_{k'} dp_N d\Omega_N^L} \right\rangle = \frac{3\mathcal{N}(G_F \cos\theta_c m_N k' p_N)^2}{8(2\pi k_F)^3 \varepsilon' E_N} \frac{P(k_0)}{k_0} \frac{\upsilon_0 \mathcal{F}_\chi^2}{E_B - p_B \cos\theta_B} \theta(k_F - p_m)\theta(p_N - k_F) \tag{2.23}$$

with the missing momentum p_m fixed by momentum conservation

$$p_m^2 = k_0^2 - 2k'k_0\cos\theta_l + k'^2 + p_N^2 - 2k_0 p_N \cos\theta_N^L + 2k' p_N(\cos\theta_l \cos\theta_N^L + \sin\theta_l \sin\theta_N^L \cos\phi_N^L). \tag{2.24}$$

2.3.2 Independent-particle shell model

In the independent-particle shell model (IPSM) the nucleons inside the target nucleus occupy discrete energy states that are eigenvalues of a spherically symmetrical potential. The specific choice of potential could vary from a simple harmonic oscillator up to a complicated microscopic potential with realistic NN interactions. In our case, we consider a fully relativistic framework, and describe the bound nucleons as solutions of the Dirac equation with scalar and vector potentials that are given by the relativistic mean field (RMF) approach [61, 62, 63]. This completely relativistic description of finite nuclei, that relies on the mean-field approximation which is only valid for high nuclear densities, is expanded in more detail in Appendix C. The general relativistic wave function solution of the Dirac equation with the

scalar $S(r) = g_\sigma \sigma(r)$ and vector $V(r) = g_\omega \omega^0(r) + g_\rho \tau_3 \rho_3^0(r) + eA^0(r)$ potentials is

$$\Psi(\mathbf{r}) = \begin{pmatrix} g_\kappa(r)\Phi_\kappa^\mu(\hat{\mathbf{r}}) \\ i f_\kappa(r)\Phi_{-\kappa}^\mu(\hat{\mathbf{r}}) \end{pmatrix} \tag{2.25}$$

with

$$\Phi_\kappa^\mu(\hat{\mathbf{r}}) = \sum_{mm'} < l\, m\, \frac{1}{2}\, m' \,|\, j\, \mu > Y_l^m(\hat{\mathbf{r}})\chi_{m'}, \tag{2.26}$$

$j = |\kappa| - 1/2$, $l = \kappa$ if $\kappa > 0$ and $l = -\kappa - 1$ if $\kappa < 0$, m and m' are the projections of the angular momentum l and the spin $s = 1/2$, respectively, $\chi_{m'}$ is a Pauli spinor of two components, and the radial functions $g_\kappa(r)$ and $f_\kappa(r)$ satisfy the following coupled differential equations

$$\begin{aligned} \frac{df_\kappa}{dr} &= \frac{\kappa - 1}{r} f_\kappa - [E - m_N - S(r) - V(r)]\, g_\kappa \\ \frac{dg_\kappa}{dr} &= -\frac{\kappa + 1}{r} g_\kappa + [E + m_N + S(r) - V(r)]\, f_\kappa. \end{aligned} \tag{2.27}$$

The relativistic wave function of a bound nucleon in momentum space can be related using the Fourier transform with the equivalent in coordinate space and is given by

$$\Psi_{\kappa_b}^{\mu_b}(\mathbf{p}) = \frac{1}{(2\pi)^{3/2}} \int d\mathbf{r} e^{-i\mathbf{p}\cdot\mathbf{r}} \Psi_{\kappa_b}^{\mu_b}(\mathbf{r}) = (-i)^{l_b} \begin{pmatrix} g_{\kappa_b}(p) \\ S_{\kappa_b} f_{\kappa_b}(p) \frac{\boldsymbol{\sigma}\cdot\mathbf{p}}{p} \end{pmatrix} \Phi_{\kappa_b}^{\mu_b}(\hat{\mathbf{p}}), \tag{2.28}$$

where $S_{\kappa_b} = \kappa_b/|\kappa_b|$ and $\Phi_{\kappa_b}^{\mu_b}(\hat{\mathbf{p}})$ is defined as in Eq. (2.26) and satisfies the relation

$$\Phi_{-\kappa_b}^{\mu_b}(\hat{\mathbf{p}}) = -\frac{\boldsymbol{\sigma}\cdot\mathbf{p}}{p} \Phi_{\kappa_b}^{\mu_b}(\hat{\mathbf{p}}) \tag{2.29}$$

with $\boldsymbol{\sigma}$ a row vector containing the Pauli matrices. Finally, the radial functions g_{κ_b} and f_{κ_b} in momentum space can be obtained from the respective functions in coordinate space

$$g_{\kappa_b}(p) = \sqrt{\frac{2}{\pi}} \int_0^\infty dr r^2 g_{\kappa_b}(r) j_{l_b}(pr)$$
$$f_{\kappa_b}(p) = \sqrt{\frac{2}{\pi}} \int_0^\infty dr r^2 f_{\kappa_b}(r) j_{\bar{l}_b}(pr) \tag{2.30}$$

with j_{l_b} the Riccati-Bessel functions and $\bar{l}_b = \kappa_b - 1$ if $\kappa_b > 0$ and $\bar{l}_b = |\kappa_b|$ if $\kappa_b < 0$. The normalization of the relativistic wave functions in either space is imposed by the condition

$$\int dr\, r^2 \big(g^2_{\kappa_b}(r) + f^2_{\kappa_b}(r)\big) = \int dp\, p^2 \big(g^2_{\kappa_b}(p) + f^2_{\kappa_b}(p)\big) = 1. \tag{2.31}$$

Since the full relativistic wave function describing the bound nucleon has components that are coupled not only to the free positive-energy Dirac spinors $u(p,s)$ but also to the free negative-energy ones $v(p,s)$, the one-body hadronic current constructed with Eq. (2.28) describing the initial nucleon and a free positive-energy Dirac spinor $u(p_N, s')$ describing the ejected nucleon will yield the corresponding hadronic tensor in the relativistic plane-wave impulse approximation (RPWIA). To recover the PWIA, one needs to drop the contributions coming from the negative-energy spinors by using the positive-energy projector. In this way, it can be shown [59] that the momentum distribution associated only to the positive-energy projection of the full relativistic wave function is

$$n\,(p) = \frac{\overline{E} + m_N}{8\pi m_N} \big|\alpha_{\kappa_b}(p)\big|^2 \tag{2.32}$$

where

$$\alpha_{\kappa_b}(p) = g_{\kappa_b}(p) - \frac{p}{\overline{E} + m_N} S_{\kappa_b} f_{\kappa_b}(p). \tag{2.33}$$

Assuming that the discrete states occupied by the nucleons, commonly known as shells, are characterized by the usual quantum numbers n, l, j with an associated bound energy $-E_{nlj}$, the spectral function will be given simply by

$$S_{IPSM}\left(p_m, \mathcal{E}\right) = \sum_{n,l,j} \left(2j+1\right) n_{nlj}\left(p_m\right) \delta\left(\mathcal{E} + E_s - E_{nlj}\right), \tag{2.34}$$

where $n_{nlj}(p_m)$ is the positive-energy RMF momentum distribution given in Eq. (2.32), the sum is extended to all the occupied shells (n, l, j), *i.e.*, $\sum_j (2j+1) = \mathcal{N}$, and the energy conservation states $\mathcal{E} = E_{nlj} - E_s$; hence the separation energy in the IPSM is the energy of the highest shell. Lastly, one can notice that the normalization of the relativistic wave function in Eq. (2.31) is broken when the negative-energy components are dropped to construct the positive-energy momentum distribution in Eq. (2.32). However, the overall contribution of the negative-energy component and its interference term with the positive-energy component is rather small $(2\% - 3\%)$ [59] and in our case a renormalization of Eq. (2.32) is performed to compensate the lack of negative-energy contributions and also to satisfy the normalization adopted in Eq. (2.9). Introducing Eq. (2.34) into Eq. (2.10) one can get the flux-averaged semi-inclusive cross section for the IPSM

$$\left\langle \frac{d\sigma}{dk' d\Omega_{k'} dp_N d\Omega_N^L} \right\rangle = \frac{(G_F \cos\theta_c k' p_N)^2 m_N}{8(2\pi)^6 \varepsilon' E_N} \sum_{n,l,j} (2j+1) \frac{P(k_{nlj})}{k_{nlj}} \upsilon_0 \mathcal{F}_\chi^2 n_{nlj}(p_m), \tag{2.35}$$

where the neutrino energy

$$k_{nlj} = E_l + E_N - m_N + E_{nlj} \tag{2.36}$$

and the missing momentum

$$\begin{aligned} p_m^2 = {} & k_{0nlj}^2 + k'^2 + p_N^2 - 2k_{0nlj}k' \cos\theta_l - 2k_{0nlj} p_N \cos\theta_N^L \\ & + 2k' p_N (\cos\theta_l \cos\theta_N^L + \sin\theta_l \sin\theta_N^L \cos\phi_N^L) \end{aligned} \tag{2.37}$$

are fixed by energy conservation.

2.3.3 Natural orbitals shell model

The Natural orbitals (NO) shell model is presented as an extension of the IPSM specially constructed to create a realistic spectral function that leads to a good agreement with the scaling function extracted from the analysis of inclusive electron-nucleus scattering data [64, 65]. The model starts from the simple IPSM spectral function given in Eq. (2.34), which can be rewrite as

$$S_{IPSM}(p_m, \mathcal{E}) = \sum_i (2j_i + 1) n_i(p_m) \delta\left(\mathcal{E} - \mathcal{E}_i\right), \tag{2.38}$$

where the sum i runs up to the last shell occupied with eigenvalue $\mathcal{E}_i$. Then, effects beyond the mean field approximation are included by replacing the δ-function in Eq. (2.38) by a function with finite width in energy like a Lorentzian function

$$L_{\Gamma_i}(\mathcal{E} - \mathcal{E}_i) = \frac{1}{2\pi} \frac{\Gamma_i}{(\mathcal{E} - \mathcal{E}_i)^2 + (\Gamma_i/2)^2}, \tag{2.39}$$

where Γ_i is the width of the i single-particle state, and by using single-particle wave functions that diagonalize the one-body density matrix [66]

$$\rho(\mathbf{r}, \mathbf{r}') = \sum_a N_a \psi_a^*(\mathbf{r}) \psi_a(\mathbf{r}'). \tag{2.40}$$

The NO single-particle wave functions in Eq. (2.40), that include short-range NN correlations, are used to obtain the natural occupation numbers N_α and the wave functions in momentum space, *i.e.*, the momentum distributions. The NO spectral function is then given by [67]

$$S_{NO}(p_m, \mathcal{E}) = \frac{1}{2\pi A} \sum_i (2j_i + 1) N_i \left|\psi_i(p_m)\right|^2 L_{\Gamma_i}(\mathcal{E} - \mathcal{E}_i), \tag{2.41}$$

where the single-particle NO momentum distributions $\left|\psi_i(p)\right|^2$ are normalized according to Eq. (2.9). The flux-averaged semi-inclusive cross section associated to this model is

$$\left\langle \frac{d\sigma}{dk' d\Omega_{k'} dp_N d\Omega_N^L} \right\rangle = \int d\mathcal{E} \frac{(G_F \cos\theta_c k' p_N)^2 m_N P(k)}{8k\varepsilon' E_N (2\pi)^7 A} \times \sum_i (2j_i+1) N_i |\psi_i(p_m)|^2 L_{\Gamma_i}(\mathcal{E}-\mathcal{E}_i) v_0 \mathcal{F}_\chi^2 \,, \tag{2.42}$$

where the neutrino and missing momenta are fixed by conservation

$$\begin{aligned} k &= E_s + E_N + E_l - m_N + \mathcal{E}, \\ p_m^2 &= k^2 + k'^2 + p_N^2 - 2kk'\cos\theta_l - 2kp_N\cos\theta_N^L 2k' p_N (\cos\theta_l \cos\theta_N^L + \sin\theta_l \sin\theta_N^L \cos\phi_N^L) \,. \end{aligned} \tag{2.43}$$

Notice that in the NO model, the substitution of the δ-function by $L_{\Gamma_i}(\mathcal{E}-\mathcal{E}_i)$ in Eq. (2.41) does not allow us to solve the integral over $\mathcal{E}$ analytically, like for the previous nuclear models, hence the integral has to be performed numerically.

2.3.4 Rome spectral function model

One of the most realistic and complete descriptions of nuclear targets commonly used in accelerator-neutrino experiments is given by the so-called Rome spectral function model [58, 68], usually referred just as Rome or spectral function (SF) model within the neutrino community. In the SF model, the nuclear spectral function is split in two parts

$$S_{\text{Rome}}(p_m, E_m) = S_{\text{SP}}(p_m, E_m) + S_{\text{corr}}(p_m, E_m) \,, \tag{2.44}$$

the single-particle contribution $S_{\text{SP}}(p_m, E_m)$ that gives the bulk contribution to the spectral function for missing energies up to $\sim$ 40 MeV and missing momenta up to $\sim$ 250 − 300 MeV and the correlated contribution $S_{\text{corr}}(p_m, E_m)$. This correlated part shows a

widespread background extending up to large values of both E_m and p_m. This is in contrast to $S_{SP}\,(p_m, E_m)$, which has a tail that is typically extended just above the Fermi level and is sharply peaked in E_m around the bound energy values of the single-particle states in the nuclear shell model. The correlated part of the spectral function arises from contributions of configurations having pairs of strongly correlated nucleons, which are mostly sensitive to the short-range NN interaction. Since it is expected that the correlated part of the spectral is only mildly affected by finite-size effects, this part is extracted from a calculation in nuclear matter which is recalculated for finite nuclei employing the local-density approximation (LDA) [68]. The SF model employs $(e, e'p)$ experimental data (e.g. Saclay [69] for ^{16}O) to parametrize $S_{\rm SP}\,(p_m, E_m)$ in the following way

$$S_{\rm SP}\,(p_m, E_m) = \sum_n Z_n \left|\phi_n(p_m)\right|^2 F_n\,(E_m - E_n)\,, \tag{2.45}$$

where $\phi_n(p_m)$ is the wave function describing the single-particle states in momentum space, which is usually fitted to experimental data with Woods-Saxon wave functions, $F_n(E_m - E_n)$ is the width of the single-particle states (e.g. Lorentzian- or Gaussian-shaped function) and Z_n is the spectroscopic factor that gives the normalization of the n shell. From the analysis of $(e, e'p)$ data it has been shown that $Z_n < 1$ and that the single-particle part of the spectral function accounts for $70 - 80\%$ of the total normalization, while the remaining $20 - 30\%$ is associated to the correlated part. The ^{12}C and ^{16}O spectral functions calculated using this approach are shown in Fig. 2·5 and the flux-averaged semi-inclusive cross section associated to this model is obtained by simply introducing Eq. (2.44) in Eq. (2.10)

$$\left\langle \frac{d\sigma}{dk' d\Omega_{k'} dp_N d\Omega_N^L} \right\rangle = \frac{(G_F \cos\theta_c k' p_N)^2 m_N}{8\varepsilon' E_N (2\pi)^6} \int_0^\infty dk \frac{P(k)}{k} \upsilon_0 \mathcal{F}_\chi^2 S_{\rm Rome}\,(p_m, E_m)\,. \tag{2.46}$$

To see more clearly the differences between the nuclear models, Fig. 2·6 shows the momentum distribution $n(p_m)$ of ^{12}C for all the models described in this section. As already

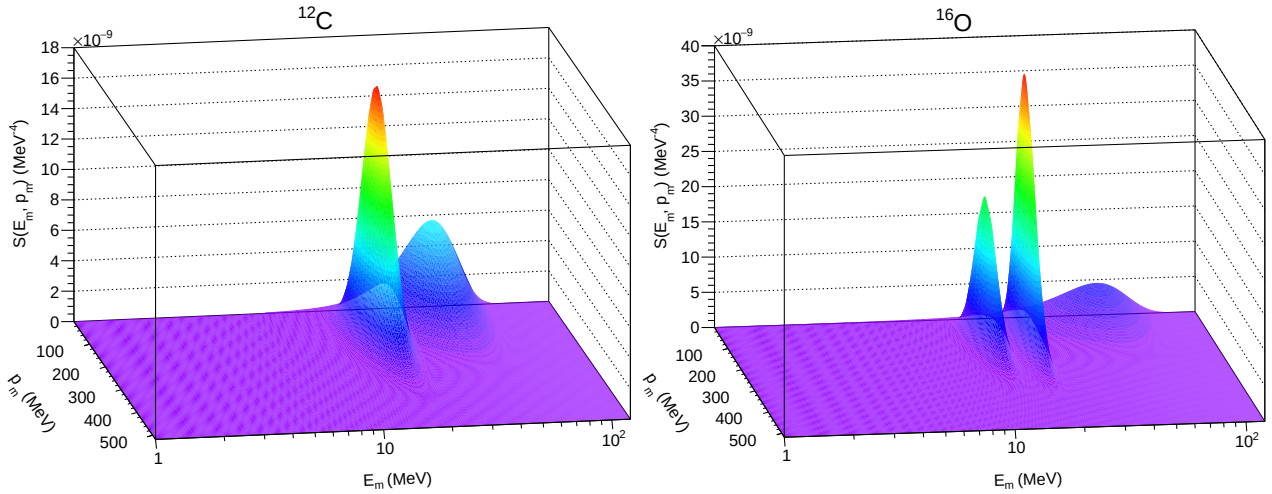

Figure 2·5: 3-D plot of the carbon (left) and oxygen (right) spectral functions calculated using the Rome approach [58, 68], *i.e.* the single-particle contribution extracted from the analysis of $(e, e'p)$ experimental data and using the LDA for the correlated part.

mentioned above, the RFG momentum distribution is constant up to k_F and then drops to zero, whereas the other models display a more complex shape characterized by tails that extend beyond k_F. Also it can be seen that the NN correlations included in the Rome momentum distribution significantly increase the strength of the distribution for large values of p_m. This effect is observed also for the NO model when it is compared to IPSM distribution, although this additional contribution is smaller than in the Rome case.

2.4 Semi-inclusive neutrino-nucleus cross section in PWIA

In the previous sections the flux-averaged semi-inclusive neutrino-nucleus cross section in PWIA for different models of the initial nuclear state was introduced. Since we are trying to understand the differences between the models, in what follows we show semi-inclusive cross sections for some specific kinematics where the dependence of the momentum distribution on the missing momentum is particularly relevant.

We begin considering the CC ν_μ semi-inclusive cross sections for IPSM and RFG model

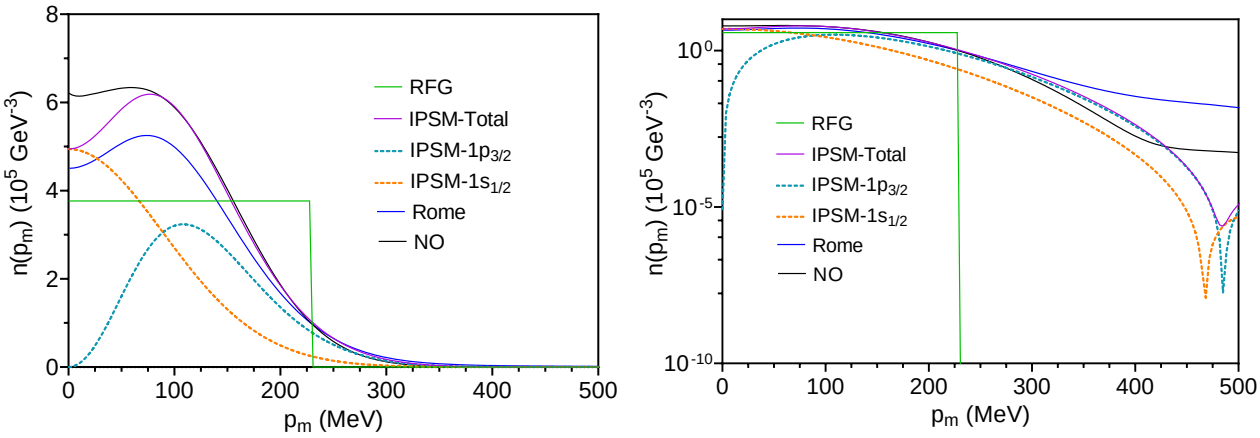

Figure 2·6: Momentum distribution $n(p_m)$ calculated by integrating the spectral function of different nuclear models of ^{12}C. The value of the Fermi momentum for ^{12}C is $k_F = 0.228$ GeV and the individual shells that are included in the IPSM are shown separately. The distributions are shown in linear (left) and semi-logarithmic (right) scales to expose the differences between the models in the low- and high-missing momentum zones.

with muon momentum $k' = 1.5$ GeV, muon scattering angle $\theta_l = 30°$ and two different values for the final proton azimuthal angle, namely $\phi_N^L = 180°$ and $\phi_N^L = 165°$, as function of the ejected proton momentum p_N and the angle θ_N^L. We consider ^{40}Ar as the target and use the neutrino flux corresponding to DUNE. Results for the RFG model are presented in Fig. 2·7 using $k_F = 0.241$ GeV for two different points of view, namely "side" (top panels) and "hawk" (bottom) views. The graphs on the left correspond to $\phi_N^L = 180°$, while the ones on the right to $\phi_N^L = 165°$. In both cases the shape of the cross section is simple being only different from zero in a very well-defined area given by the Fermi condition $p_m \leq k_F$. Notably, compared to the $\phi_N^L = 180°$ scenario, the region where the cross section exists is significantly reduced when $\phi_N^L = 165°$. In the latter kinematics, only a few points in the (p_N, θ_N^L) plane satisfy the condition that the corresponding missing momentum, as defined in Eq. (2.24), is smaller than k_F. Fig. 2·8 shows the semi-inclusive cross sections for the IPSM. For $\phi_N^L = 180°$ (left panels), the shape is more complex compared to the RFG model. The contour appears more diffuse, and the maximum is approximately positioned at the center

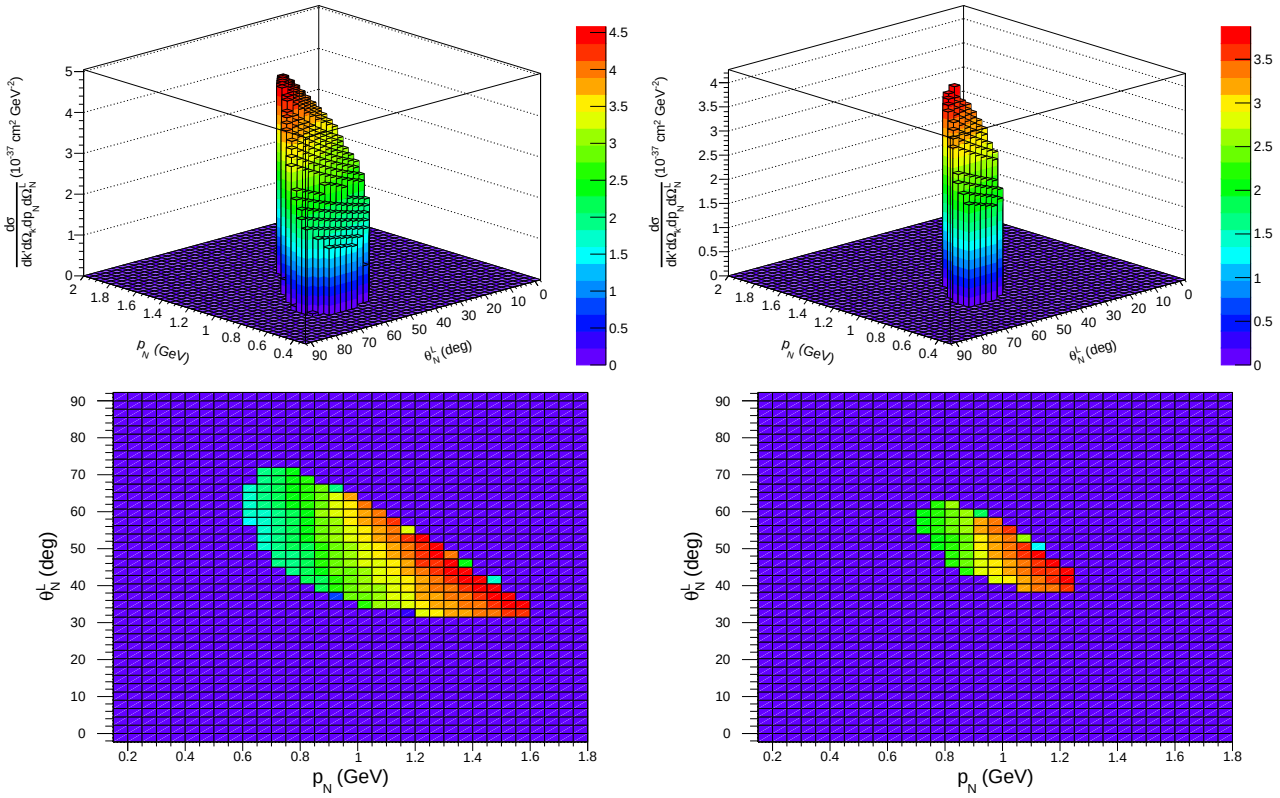

Figure 2·7: Semi-inclusive cross section for ^{40}Ar and DUNE flux with $k' = 1.5$ GeV, $\theta_l = 30°$, $\phi_N^L = 180°$ (left panels) and $\phi_N^L = 165°$ (right panels) using the RFG model.

of the existing cross-section region. However, its distribution clearly differs from the results observed for $\phi_N^L = 165°$ (right panels). Here, the cross section displays a symmetric shape with a well-defined maximum at the center of the projected contour. As one moves away from the center, the magnitude uniformly decreases in all directions. It is noteworthy that the maximum value of the cross section decreases by approximately $\sim 70\%$ when $\phi_N^L = 165°$, in contrast to the corresponding value at $\phi_N^L = 180°$. On the contrary, note that for the RFG model (Fig. 2·7) the reduction is only $\sim 15\%$. This is clearly illustrated in Table 2.1 where the specific values, denoted by $(\tilde{p}_N, \tilde{\theta}_N^L)$, for which the semi-inclusive cross section reaches its maximum for the two ϕ_N^L-angles considered and both nuclear models are summarized. The origin of these features is further investigated in the next plots.

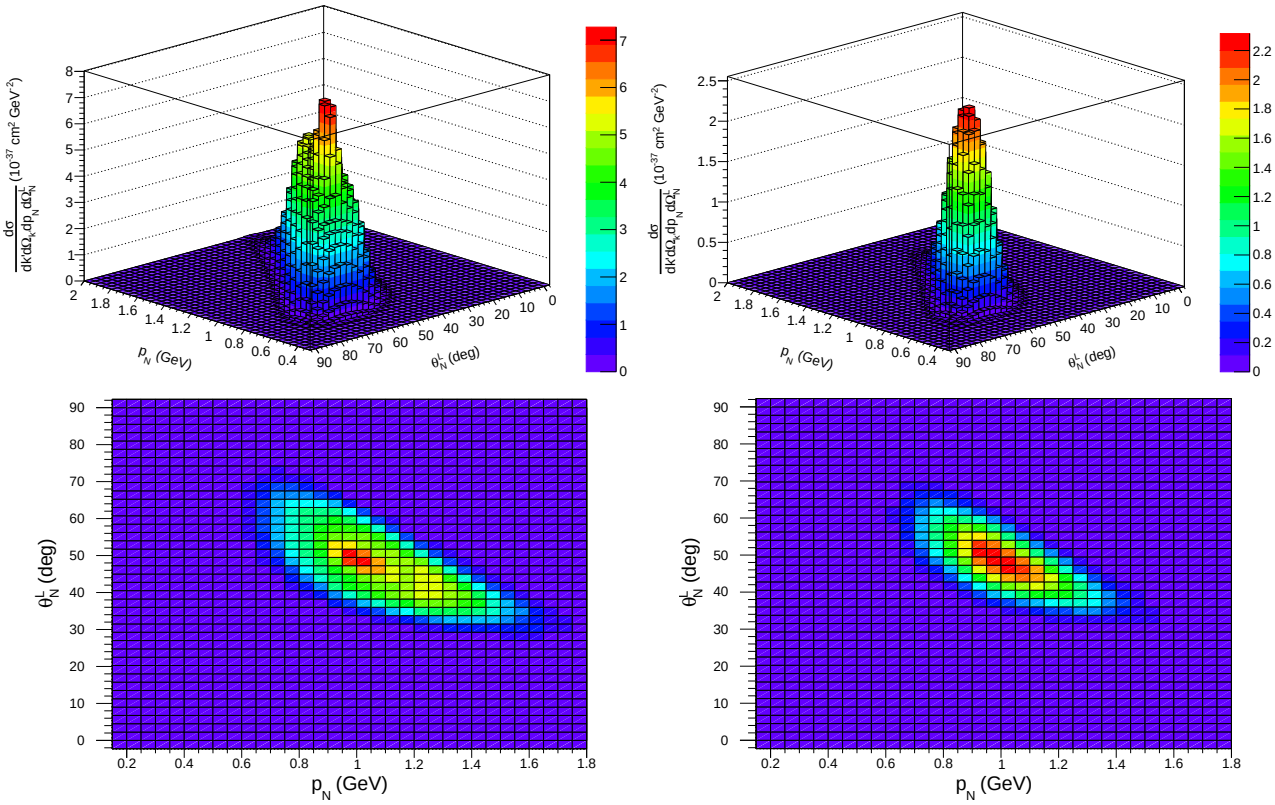

Figure 2·8: Semi-inclusive cross section for ^{40}Ar and DUNE flux with $k' = 1.5$ GeV, $\theta_l = 30°$, $\phi_N^L = 180°$ (left panels) and $\phi_N^L = 165°$ (right panels) using the IPSM.

	$\phi_N^L = 180°$			$\phi_N^L = 165°$		
	$\tilde{p}_N$	$\tilde{\theta}_N^L$	Cross section	$\tilde{p}_N$	$\tilde{\theta}_N^L$	Cross section
RFG	1.43 GeV	43.50°	4.62×10^{-37}	1.24 GeV	42.89°	3.95×10^{-37}
IPSM	1.00 GeV	49.54°	7.56×10^{-37}	1.00 GeV	48.33°	2.32×10^{-37}

Table 2.1: Values of p_N and θ_N^L that give the maximum cross sections in Fig. 2·7 and Fig. 2·8, *i.e.*, $(\tilde{p}_N, \tilde{\theta}_N)$. Cross sections in cm^{2}GeV^{-2}.

Fig. 2·9 shows the semi-inclusive cross sections for the IPSM (red dashed) and the RFG (blue solid) models and the two values of ϕ_N^L. The graphs on the left present the semi-inclusive cross section as a function of the ejected nucleon momentum p_N evaluated at the values of $\tilde{\theta}_N^L$ where the maximum in the cross section occurs in each model. The panels on the right show the corresponding cross sections as function of θ_N^L at fixed $\tilde{p}_N$. Not only the

shapes in the two models completely disagree but also the region in $(p_N,\, \theta_N^L)$ where the cross section is defined differs very significantly.

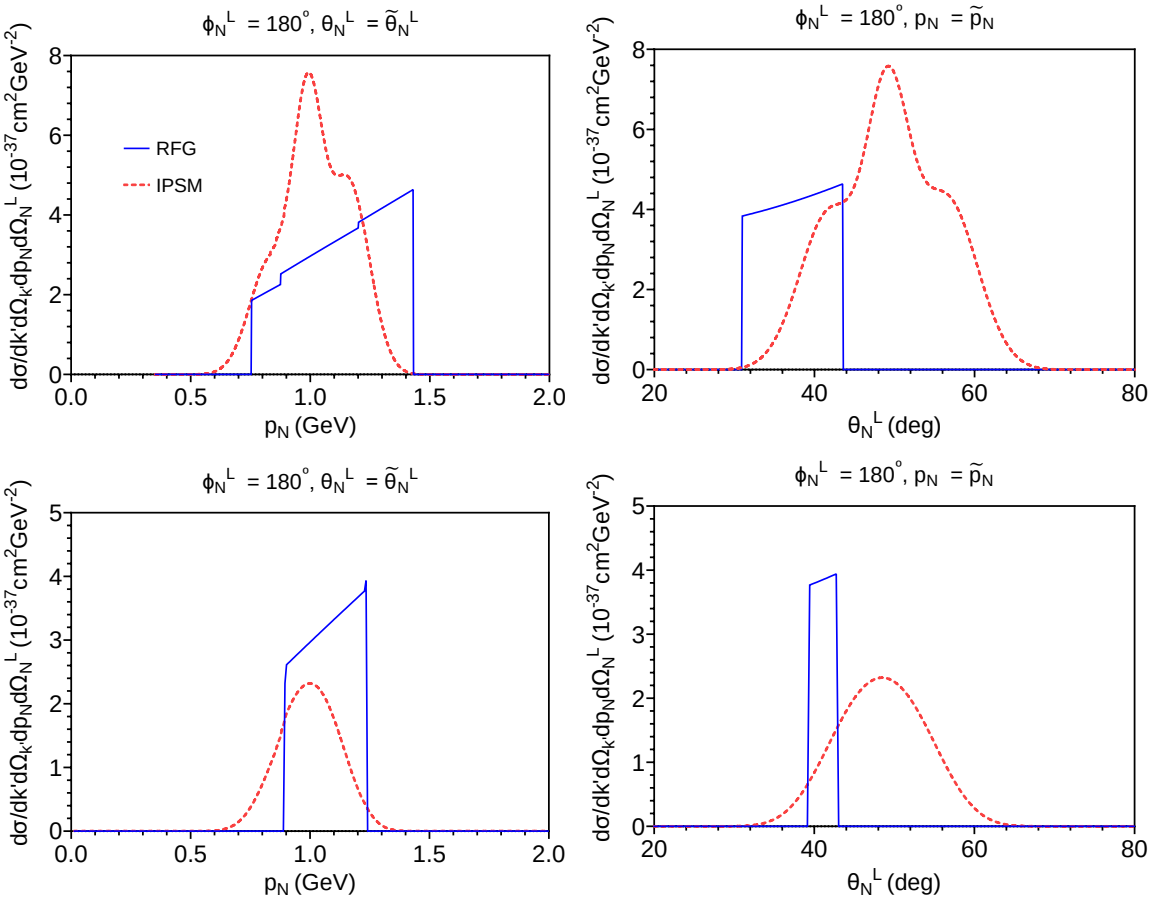

Figure 2·9: Semi-inclusive cross sections as function of p_N (θ_N^L) for the two values considered of the azimuthal angle ϕ_N^L (see text for details). In each case the cross section is evaluated at the corresponding values $\tilde{\theta}_N^L$ ($\tilde{p}_N$) that give the maximum cross section in Figs. 2·7 and 2·8. The values of $\tilde{p}_N$ and $\tilde{\theta}_N^L$ are summarized in Table 2.1.

The specific contribution of the different shells in the IPSM to the semi-inclusive cross section in the case of ^{40}Ar is shown in Fig. 2·10, where a cut in the plane $\theta_N^L = \tilde{\theta}_N^L$ of the semi-inclusive cross section shown in Fig. 2·8 is presented. The left (right) panel in Fig. 2·10 corresponds to $\phi_N^L = 180^\circ$ ($\phi_N^L = 165^\circ$). In both graphs the behavior and allowed values of the missing momentum p_m (solid black line) are shown. According to the ^{40}Ar momentum distribution (see Fig. 2·11), the s-shell contribution is dominant for very low

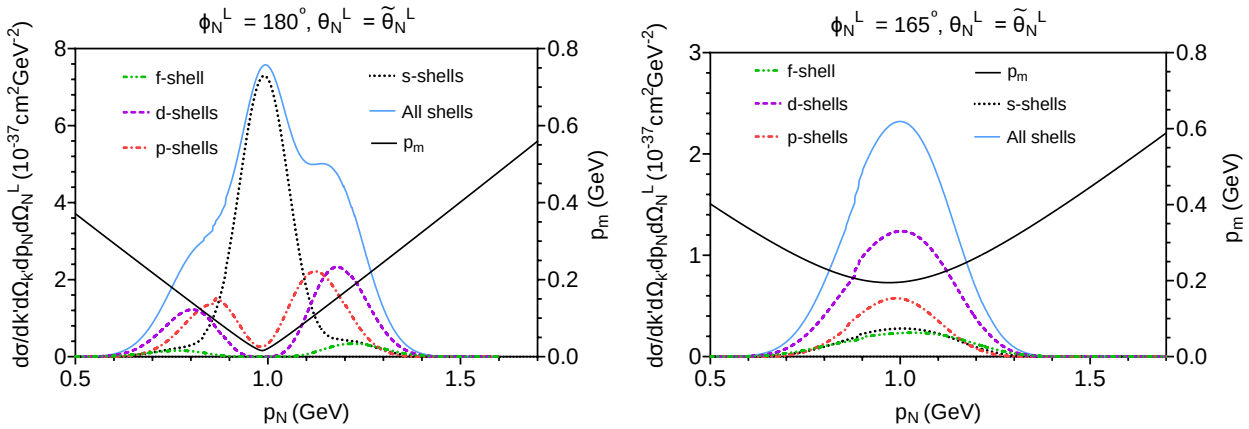

Figure 2·10: (Left axes) Contributions to the semi-inclusive cross section by each shell in the IPSM for ^{40}Ar. The value of $\tilde{\theta}_N^L$ is given in Table 2.1 and the lepton variables are fixed to $k' = 1.5$ GeV and $\theta_l = 30°$. (Right axes) Missing momentum p_m defined in Eq. (2.37) for the IPSM. Since its value is different for each shell, here is shown the average over all the ^{40}Ar shells.

missing momentum. For the kinematics considered in the left panel of Fig. 2·10 this very low-p_m region corresponds to values of the ejected nucleon momentum in the vicinity of p_N = 1.0 GeV ($p_m \sim 40 - 50$ MeV). The other shells give a smaller contribution, generating the secondary peaks observed in Fig. 2·8 at $\phi_N^L = 180°$. These peaks disappear at $\phi_N^L = 165°$ being also the cross section significantly smaller. As shown in the right panel of Fig. 2·10, the missing momentum gets also its minimum value in the region of p_N close to 1 GeV. However, here $p_m \sim 200$ MeV, *i.e.,* much larger than the corresponding value in the previous case. As clearly illustrated by the ^{40}Ar momentum distribution (Fig. 2·11), at $p_m \simeq 200$ MeV the shells that contribute the most are the d and p-ones. This is consistent with the more symmetric shape of the semi-inclusive cross section shown in Fig. 2·8 for $\phi_N^L = 165°$ (right panels) with only one visible peak.

According to the general energy and momentum conservation given by Eqs. (2.1, 2.5), it is possible to obtain an expression for $\mathcal{E}$, or equivalently E_m, as function of p_m for a selected

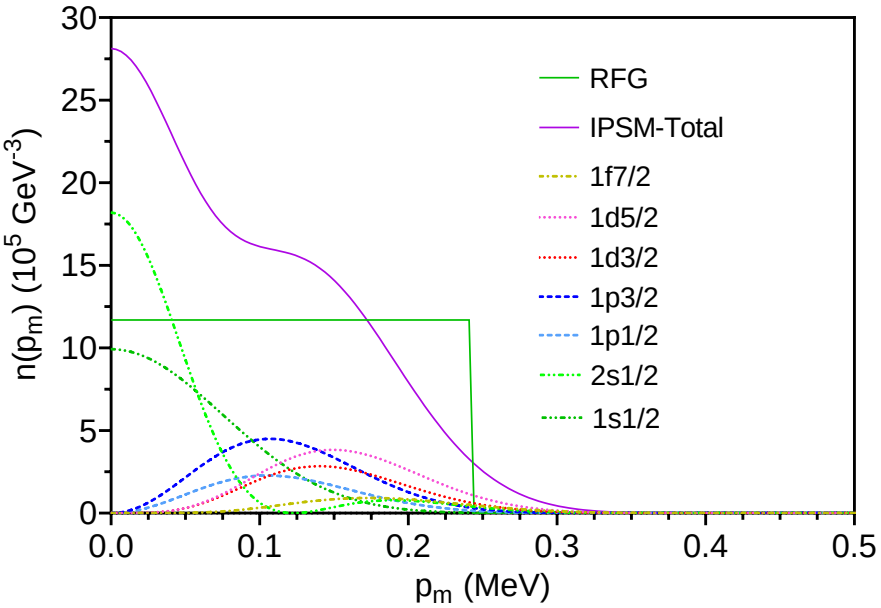

Figure 2·11: IPSM and RFG momentum distributions of ^{40}Ar. The Fermi momentum is set to $k_F = 0.241$ GeV. The contributions from the different shells of the IPSM are shown separately.

set of semi-inclusive variables: (k', θ_l, p_N, θ_N^L, ϕ_N^L). This relation is

$$\mathcal{E}(p_m) = k - \sqrt{k'^2 + m_l^2} - E_s - E_N + m_N \,, \tag{2.47}$$

where the neutrino momentum k is the solution of the equation

$$k^2 - 2k(k'\cos\theta_l + p_N\cos\theta_N^L) + k'^2 + p_N^2 + 2k'p_N(\cos\theta_l\cos\theta_N^L + \sin\theta_l\sin\theta_N^L\cos\phi_N^L) - p_m^2 = 0\,, \tag{2.48}$$

and it defines trajectories in the $(\mathcal{E}, p_m)$ plane allowed by energy conservation at each kinematics. By plotting the trajectories $\mathcal{E}(p_m)$, likewise $E_m(p_m)$, for a set of semi-inclusive variables, one can observe that the RFG (IPSM) CC semi-inclusive cross section is different from zero only if the corresponding trajectory crosses the curve $\mathcal{E}_{RFG}$ ($\mathcal{E}_{nlj}$), where the RFG (IPSM) spectral function lives. This is illustrated in Fig. 2·12 where the trajectories $E_m(p_m)$ for the set of variables that gives the maximum cross sections in Figs. 2·7 and 2·8 together

with $E_m(p_m)$ for the two models are shown. In the case of the IPSM (dashed curves) the two trajectories corresponding to the two ϕ_N^L-values cross the specific missing energies for the different shells at very different values of the missing momentum. Whereas for $\phi_N^L = 180°$ the crossing occurs in the region of low-p_m, *i.e.*, $p_m \simeq 50$ MeV or below, the situation is clearly different for $\phi_N^L = 165°$ where the crossing takes place at larger p_m-values ($p_m \simeq 200$ MeV), a region where the momentum distribution has dropped significantly. This explains the large reduction observed in the maximum of the semi-inclusive cross section when going from $\phi_N^L = 180°$ to $\phi_N^L = 165°$.

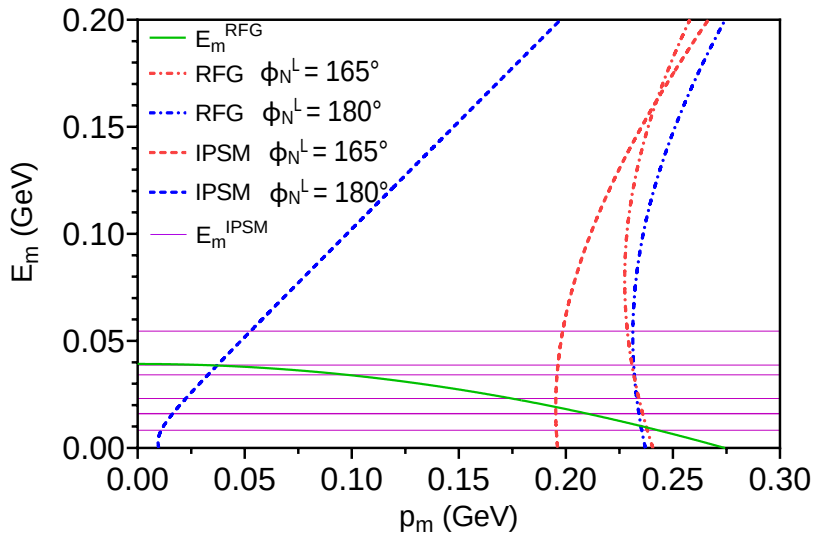

Figure 2·12: Trajectories $E_m\,(p_m)$ given by Eq. (2.47) evaluated at the kinematics that give the maximum cross sections in Figs. 2·7 and 2·8 summarized in Table 2.1. For the RFG $E_m^{RFG} = E_F - \sqrt{p_m^2 + m_N^2} + E_s$, while for the IPSM $E_m^{IPSM} = E_{nlj}$.

The situation is clearly different for the RFG model. Here the trajectories for the two ϕ_N^L-values (dot-dashed lines) closely overlap, intersecting the RFG missing energy at $p_m \simeq 240$ MeV/c, *i.e.,* just below the Fermi level. As known, the RFG momentum distribution is constant and different from zero up to $p_m = k_F$. Thus the 15% reduction observed in the maxima of the semi-inclusive cross sections for the two ϕ_N^L-values cannot be attributed to the momentum distribution itself but rather to the specific kinematic factors (evaluated at

the particular allowed values for the remaining kinematical variables) that enter in the cross section.

Using the general expression for the trajectory $E_m(p_m)$ we can also analyze the origin of the high peak in the cross section shown in Fig. 2·8 for $\phi_N^L = 180°$. Since this result is not present in the case of the RFG (Fig. 2·7), one could assume that its origin is linked to the complex, non-constant, structure shown by the momentum distribution of the IPSM. As already shown in Fig. 2·12, the IPSM trajectory corresponding to $\phi_N^L = 180°$ is consistent with significant contribution to the semi-inclusive cross section by the momentum distribution at low missing momentum values. This is the region where the different s-shells clearly dominate (see Fig. 2·11), giving rise to the maximum in the cross section observed in Fig. 2·8. Therefore if one excludes the s-shells contributions, the semi-inclusive cross section should decrease significantly. This is illustrated in Fig. 2·13 where the contour graph of the semi-inclusive cross section including all shells in ^{40}Ar (left panel) and removing the contribution of the s-shells (right panel) are shown. Note how importantly the strength in the cross section is modified in the (p_N, θ_N^L)-plane. The peak presented in the left panel located in the vicinity of $p_N \simeq 1.0$ GeV and $\theta_N^L \simeq 50°$, due to the s-shell contributions, has completely disappeared in the right panel leaving a hole where the cross section is very small.

All previous results were for ^{40}Ar, the target currently used by MicroBooNE and that will be used in the future by the DUNE collaboration. In what follows the study is extended to the case of ^{12}C, used in past and on-going experiments. The semi-inclusive cross sections for muon neutrinos on ^{12}C are calculated with kinematics fixed to $k' = 0.55$ GeV, $\theta_l = 50°$ and $\phi_N^L = 180°$. The T2K muon neutrinos flux is used to generate the cross sections and, in addition to the RFG and IPSM nuclear models already used in the case of DUNE (^{40}Ar), the predictions using the NO model will be also given. In Fig. 2·14 the semi-inclusive cross sections for the kinematics defined above and the three nuclear models are presented. The shapes of the semi-inclusive cross sections are, like in the ^{40}Ar results, highly correlated with

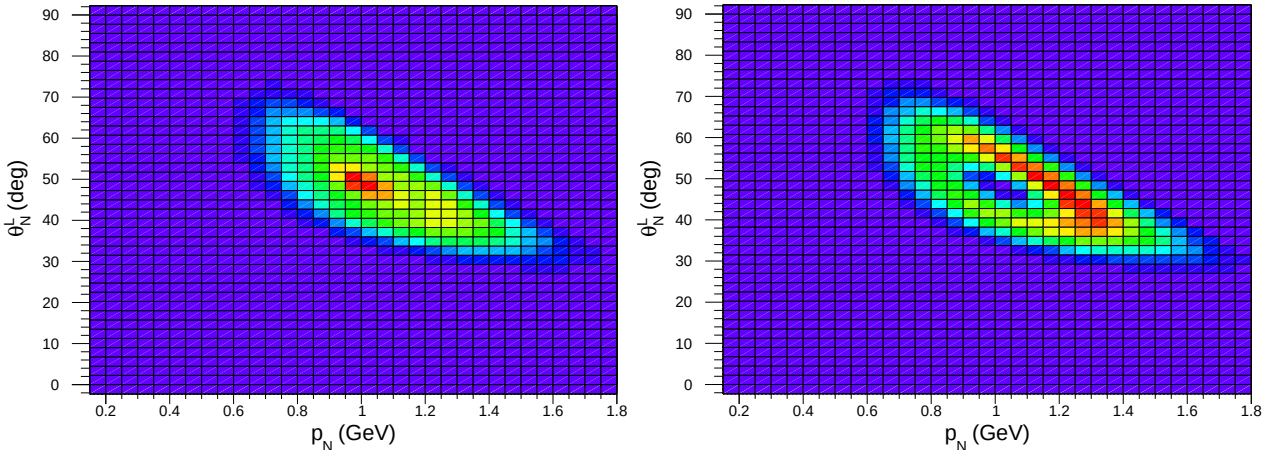

Figure 2·13: Semi-inclusive cross section for ^{40}Ar and DUNE flux with $k' = 1.5$ GeV, $\theta_l = 30^\circ$ and $\phi_N^L = 180^\circ$ using the IPSM including all shells (left panel) and removing the s-shells (right). Cross sections in the same units than the one presented in the top left panel in Fig. 2·8.

the shapes of the ^{12}C momentum distributions (see Fig. 2·6). Notice that the cross section for IPSM in Fig. 2·14 shows a small hole in the center of the region that is not present in the case of the NO model. An analysis of the E_m (p_m) trajectories shows that this particular region in the (p_N, θ_N^L)-plane corresponds to very small values of the missing momentum. Note that the behavior of the momentum distribution for the two models, IPSM and NO, differs at low-p_m: the former decreases as p_m approaches zero whereas the latter does not.

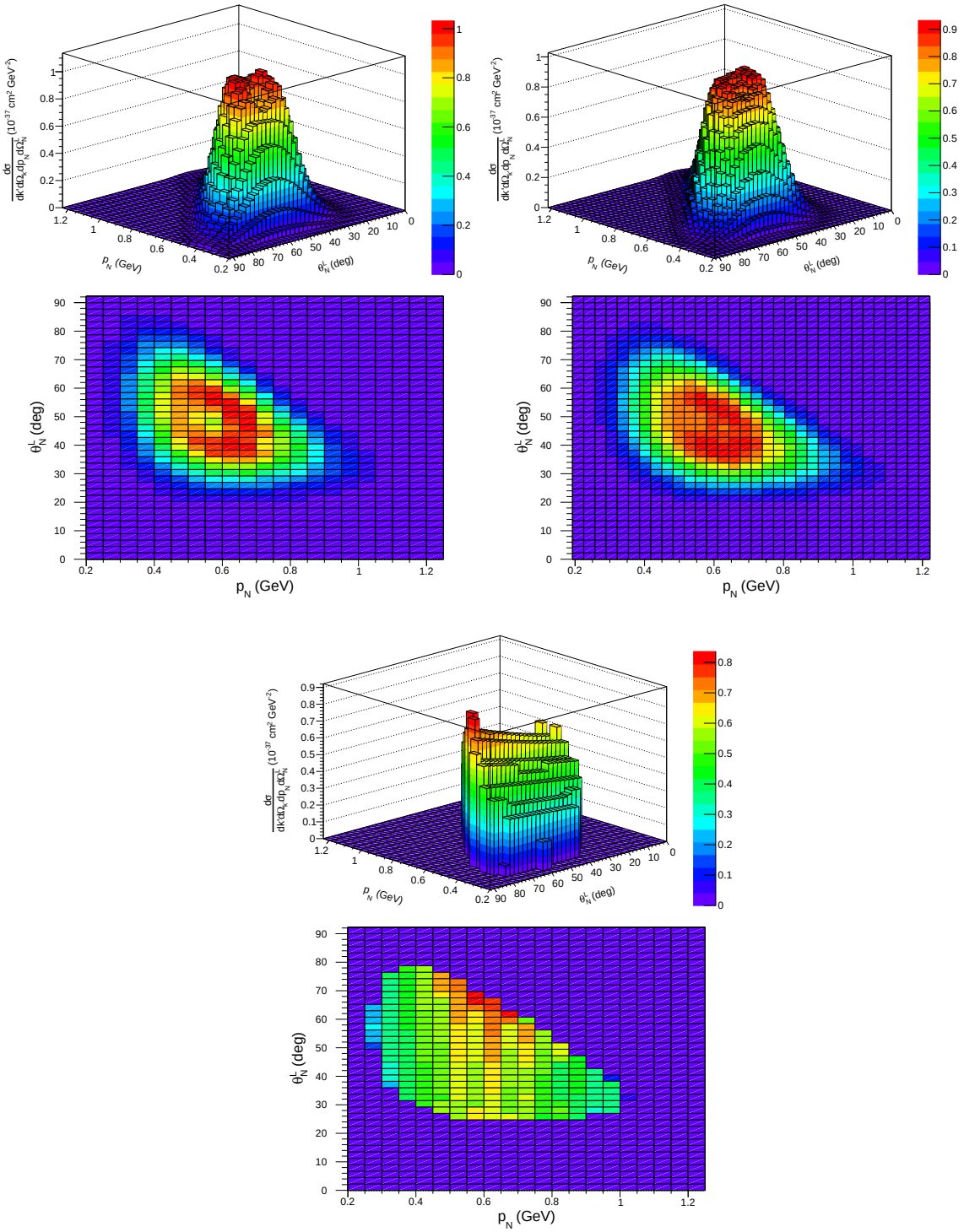

Figure 2·14: Semi-inclusive cross section for ^{12}C and T2K flux with $k' = 0.55$ GeV, $\theta_l = 50°$ and $\phi_N^L = 180°$ using the IPSM (top left panels), NO (top right panels) and RFG (bottom panels) nuclear models.

Chapter 3

The relativistic distorted-wave impulse approximation

In the previous chapter we introduced the semi-inclusive CC neutrino-nucleus cross section in PWIA, *i.e.*, the bound neutron, after exchanging momentum and energy with the virtual boson W^-, is turned into a proton than moves through the residual nucleus without interacting with the remaining $A-1$ nucleons. However, in a real process the proton interacts via the strong and electromagnetic forces on its way out of the residual nucleus. These final-state interactions (FSI) could produce, for instance, transitions to unobserved channels that cause a reduction of the cross section or scattering where the four-momentum of the ejected proton is modified by elastic interactions with the nuclear medium. In general FSI distort the wave function that describes the ejected proton, breaking the relationship between the asymptotic proton momentum (*i.e.* the one that is detected) and the momentum of the bound neutron state. The approach we are adopting to describe FSI for semi-inclusive CC neutrino-nucleus scattering in this thesis is the so-called relativistic distorted-wave impulse approximation (RDWIA), a fully quantum and relativistic approach extensively tested against exclusive $(e, e'p)$ measurements for several nuclei [70, 71, 72] that has been extended to also make predictions of semi-inclusive neutrino-nucleus cross sections [73, 74, 75, 76]. The flux-

averaged semi-inclusive neutrino-nucleus cross section can be written as [73, 74, 75]

$$\left\langle \frac{d\sigma}{dk' d\Omega_{k'} dp_N d\Omega_N^L} \right\rangle = \frac{G_F^2 \cos^2\theta_c k'^2 p_N^2}{64\pi^5} \int dk \frac{W_{A-1}}{E_{A-1} f_{\rm rec}} L_{\mu\nu} H^{\mu\nu} P(k), \tag{3.1}$$

where the recoil factor is given by

$$f_{\rm rec} = \left| 1 - \frac{\mathbf{p_m} \cdot \hat{z}}{E_{A-1}} \right|. \tag{3.2}$$

Notice that the integral over the neutrino momentum k in Eq. (3.1) is equivalent to the integral over the missing energy E_m because they are related through the energy-momentum conservation:

$$E_m = W_{A-1} + m_N - M_A = k - E_l + m_N - E_N - T_{A-1} \tag{3.3}$$

with T_{A-1} the kinetic energy of the recoiling system. The hadronic tensor, which contains all the information about the nuclear dynamics of the process including FSI, is constructed in a generic way as

$$H^{\mu\nu} = \overline{\sum_i} \sum_f J^\mu_{fi} J^{\nu\,\dagger}_{fi} = \left\langle A-1, p_N \left| \hat{J}^\mu \right| A \right\rangle \left\langle A-1, p_N \left| \hat{J}^\nu \right| A \right\rangle^*, \tag{3.4}$$

where one averages over initial and sums over final states, $|A\rangle$ is the initial nuclear state given by the target nucleus A, $|A-1, p_N\rangle$ is the final hadronic state composed of the ejected proton with asymptotic momentum p_N and the undetected final nucleus $A-1$, and $\hat{J}^\mu$ is the weak current operator. Assuming that the IA is valid, then the current operator $\hat{J}^\mu$ is reduced to an incoherent sum of relativistic one-body current operators. Additionally, we are assuming that the initial nucleus is described by the independent-particle shell model. As already explained in Sec. 2.3.2, within the IPSM the initial state is made of a finite number of nucleons characterized by the quantum numbers κ and μ, and described by a relativistic

wave function solution of the Dirac equation using the RMF potentials. Then, taking into account the IA and IPSM assumptions, the hadronic tensor is given by

$$H_{\kappa}^{\mu\nu} = \rho_{\kappa}\left(E_m\right) \sum_{\mu, s_N} J_{\kappa,\mu,s_N}^{\mu} J_{\kappa,\mu,s_N}^{\nu *} \tag{3.5}$$

with $\rho_{\kappa}\left(E_m\right)$ the missing energy density or profile of the initial nucleus, which are Dirac deltas $\delta\left(E_m - E_{\kappa}\right)$ at the values of the bound energies if one uses a pure IPSM to describe the initial state, and

$$J_{\kappa,\mu,s_N}^{\mu} = \int d\mathbf{r}\, e^{i\mathbf{r}\cdot\mathbf{q}} \overline{\Psi}^{s_N}\left(\mathbf{r}, p_N\right) \hat{J}_N^{\mu} \Phi_{\kappa}^{\mu}\left(\mathbf{r}\right) , \tag{3.6}$$

where μ is the third component of the total angular momentum $j = |\kappa| - 1/2$ of the bound nucleon, s_N the spin projection of the final nucleon and $\hat{J}_N^{\mu}$ is the CC2 one-body current operator given in Eq. (A.4). The wave functions Ψ^{s_N} and Φ_{κ}^{μ} are four-dimensional spinors which describe, respectively, the scattered and bound nucleons. Within RDWIA, the scattered proton wave function Ψ^{s_N} with asymptotic momentum p_N is obtained as a partial wave expansion

$$\Psi^{s_N}\left(\mathbf{r}, p_N\right) = 4\pi \sqrt{\frac{E_N + m_N}{2E_N}} \sum_{\kappa,\mu,m'} e^{-i\delta_{\kappa}^{*}} i^{l} < l\, m'\, \frac{1}{2}\, s_N \,|\, j\, \mu > Y_{lm}^{*}(\hat{\mathbf{r}}) \psi_{\kappa}^{\mu}\left(\mathbf{r}, p_N\right) \tag{3.7}$$

with $Y_{lm}(\hat{\mathbf{r}})$ the spherical harmonics that describe the nucleon direction and l the orbital angular momentum. The relativistic wave function $\psi_{\kappa}^{\mu}\left(\mathbf{r}, p_N\right)$ for a certain κ can be expressed as in Eq. (2.25) where the radial functions $g_{\kappa}\left(r\right)$ and $f_{\kappa}\left(r\right)$ are solutions of the Dirac coupled differential equations (see Eq. (2.27)) with some scalar and vector potentials, in addition to the Coulomb potential. However, as we will see in Sec. 3.2, the scalar and vector potentials can be complex for some FSI models, therefore the outgoing proton will be described in that case by the complex conjugates of the radial functions. Finally, the phase shifts δ_{κ}^{*} and the

normalization are calculated by matching the solutions of Eq. (2.27) with its asymptotic wave function in the limit $r \to \infty$. In the special case of the long-range Coulomb potential, the solutions are matched with the analytic expressions of the Dirac-Coulomb wave functions [77]. The bound wave functions $\Phi^{\mu}_{\kappa}(\mathbf{r})$ in Eq. (3.6) will be the complete bound-state solutions of the Dirac equation with the RMF potentials (see Eq. (2.25)).

In the next two sections, we describe more in detail the specific model of the initial state used in this thesis and the possible choices of potentials to model FSI within RDWIA.

3.1 Initial state within RDWIA: beyond the relativistic mean-field model

In Sec. 2.3.2 we briefly introduced the independent-particle shell model within the context of semi-inclusive neutrino-nucleus reactions in PWIA. There, the initial nuclear state was described only by the positive-energy bound solutions of the Dirac equation using the RMF potentials. Within the RDWIA not only the positive-energy but also negative-energy solutions using the RMF potentials are going to be used for the initial nuclear state $\Phi^{\mu}_{\kappa}(\mathbf{r})$ in Eq. (3.6). Also, it is known from exclusive $(e, e'p)$ experiments that effects beyond the mean-field approximation, such as short- and long-range correlations, modify the missing energy distribution predicted by a pure shell model like the RMF model. Hence the RMF description of the initial state will be extended to include effects beyond the mean-field approximation taking as reference the spectral function formalism (as described in Sec. 2.3.4), that simultaneously includes the depletion of the occupation of the shell-model states and the appearance of nucleons at higher missing-energies due to nucleon-nucleon correlations. However since the SF formalism assumes the factorization of the semi-inclusive cross section in to the elemental single neutrino-nucleon cross section times the spectral function, while the RDWIA formalism is an unfactorized calculation, we follow [73, 75] to include, in an effective way, the improvements of the SF formalism without imposing factorization in the

distorted-wave calculation for ^{16}O and ^{12}C. For both nuclei, the missing energy profile $\rho\left(E_m\right)$ that appears in Eq. (3.5) can be divided in different regions. In the low missing-energy region, the p-shell states (both $1p_{\frac{3}{2}}$ and $1p_{\frac{1}{2}}$ for ^{16}O and $1p_{\frac{3}{2}}$ for ^{12}C) will have a Gaussian energy dependence rather than δ-functions as in the IPSM. The same is applied to the $1s_{\frac{1}{2}}$ shell in the intermediate missing-energy region. The high E_m and p_m region of the spectral function, that accounts for correlations, will be reproduced in the RDWIA calculation by introducing an additional s wave, denominated background, that is broad in momentum space and that is fitted to reproduce the momentum distribution of the Rome spectral function [58, 68] for both nuclei. In the intermediate missing-energy region, where the s-shell and the background coexist, and in the high missing-energy zone, where only the background contributes, the background is parametrized as follows [73]:

$$F\left(E_m\right) = \frac{S_b \exp\left(-100\, b\right)}{\exp\left[-\left(E_m - c\right)/w\right] + 1} \tag{3.8}$$

if $26 < E_m < 100$ MeV, and

$$F\left(E_m\right) = S_b \exp\left(-b\, E_m\right) \tag{3.9}$$

if $E_m > 100$ MeV. The values of the parameters are obtained by performing a fit of the Rome spectral function, which yields $S_b = 0.0177\,\mathrm{MeV}^{-1}$, $b = 0.011237\,\mathrm{MeV}^{-1}$, $c = 40$ MeV and $w = 5$ MeV. Since we are more interested in the context of this thesis in ^{12}C, the specific parameterization of $\rho\left(E_m\right)$ for this nucleus is shown in Fig. 3·1. Also, the contribution of two shells of ^{12}C to the missing energy profile is summarized in Table 3.1.

In later chapters the comparison with semi-inclusive cross sections measurements and the RDWIA predictions for ^{40}Ar will be presented, however an equivalent Rome spectral function does not exist for this nucleus. Therefore for ^{40}Ar a missing energy profile $\rho\left(E_m\right)$ will be proposed [76] combining RMF results, phenomenology and exclusive $(e, e'p)$ measurements on ^{40}Ar by JLAB collaboration [78]. As for ^{12}C, the wave functions of the 22 neutrons

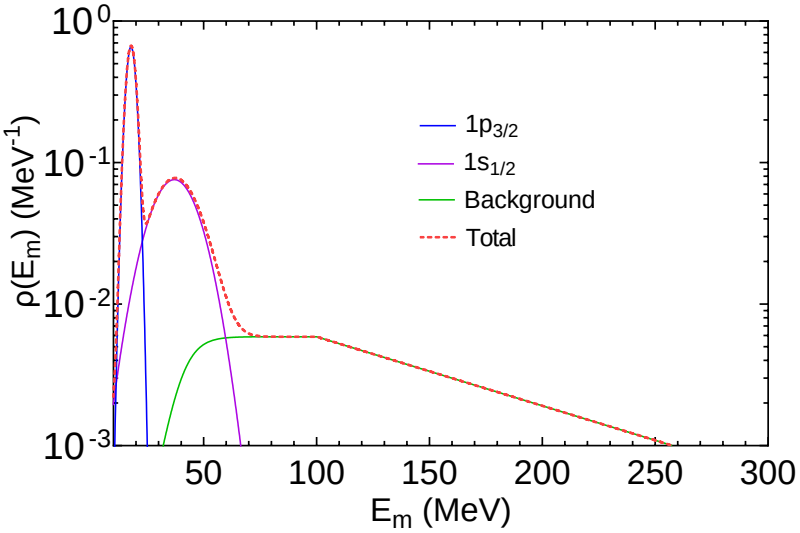

Figure 3·1: Parameterization of the missing energy profile $\rho\left(E_m\right)$ for ^{12}C separated by contributions of the individual shells and the background. The background is normalized so there are 0.8 nucleons up to $E_m = 300$ MeV, *i.e.* $\int_{26}^{300} dE_m F\left(E_m\right) = 0.8$. The remaining nucleons are associated to the shells as summarized in Table 3.1.

κ	E_κ (MeV)	σ_κ (MeV)	n_κ
$1s_{1/2}$	37.0	10.0	1.9
$1p_{3/2}$	17.8	2.0	3.3

Table 3.1: Parameterization of the missing energy distributions for the two shells of ^{12}C. The contribution to the missing energy density $\rho_\kappa\left(E_m\right)$ of each shell is given by $\rho_\kappa\left(E_m\right) = \frac{n_\kappa}{\sqrt{2\pi}\sigma_\kappa} \exp(-\left(\frac{E_m - E_\kappa}{2\sigma_\kappa}\right)^2)$, with E_κ position of the peak, σ_κ the width and n_κ the occupation number, *i.e.* the number of nucleons in each shell.

in ^{40}Ar will be given by the bound states solutions of the Dirac equation with the RMF potentials. However the realistic missing energy profile $\rho\left(E_m\right)$ for ^{40}Ar will be modeled as a Maxwell-Boltzmann distribution [78] for each shell κ

$$\rho_\kappa\left(E_m\right) = \frac{4S_\kappa}{\sqrt{\pi}\sigma_\kappa}\left(\frac{E_m - E_\kappa + \sigma_\kappa}{\sigma_\kappa}\right)^2 \exp\left[-\left(\frac{E_m - E_\kappa - \sigma_\kappa}{\sigma_\kappa}\right)^2\right]\left(2j_\kappa + 1\right), \tag{3.10}$$

with E_κ the position of the peak, σ_κ the width, S_κ the occupancy of the shell, *i.e.* the ratio

between the number of nucleons in a shell and the number of nucleons predicted by the IPSM, and j_κ the total angular momentum of the shell κ. A summary with the parameterization for the seven shells in ^{40}Ar can be found in Table 3.2. There, the position of the peaks are given by the RMF predictions except for the valence shell ($1f\frac{7}{2}$) which is fixed to the experimental neutron separation energy [79]. The widths of the shells used in this thesis to describe neutrons in argon are inspired from $(e, e'p)$ exclusive measurements in ^{40}Ar by JLAB [78]. Finally, the spectroscopic factors assigned to each shell are based on phenomenology: the internal shells ($1s\frac{1}{2}$, $1p\frac{3}{2}$ and $1p\frac{1}{2}$) are affected by short-range correlations while external shells ($1d\frac{5}{2}$, $2s\frac{1}{2}$, $1d\frac{3}{2}$ and $1f\frac{7}{2}$) do depend on both short- and long-range correlations [80, 81], therefore their spectroscopic factors are lower. In addition to the value of the parameters, Table 3.2 also shows the uncertainty associated to each parameter. Proceeding in this way we provide, for the first time, an uncertainty band in theoretical semi-inclusive neutrino-nucleus predictions due to the modeling of the initial nuclear state. This uncertainty band will be generated by randomly sampling the values of the missing energy profile parameters within their uncertainties with an uniform probability distribution and running the RDWIA calculation for up to one hundred different combinations of the $\rho\,(E_m)$ parameterization. The only parameter missing for this model of neutrons in ^{40}Ar is the background normalization S_b in Eqs. (3.8) and (3.9). This parameter, related with the number of neutrons in the background, is constrained by imposing that the total number of neutrons is fixed to 22 for each different parameterization of $\rho\,(E_m)$. However, using this method, some random combinations of the parameters could give up to 40-50% of the neutrons in background for argon which is clearly unrealistic. To avoid this, the RDWIA calculation is done only if the background contains between 15-25% of the 22 neutrons, which is consistent with previous studies [82, 83, 84]. The corresponding missing energy profile $\rho\,(E_m)$ for argon is shown in Fig. 3·2 compared with the RMF prediction.

α	E_κ (MeV)	σ_κ (MeV)	S_κ
$1s_{1/2}$	55 ± 6	30 ± 15	0.9 ± 0.15
$1p_{3/2}$	39 ± 4	12 ± 6	0.9 ± 0.15
$1p_{1/2}$	34 ± 3	12 ± 6	0.9 ± 0.15
$1d_{5/2}$	23 ± 2	5 ± 3	0.75 ± 0.15
$2s_{1/2}$	16.1 ± 1.6	5 ± 3	0.75 ± 0.15
$1d_{3/2}$	16.0 ± 1.6	5 ± 3	0.75 ± 0.15
$1f_{7/2}$	9.869 ± 0.005	5 ± 3	0.75 ± 0.15

Table 3.2: Parameterization of the missing energy distribution for the 22 neutrons in ^{40}Ar adopted in this work. The missing energy distributions are modeled as Maxwell-Boltzmann distributions (see the text). The spectroscopic factors or occupancies of the shells S_κ give the relative occupancy of the shell respect to the pure shell model prediction. The position of the $1f_{\frac{7}{2}}$ shell was set to the experimental neutron separation energy [79], and the others were set to the RMF values. The widths used in this model were inspired from the proton results obtained by JLAB $(e, e'p)$ experimental data on ^{40}Ar [78].

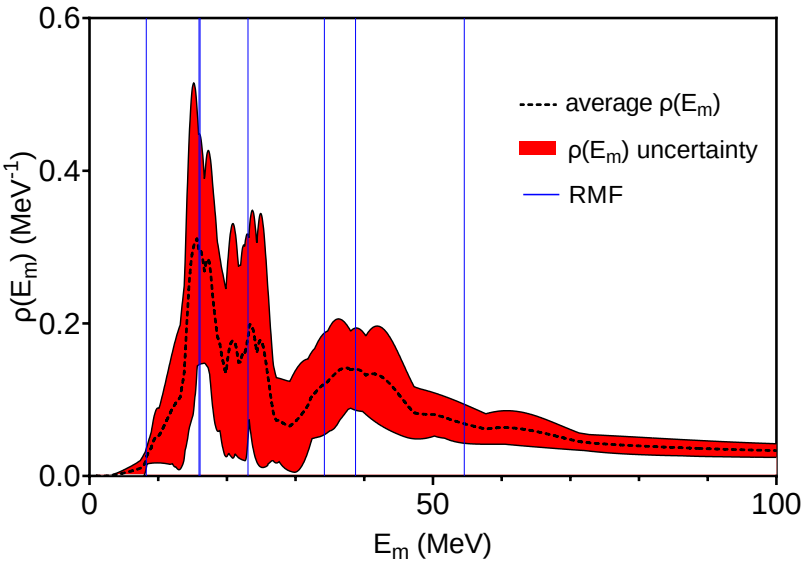

Figure 3·2: Missing energy profile of neutrons in ^{40}Ar described by the parameterization given in Table 3.2. The red band corresponds to the uncertainties also summarized in Table 3.2. The vertical blue lines show the positions of the seven RMF shells and the black dashed line shows the mean value of the distribution.

3.2 Final state interactions within RDWIA

In this section two approaches to FSI within RDWIA, denoted as Relativistic optical potential (ROP) and Energy-dependent relativistic mean field (ED-RMF), are discussed. In general, FSI models can either use complex potentials or only real potentials. Complex potentials, given that the imaginary part of the potential produces a loss of flux to inelastic channels, should be used when the kinematic constrains of the experiment being analyzed isolates the elastic channel, for instance exclusive $(e, e'p)$ experiments. This is equivalent to constrain the values of the missing energy E_m below the two nucleons knockout energy, which guarantees that only the elastic channel is being measured. Instead, pure real potentials are more appropriate for inclusive-like measurements where all the channels contribute to the experimental signal, including the inelastic ones.

3.2.1 Relativistic optical potential

The ejected nucleon wave function is calculated as the scattering solution of the Dirac equation in the presence of a complex relativistic optical potential. In this thesis, we use phenomenological relativistic optical potentials that are not derived from a specific microscopic theory but have been fitted to certain elastic proton-nucleus scattering observables. Specifically, we will use global scalar-vector (S—V) potentials that can be applied to protons with different kinetic energies. Cooper *et at* [85] published different parametrizations for nuclei of interest for accelerator neutrino experiments, such as ^{12}C, ^{16}O or ^{40}Ca, for protons kinetic energies in the range $20 \leq T_N \leq 1040$ MeV. Although ^{40}Ca is not used as target in accelerator neutrino experiments, its parametrized relativistic optical potential will be employed to generate the predictions for ^{40}Ar in later chapters. The scalar or vector global

S—V relativistic optical potentials take the general form [85]

$$U(r,E,A) = V^{\mathcal{V}}(E,A)\, f^{\mathcal{V}}(r,E,A) + V^{\mathcal{S}}(E,A)\, f^{\mathcal{S}}(r,E,A) + i\Big(W^{\mathcal{V}}(E,A)\, g^{\mathcal{V}}(r,E,A) + W^{\mathcal{S}}(E,A)\, g^{\mathcal{S}}(r,E,A) \Big), \tag{3.11}$$

where E and r are the proton center of mass energy and position, A is the atomic mass number of the target and the superscripts $\mathcal{V}$ and $\mathcal{S}$ refer to the volume and surface peaked terms respectively. The geometric functions f^i and g^i, with $i = \mathcal{V}, \mathcal{S}$, are

$$f^{\mathcal{V}}(r,E,A) = \frac{\cosh\left[R(E,A)/a(E,A)\right] - 1}{\cosh\left[R(E,A)/a(E,A)\right] + \cosh\left[r/a(E,A)\right] - 2},$$

$$f^{\mathcal{S}}(r,E,A) = \frac{\Big(\cosh\left[R(E,A)/a(E,A)\right] - 1\Big)\Big(\cosh\left[r/a(E,A)\right] - 1\Big)}{\Big(\cosh\left[R(E,A)/a(E,A)\right] + \cosh\left[r/a(E,A)\right] - 2\Big)^2}. \tag{3.12}$$

The same functional forms are used for g^i. As mentioned above, the optical potential consists of scalar and vector terms each having both real and imaginary parts. In the parametrization the eight strength parameters, namely V^i and W^i for the scalar and vector terms, have the same polynomial dependence upon E and A. For instance

$$V^{\mathcal{V}}(E,A) = v_0 + \sum_{m=1}^{4} v_m x^m + \sum_{n=1}^{3} v_{n+4} y^n + v_8 xy + v_9 x^2 y + v_{10} x y^2, \tag{3.13}$$

where $x = 1000/E$, with E in MeV, and $y = A/(A+20)$. Generally, both scalar and vector potentials, as well as their real and imaginary parts, may have different geometry parameter values. The functions $R(E,A)$ and $a(E,A)$ appearing in Eq. (3.12) are also represented by

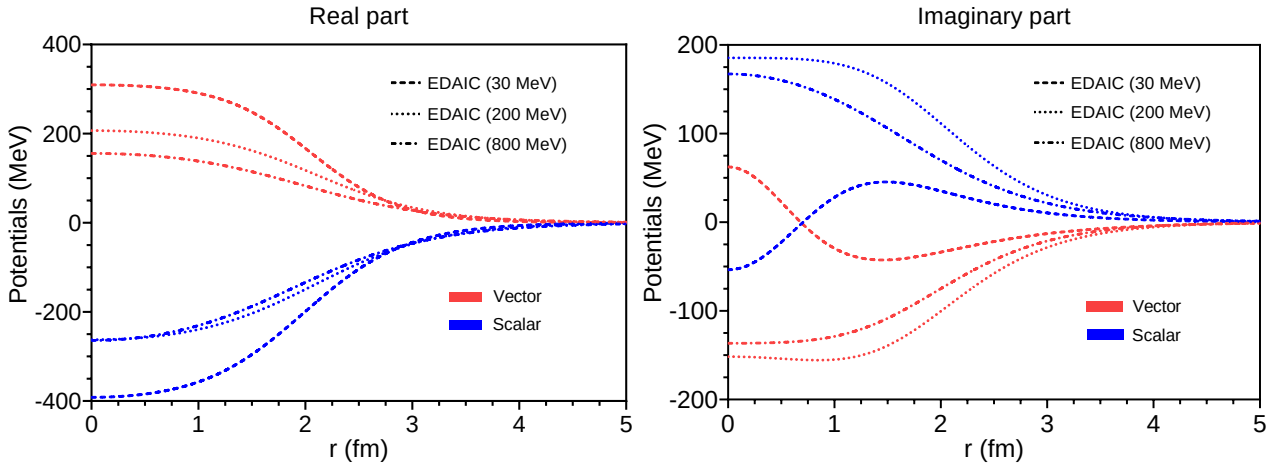

Figure 3·3: Energy-dependent A-independent ^{12}C (EDAIC) relativistic optical potential [85] evaluated at different proton kinetic energies $T_N = 30$ MeV (dashed), 200 MeV (dotted) and 800 MeV (dash-dotted). The vector (red lines) and scalar (blue lines) components of the potential are shown separately for both the real (left panel) and imaginary (right panel) parts.

polynomial expansions, as follows

$$R\left(E,A\right)=A^{1/3}\left[r_0+\sum_{m=1}^{4}r_m x^m+\sum_{n=1}^{3}r_{n+4}y^n+r_8xy+r_9x^2y+r_{10}xy^2\right], \tag{3.14}$$

$$a\left(E,A\right)=a_0+\sum_{m=1}^{4}a_m x^m+\sum_{n=1}^{3}a_{n+4}y^n+a_8xy+a_9x^2y+a_{10}xy^2. \tag{3.15}$$

The optical potentials that will be used in this thesis are the ones denominated energy-dependent A-independent (EDAI) potentials where the dependence on A of all the parameters is dropped. Further simplifications are performed, compared with the general energy-dependent A-dependent (EDAD) potentials, to reduce the total number of parameters for each target nucleus to 70 [85]. The number of data points used in the fits for each target is well over 1000. Fig. 3·3 shows the radial dependence of the EDAIC potential (the one for ^{12}C) evaluated at different proton kinetic energies.

As it was said previously, the ROP contains a real and an imaginary term, where the

latter accounts for losses to inelastic channels. Thus, the ROP describes scenarios where the ejected nucleon propagates through the residual nucleus undergoing only elastic scattering and consequently no other hadrons are created in the process. Hence, the ROP describes the QE contribution to the situation where only one proton and no other hadrons are detected in the final state, although additional hadrons can appear due to MEC or to initial state correlations, if the missing energy is large enough. The ROP approach was successfully applied in the past to describe exclusive electron scattering $(e, e'p)$ [70, 71, 72] experiments, for which a missing energy below the two-nucleon knock-out threshold can be determined from the detection of the final electron and proton in coincidence, plus the knowledge of the energy of the initial electron. In case of neutrino scattering, however, due to the fact that the energy distribution of the neutrino beams is very wide, the mere detection in coincidence of a muon and a proton in the final state does not guarantee control of the missing energy. Thus, the measured events would be composed of contributions beyond the elastic one described by the ROP. A simple way to consider in the final state the events beyond the elastic channel is to take only the real part of the ROP (rROP), that is, removing the absorption into the elastic-only channel. This has been shown to be quite effective in describing inclusive cross-section measurements [86, 87] which include all hadronic final states, namely both elastic and inelastic channels. The rROP model does not include losses to inelastic channels and is, in principle, consistent with special relativity and quantum mechanics. However there could be orthogonality issues [86, 88, 89] for small momenta transfer because the initial and final states are described by solutions of different Hamiltonians (RMF for the initial nuclear state, rROP for the final nuclear state). This problem is overcome in the ED-RMF approach described below.

3.2.2 Extended relativistic mean-field potential: ED-RMF

As explained in Sec 3.1 the wave function used to describe the initial nuclear state that interacts with the neutrino corresponds to the eigenstates solution of the Dirac equation using the RMF potentials (see Appendix C where the RMF model is described in more details). The same RMF potentials can be used to solve the Dirac equation and find the scattering states that describe the ejected nucleon wave function. By adopting this approach, the preservation of orthogonality is guaranteed and the distortion of the outgoing nucleon (FSI) is considered by propagating it using the self-energy calculated within the mean-field approach. This methodology proves to be a suitable approximation in scenarios where nucleon propagation can be adequately described by this model, particularly, in inclusive electron [90, 91] and neutrino [91, 92] reactions involving moderate values of transferred momentum. Although Pauli blocking is automatically obtained by using the same potential for both the initial and final nuclear states, there are some disadvantages of using this approach for certain reactions and kinematics. For instance, in exclusive experiments, like $(e, e'p)$, where the value of E_m is selected to isolate the elastic channel, a potential with only real components, like the RMF, would not describe them correctly. Instead an optical potential with an imaginary part, like the one described in Sec. 3.2.1, should be employed [70, 72]. Also, using a pure RMF approach, with an energy-independent potential to describe the nucleon in the final state, is bound to be inadequate as the momentum of the final nucleon increases, even in the case of inclusive experiments [91, 93]. The RMF potentials are too strong for relatively high nucleon momenta, a region where one expects the potentials to become weaker. A solution to this problem was presented with the SuSAv2 model [91], which incorporates a combination of results from both the RMF and RPWIA approaches. It employs a linear combination of the scaling functions derived from RPWIA and RMF, with the weight of each contribution determined by a transition function that varies with the momentum transfer q. In [94] the parameters of the SuSAv2

model were fitted to $^{12}\mathrm{C}(e,e')$ data, resulting in remarkable agreement with inclusive data, particularly for ω values exceeding approximately 50 MeV. This agreement extends to (e,e') data from different nuclei [93] as well as to inclusive CC neutrino-nucleus reactions [95]. Exploiting the success of the SuSAv2 model, an energy-dependent relativistic mean field potential (ED-RMF) [86, 87] can be constructed that keeps the RMF strength and proper orthogonality for slow nucleons, but becomes weaker as nucleon momenta increase following SuSAv2 phenomenological transition function. The ED-RMF blending function $f_b\left(T_N\right)$, that depends on the outgoing nucleon kinetic energy T_N and multiplies both the vector and scalar RMF potentials, was fitted to the SuSAv2 RMF-to-RPWIA transition function for $^{12}\mathrm{C}$, and is the following [87]

$$f_b\left(T_N\right) = \frac{0.85}{\left(T_N/200\right)^2 + 3.5} + \frac{0.48}{\exp\left[\left(T_N - 90\right)/23\right] + 1} + 0.29, \tag{3.16}$$

where T_N is in the laboratory frame and in MeV. The radial dependence of both ED-RMF and RMF potentials for $^{12}\mathrm{C}$ are compared in Fig. 3·4 for different values of T_N. For small values of T_N both potentials are essentially the same, preserving orthogonality that is especially relevant in this low-momentum region. At larger values of T_N, orthogonality is no longer an issue and the blending function $f_b\left(T_N\right)$ reduces the magnitude of the strong RMF potentials improving the agreement with inclusive electron and neutrino scattering data. Although the blending function $f_b\left(T_N\right)$ has been fitted to electron scattering data by $^{12}\mathrm{C}$, the same parametrization has been successfully used to describe inclusive electron data on argon and titanium [86, 87].

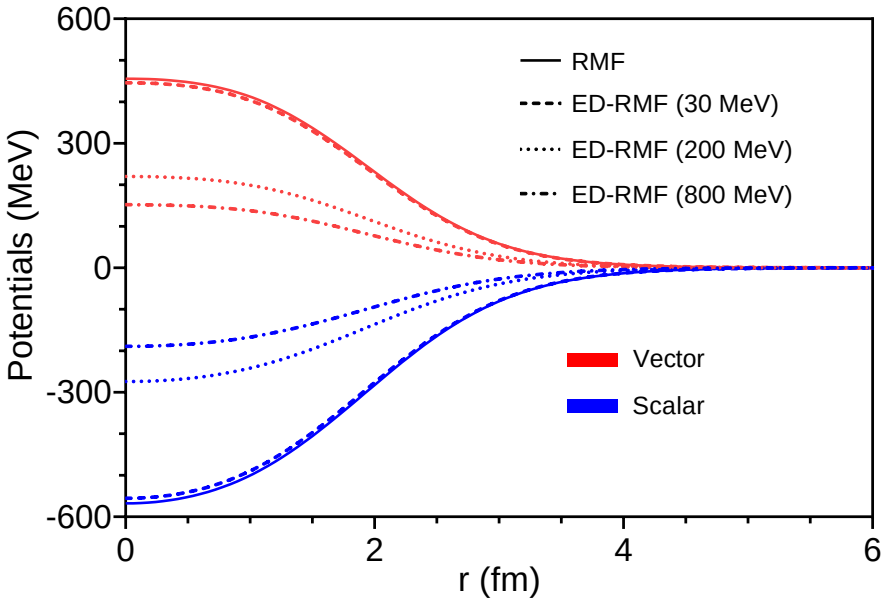

Figure 3·4: Energy-dependent relativistic mean field (ED-RMF) potential [86, 87] for ^{12}C evaluated at different proton kinetic energies $T_N = 30$ MeV (dashed), 200 MeV (dotted) and 800 MeV (dash-dotted). The RMF potential (solid) is also shown for reference. The vector (red lines) and scalar (blue lines) components of the potentials are shown separately.

Chapter 4

Neutrino generators approach to semi-inclusive reactions

In the previous chapter we have introduced the relativistic distorted-wave approach from which an expression of the five-dimensional differential cross section can be obtained without any further approach than the IA (see Eq. (3.1)). The RDWIA is one of the few microscopic models capable of reliably provide both exclusive-like and inclusive (by integrating over all the ejected nucleon variables) cross sections without relying on the factorized expression obtained in the PWIA limit. The analysis of neutrino oscillation measurements requires the usage of neutrino event generators, based on Monte Carlo simulations, to reconstruct the unknown initial neutrino energy on an event-by-event basis by correctly modeling all the possible reactions channels (QE, 2p2h, inelastic, coherent, etc), and also different nuclear effects like initial state correlations, Fermi motion or FSI. The most common MC generators used in accelerator-based and scattering neutrino experiments are GENIE [96, 97, 98], NEUT [99, 100, 101], GiBUU [102] and NuWro [103]. Without entering into much detail, a generic neutrino event generator typically proceeds through the following steps:

(I) The incident neutrino energy is determined from the neutrino energy distribution.

(II) The target nucleus is selected according to the cross section of the target material.

(III) The location of the target nucleon inside the nucleus is randomly chosen. The initial four-momentum of the nucleon is taken from the momentum distribution given by the

nuclear model implemented in the generator.

(IV) The interaction mode is selected from the probabilities for the corresponding incident neutrino energy. For instance, if a large neutrino energy was initially sampled, it is more probable that the selected mode is inelastic scattering rather than QE.

(V) The neutrino-nucleon interaction is simulated according to the interaction mode selected and the differential cross section of the interaction is used to simulate the kinematics of the outgoing lepton, nucleon(s) and other particles (for instance, pions).

(VI) The possible re-interactions of the particles within the nucleus are simulated, according to the FSI model.

The semi-classical intranuclear cascade model (INC) is the most commonly used FSI model in neutrino generators. It considers each particle produced individually, starting from the interaction vertex and continuing until the particle exits the nucleus. During this propagation, the particle is moved in small steps (around 0.1 fm, typically), and at each step, the probability of an interaction is evaluated. This probability is based on the particle's mean free path, which is influenced by the density of the surrounding medium (determined according to the nuclear model) and the probability of interacting with nucleons. Various types of interactions with the nucleus are possible, and their individual cross sections depend on the particles' energies. The only quantum effect considered is Pauli blocking. Apart from that, the model is classical in nature, treating the propagated particles as free and assuming they travel in straight lines between consecutive scatterings. The scatterings themselves are evaluated using free-space cross sections. Pauli blocking can be included as an average effect by reducing the nucleon interaction cross section through a global factor or as a local effect by ensuring that the momentum of the final-state particles is above some value of the Fermi momentum at each interaction point.

The implementation of a specific neutrino interaction model in a neutrino event generator

usually requires a fast method of calculating the differential cross section. However the RDWIA calculations demand significant computational resources to generate predictions for comparison with experimental measurements, although the computation can be accelerated by, for instance, precalculating and storing in tables the hadronic tensor components $H_{\kappa}^{\mu\nu}$ as function of four dynamic variables (for instance q, ω, p_m and E_m). Until this date few microscopic models capable of exclusive predictions are implemented in neutrino event generators. Some work is currently being done to implement models based in RDWIA approach in MC generators [74]. Models like SuSAv2 [91, 93, 94] and Hartree-Fock continuum random phase approximation (HF-CRPA) [104, 105] have been implemented in some neutrino event generators like GENIE, but these models yield inclusive predictions as function of the outgoing lepton kinematics only. Later on, we will elaborate on the implementation of these models [106, 107] in generators using a factorization ansatz [106]. In this approach, lepton kinematics is directly computed from a microscopic model calculation before the hadronic system is incorporated using approximate methods. As a result, the model accurately reflects the microscopic model's predictions for lepton kinematics, but it provides only a broad estimation for outgoing hadron kinematics due to the limited information available.

Summarizing, models that are in principle inclusive can be used in combination with neutrino event generators to provide semi-inclusive predictions by means of different approximations. Exploiting this approach, in this thesis we will compute the semi-inclusive predictions using the SuSAv2 implementation in GENIE [106] and directly compare them with the RDWIA results and experimental semi-inclusive measurements by different international collaborations. Since all the available semi-inclusive experimental data correspond to CC0π, we will also make use of the SuSAv2 2p2h model implemented in GENIE as well as the GENIE's pion absorption model to generate the non-quasielastic (non-QE) contributions to semi-inclusive cross sections. In what follows, we discuss in detail the implementation approach of the SuSAv2 (QE and MEC) model in GENIE. Additionally, a brief description of GENIE's

pion absorption model is also presented before we move on to the comparison with the experimental data in the next chapter.

4.1 SuSAv2 implementation in GENIE

At present, only a few neutrino event generators are capable of calculating exclusive predictions. Most theoretical models implemented in the generators can predict the kinematics of the outgoing leptons but are not directly applicable to describe hadrons in the final state. Nevertheless, it is feasible to generate semi-inclusive predictions, involving both a lepton and a hadron in the final state, by employing inclusive models implemented in generators with the aid of approximations like the factorization approach [106]. However, given the impact of these semi-inclusive reactions on oscillation analyses, it is necessary to validate the accuracy of these approximations against experimental measurements of cross sections and also against microscopic neutrino interaction models capable of predicting final lepton and hadron kinematics.

Among the different nuclear models for neutrino interactions, those based on the RMF theory are promising candidates to be implemented in event generators due to their accurate description of the nuclear dynamics and their good agreement with both inclusive and semi-inclusive electron- and neutrino-nucleus scattering data without relying on any factorization approach. As a first attempt in this direction, the SuSAv2-MEC model [91, 93, 94], a purely inclusive approach based on the RMF theory which has proven to successfully predict inclusive cross sections for electrons and neutrinos in a wide range of kinematics, was implemented in the neutrino event generator GENIE [106] for both 1p1h and 2p2h channels. This implementation has been carried out via SuSAv2 1p1h and 2p2h inclusive hadron tensor tables, $H_{\mu\nu}(q,\omega)$, using a binning of 5 MeV in the transferred momentum and energy which is combined with GENIE's interpolation methods between adjacent bins. Since the SuSAv2 is an inclusive model and all the information about hadrons in the final state has been

integrated, a factorization between the leptonic and hadronic vertices is used to generate semi-inclusive predictions. Under this approach the outgoing hadronic state is generated starting with an initial nucleon state sampled from a local Fermi gas (LFG) nuclear model for the 1p1h channel. A missing momentum $\mathbf{p_m}$ is sampled from the LFG momentum distribution and the outgoing nucleon energy E_N is calculated as [108]

$$E_N = \sqrt{p_m^2 + m_N^2} - \omega - E_b\left(q\right), \tag{4.1}$$

where $E_b\left(q\right)$ is a q-dependent binding energy inspired by the phenomenological energy shift from the SuSAv2 model

$$E_b = \max\left(5, -17.687 + 0.0564q\right)\left[\text{MeV}\right]\left(q < 827\text{MeV}\right) \tag{4.2}$$

and $E_b\left(q\right) = E_b\left(q = 827\text{ MeV}\right) \simeq 29$ MeV for $q > 827$ MeV. The outgoing nucleon momentum calculated according to Eq. (4.1) will not agree in general with momentum conservation Eq. (2.1), *i.e.* $\sqrt{E_N^2 - m_N^2} \neq |\mathbf{p_m} + \mathbf{q}|$. To partially solve this issue, the magnitude of the outgoing nucleon momentum is taken from Eq. (4.1) but the direction is constructed according to the momentum conservation, *i.e.*

$$\mathbf{p_N} = \sqrt{E_N^2 - m_N^2}\left(\frac{\mathbf{p_m} + \mathbf{q}}{|\mathbf{p_m} + \mathbf{q}|}\right). \tag{4.3}$$

After the nucleon is extracted, the propagation is carried out through the nucleus using GENIE's semi-classical cascade FSI model. In [108] the distributions as function of the nucleon kinetic energy and scattering angle were obtained for exclusive $(e, e'p)$ events on carbon using the ED-RMF model and GENIE's factorization approach described above. The distributions are shown in Fig. 4·1 where a shift in the nucleon kinetic energy distribution is observed between the exact calculation ("Full") and the GENIE implementation ("Approx").

Regarding the angular distribution, the differences found are larger than for the energy distribution with a slight displacement of the maximum and significant shape differences. As pointed out in [108] these differences could be washed out after applying the GENIE cascade FSI model, however it was found that the effects of the factorization approach remain visible. In the case of the SuSAv2 2p2h channel, based on the relativistic Fermi

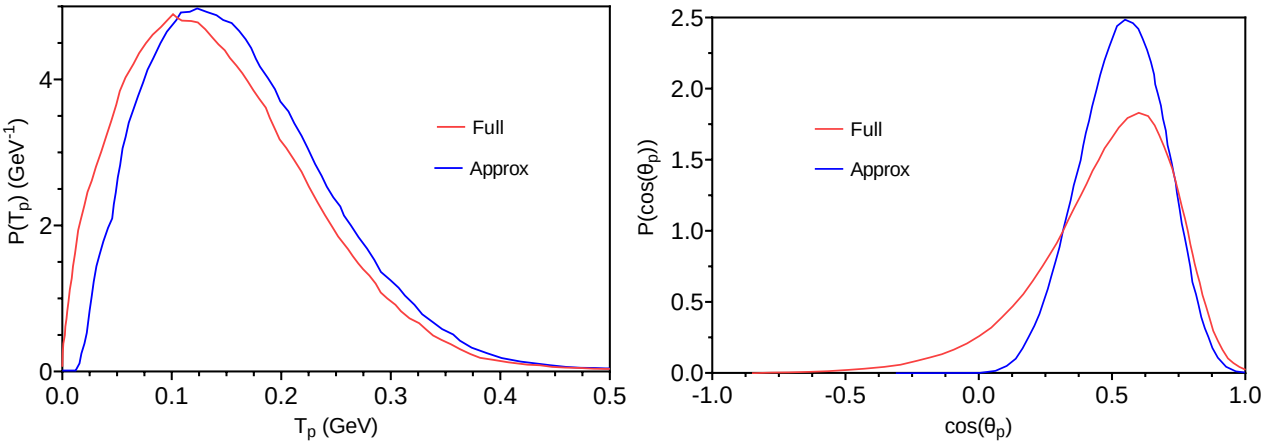

Figure 4·1: Proton kinetic energy (left) and scattering angle (right) distributions for the process $e+A \rightarrow e'+p+B$. The electron beam energy is fixed to 1.159 GeV and the outgoing electron phase-space is limited to $17^\circ < \theta_{e'} < 40^\circ$ and $E_{e'} > 0.4$ GeV. The red lines show the unfactorized RDWIA predictions obtained with ED-RMF potential for carbon (named "Full") while the blue lines show the equivalent distributions obtained after applying the GENIE algorithm (Eq. (4.1) and Eq. (4.3)) and before adding GENIE cascade FSI (named "Approx"). Results taken from [108].

gas (RFG) calculation [109, 110], the momentum and energy transfer are assigned to a pair of nucleons drawn from a LFG nuclear model after taking into account the removal energy, which is a constant in this case. The probability of having neutron-neutron (proton-proton for antineutrinos) or proton-neutron pairs as initial cluster is chosen based on the kinematics of the inclusive reaction using the SuSAv2-MEC 2p2h theoretical model [111]. The transferred momentum and energy are shared equally between the cluster components, one neutron (proton) is turned into a proton (neutron) for neutrinos (antineutrinos) and the cluster breaks up into two nucleons. The two nucleons are then propagated through the

nucleus via GENIE's semi-classical cascade model.

4.2 GENIE pion absorption model

GENIE can further be used to model the pion absorption contribution to semi-inclusive CC0π measurements. The predominant contribution stems from GENIE's simulation of single pion production using an extension of the Rein-Sehgal model [112] to account for nonzero lepton masses [113], which produces pions and nucleons which are propagated through the nucleus via the same semi-classical cascade FSI model used for other interaction channels. In a portion of the events, the outgoing pions are absorbed within the nuclear medium, often leading to the ejection of additional nucleons in the process. The small additional contributions, where all mesons are absorbed by FSI, arise from more inelastic channels. These channels are evaluated using an effective leading-order model that incorporates the modifications proposed by Bodek and Yang [114] to accurately describe scattering at low momentum-transfers.

Chapter 5

Comparison with semi-inclusive experimental measurements

In this chapter all the available CC semi-inclusive neutrino-nucleus experimental measurements from T2K [115], MINERνA [116, 117] and MicroBooNE [118, 119] are compared with the theoretical RDWIA QE predictions using different FSI models described in Chapter 3: ROP, rROP, ED-RMF and RPWIA. These unfactorized predictions will be compared to those obtained by the SuSAv2 model implemented in GENIE neutrino event generator as explained in Sec. 4.1. For a fair comparison with the experimental measurements, which are all CC0π, the SuSAv2-2p2h MEC and pion absorption contributions calculated with GENIE will be added to the QE predictions.

5.1 T2K

The T2K collaboration measured [115] $\nu_\mu - ^{12}$C CC0π semi-inclusive cross sections with two different topologies: *i*) one muon and no protons in the final state (1μCC0π0p) with momenta above 0.5 GeV, and *ii*) one muon and at least one proton in the final state (1μCC0πNp) where the leading (*i.e.* the fastest) proton has momentum above 0.5 GeV.

5.1.1 1μCC0π0p

By the definition of this topology one could think that this corresponds to the inclusive CC0π channel, where only the final lepton is detected while no information about hadrons in the final state does exist. However, in the definition of the inclusive cross section one explicitly integrates over the ejected hadron variables in the entire phase-space allowed by conservation and the kinematics of the reaction. For the 1μCC0π0p signal, the integration over the ejected proton kinematics is performed as in the inclusive case except for the integral over p_N which is limited by the T2K experimental proton detection threshold of 0.5 GeV. Because of this limitation in the proton momentum, no inclusive model can be compared with these data because it would necessarily include contributions of protons with momenta above 0.5 GeV. Therefore these cross sections are indeed semi-inclusive and only models capable of predicting both the final muon and proton kinematics, like the RDWIA, can be compared against them.

In Fig. 5·1 the microscopic RDWIA and the GENIE-SuSAv2 predictions are compared with T2K 1μCC0π0p measurements as function of the muon kinematics. For backward angles the microscopic calculation predicts a rather small difference between RPWIA and the models with FSI (rROP, ROP and ED-RMF), all of them underestimating the experimental measurements in contrast with the better agreement achieved with GENIE-SuSAv2. As one moves to more forward muon angles GENIE-SuSAv2 predictions start to overestimate some of the experimental points, an outcome probably due to scaling or factorization violations and poor treatment of low-energy effects which are accounted for more consistently by the ED-RMF model. The two RDWIA models that use real potentials, namely ED-RMF and rROP, give similar predictions for backward muon angles. However, some differences appear as one moves to more forward muon angles and the maximum discrepancy can be observed in the peak of the $0.98 < \cos\theta_l < 1.0$ distribution. In this zone, where q and ω are small, the ED-RMF prediction is closer to the data due to the better treatment of orthogonalization

between the initial and final nucleon wave functions. All the RDWIA models except the ED-RMF have at some degree lack of orthogonalization in this region, but in particular the overlap between the initial bound wave functions and the plane waves used in RPWIA is very large yielding big spurious contributions to the cross section for this model which largely overestimates the data at low values of k'. For all the angular bins the 2p2h contribution, although non-negligible, is limited to a few percent of the total cross section. Interestingly, the final state proton kinematic restriction ($p_N < 0.5$ GeV) leaves the pion absorption contribution negligible. No model is able to reproduce the sharp oscillation shown by the data just after the maximum in the last two bins ($0.94 < \cos\theta_l < 0.98$ and $0.98 < \cos\theta_l < 1.0$), but it should be noted that, once the reported correlations in the measured cross section are accounted for, the measurement shows no significant preference for an oscillation in the cross section.

To quantify the agreement of the different models with the data, in Appendix D a χ^2 analysis using the covariance matrices provided with the cross sections measurements is discussed in detail. All the results for T2K are summarized in Table D.1. For CC0π measurements without protons in the final state and momenta above 0.5 GeV, the ROP and ED-RMF models have associated a smaller χ^2 compared with GENIE-SuSAv2 results, although still much larger than the number of degrees of freedom (*d.o.f.*), indicating that low momentum protons are not quantitatively described by these models.

5.1.2 1μCC0πNp: Muon and proton kinematics

In Fig. 5·2 and Fig. 5·3 the different models are compared with T2K 1μCC0πNp semi-inclusive cross-section measurements with at least one proton with momentum above 0.5 GeV as function of the leading proton's kinematics and the muon scattering angle, respectively. In general, the 2p2h channel seems to be more relevant for this case compared with the previous analysis, especially at forward scattering angles. This is not surprising, since the

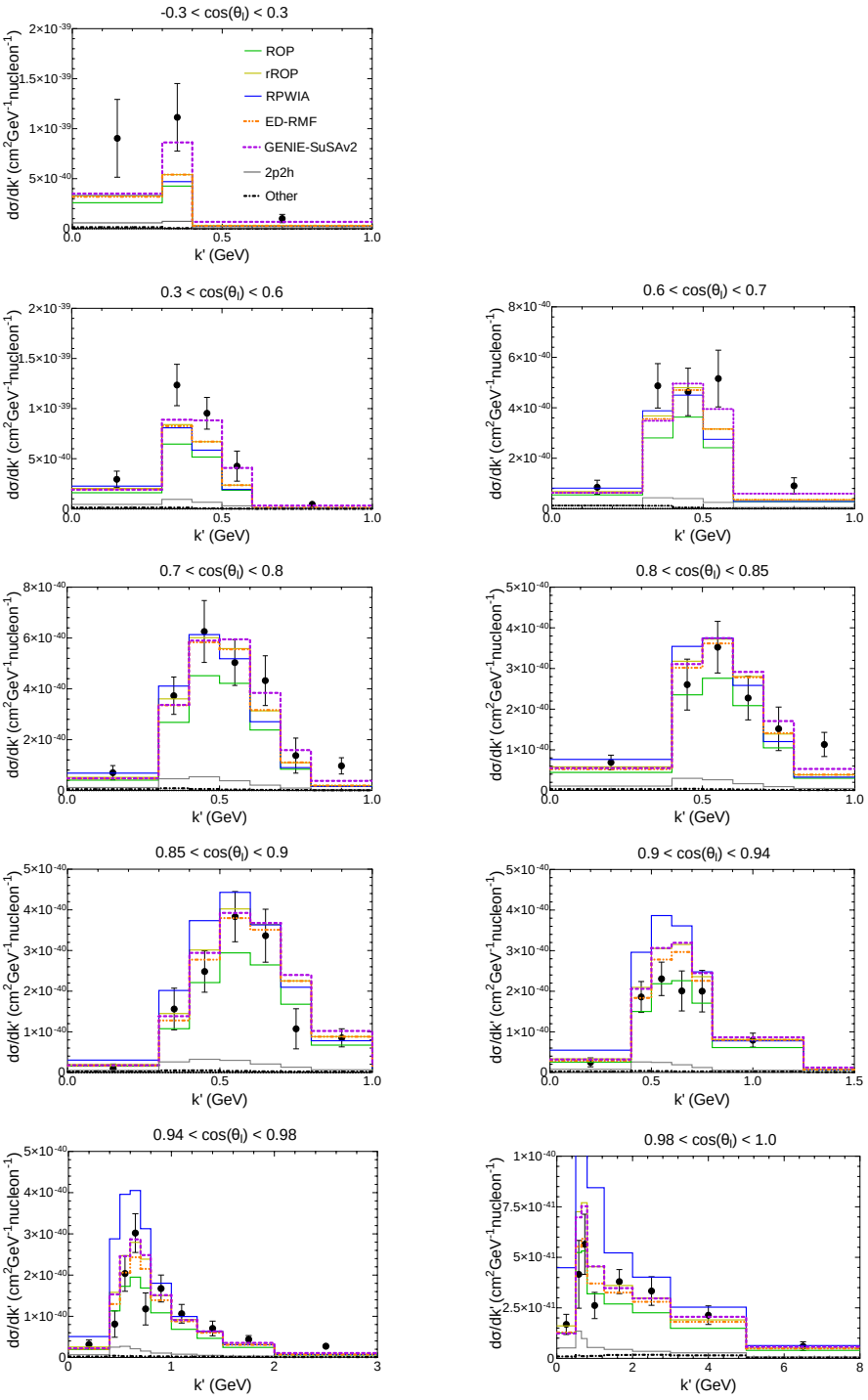

Figure 5·1: T2K 1μCC0π0p semi-inclusive $\nu_\mu - {}^{12}$C cross section without protons in the final state with momenta above 0.5 GeV as function of the muon kinematics. All curves include the 2p2h and pion absorption (denoted "other") contributions evaluated using GENIE (shown separately). Cross-section measurements taken from [115].

2p2h cross section is peaked at higher ω (hence higher p_N) than the QE cross section. The pion absorption channel also appears more relevant, but only in specific regions of outgoing muon and proton kinematics (at relatively forward muon and proton scattering angles). As a consequence non-QE contributions do affect more to data corresponding to values $p_N > 0.5$ GeV than at $p_N < 0.5$ GeV. In the specific case of the distribution as function of $\cos\theta_N^L$ with $0.8 < \cos\theta_l < 1.0$, the bin $0.8 < \cos\theta_N^L < 1.0$ is overestimated by all the RDWIA models and GENIE-SuSAv2 due to the large non-QE (2p2h + pion absorption) contributions.

The GENIE-SuSAv2 results slightly overestimate some of the experimental points, while the ED-RMF and rROP models tend to match or improve the agreement, especially for proton momentum around 0.5-0.7 GeV. It is interesting to note that the ROP model in Fig. 5·3 describes better the cross section measurements for $0.3 < \cos\theta_l < 1.0$ than the rest of the models, but the situation reverses for $-1.0 < \cos\theta_l < 0.3$, with ROP underestimating the cross section measurements. ROP predicts the cross section corresponding to the case in which the struck nucleon interacts only elastically with the residual nucleus, i.e., it does not knock out other nucleons or create new mesons in its way out. Thus, if one does not include the background contribution due to short-range correlations, that appears at large E_m-p_m (see Fig. 3·1), and that necessarily corresponds to a process with at least two nucleons in the final state, then the ROP model gives a lower bound estimate of the cross section for one and only one proton, and no other hadron, in the final state. One does expect in general that the experimental neutrino measurements are above the ROP predictions, consistently with the fact that the experimental signal includes more channels than the one represented in the ROP, namely, that the nucleon knocked out by the neutrino just interacts elastically while traveling off the nucleus.

The χ^2 comparison presented in Table D.1 shows good agreement of the ROP results with the measurements with a $\chi^2/d.o.f.$ close to 1. As shown in Appendix D, this strong preference for the ROP model is driven up by bins with high proton momentum in the cross

sections as function of p_N with $0.3 < \cos\theta_N^L < 0.8$ and $0.8 < \cos\theta_N^L < 1.0$.

5.1.3 1μCC0πNp: Inferred variables

Measuring multiple particles in the final state, like a muon and the ejected proton in the case of the semi-inclusive reactions being analyzed, opens the possibility to measure not only cross sections as function of each particle kinematics but also as function of variables that depend on both particles' kinematics at the same time. One of these types of variables, that somehow measure correlations between the muon and the proton in the final state, are the so-called inferred variables (IV) [115]. The IV variables are defined as

$$\begin{aligned} \Delta p &= |\mathbf{p}_N| - \left|\mathbf{p}_N^{\text{inf}}\right|, \\ \Delta\theta &= \arccos\left(\hat{\mathbf{p}}_N^{\text{inf}} \cdot \hat{\mathbf{z}}\right), \\ |\Delta\mathbf{p}| &= \left|\mathbf{p}_N - \mathbf{p}_N^{\text{inf}}\right|, \end{aligned} \tag{5.1}$$

where $\hat{\mathbf{z}}$ denotes the neutrino beam direction and $\mathbf{p}_N^{\text{inf}} = \mathbf{k}_\nu^{\text{inf}} - \mathbf{k}'$ is the final proton momentum inferred under the hypothesis that the neutrino interacts with a neutron at rest having mass $\tilde{m}_n = m_n - E_b$ (with E_b=25 MeV for carbon), namely

$$\mathbf{k}_\nu^{\text{inf}} = \frac{m_p^2 - m_\mu^2 + 2E_l\tilde{m}_n - \tilde{m}_n^2}{2\left(\tilde{m}_n - E_l + k'\cos\theta_l\right)}\ \hat{\mathbf{z}}, \tag{5.2}$$

where m_p and m_μ are the proton and muon masses, respectively. Notice that, according to Eq. (5.1) and Eq. (5.2), the definition of the inferred proton kinematics relies on the same QE expression used, for example, in the estimation of neutrino energy at T2K far detector. Consequently, the observed deviations from the expected proton inferred kinematic imbalance could provide hints of the biases that may be caused from the mismodeling of nuclear effects in neutrino oscillation measurements at T2K [115].

In Figs. 5·4, 5·5 and 5·6 we show the predictions of the models as function of the inferred

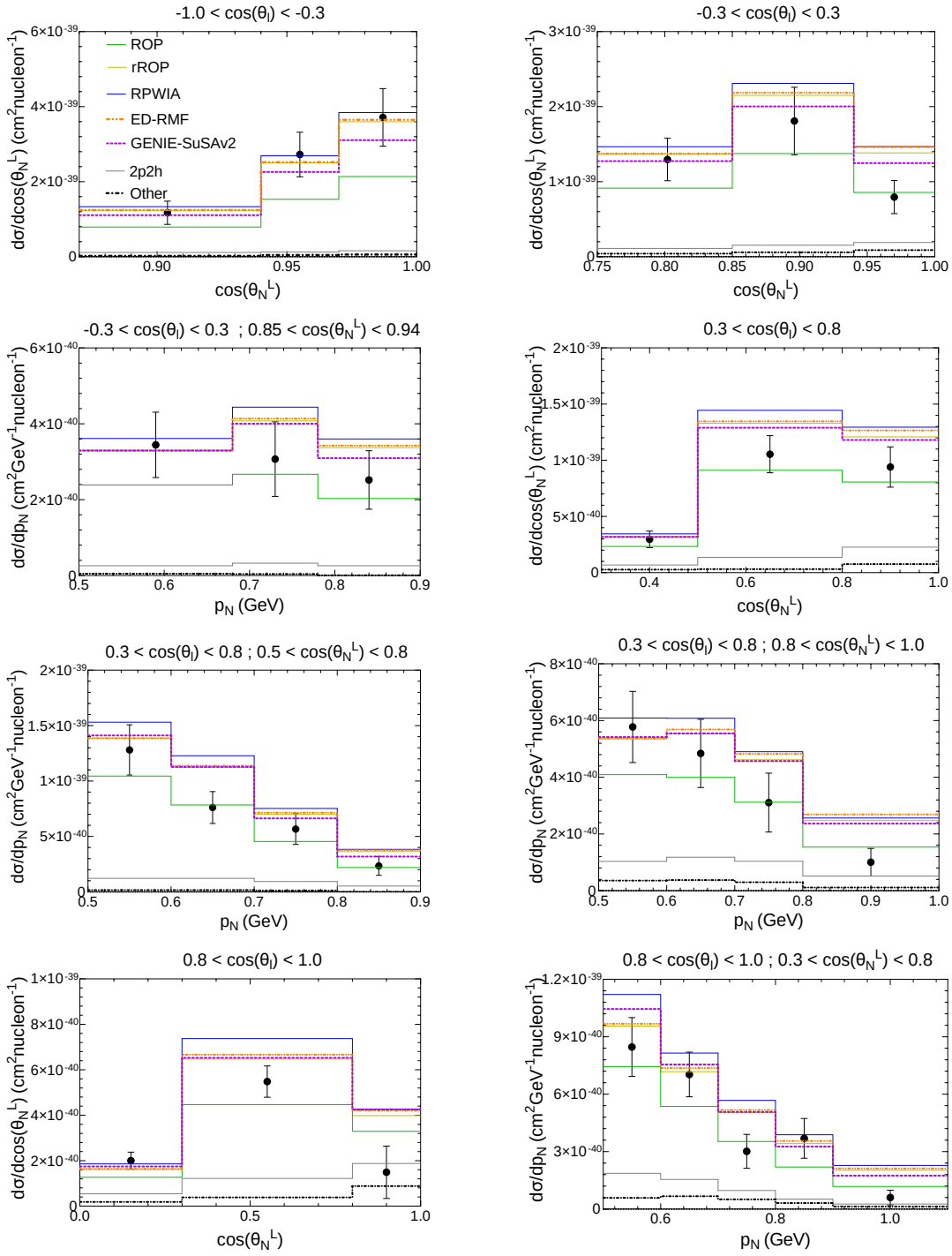

Figure 5·2: T2K 1μCC0πNp semi-inclusive $\nu_\mu - ^{12}$C cross section with at least one proton in the final state with momentum above 0.5 GeV as function of the leading proton and muon kinematics. All curves include the 2p2h and pion absorption (denoted "other") contributions evaluated using GENIE (shown separately). Cross-section measurements taken from [115].

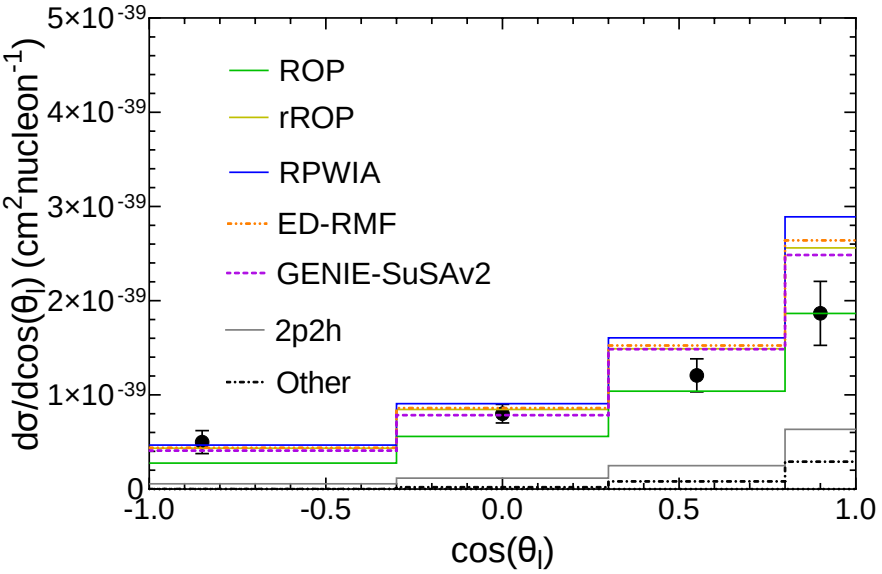

Figure 5·3: T2K 1μCC0πNp semi-inclusive $\nu_\mu - ^{12}$C cross section with at least one proton in the final state with momentum above 0.5 GeV as function of the muon scattering angle. All curves include the 2p2h and pion absorption (denoted "other") contributions evaluated using GENIE (shown separately). Cross-section measurements taken from [115].

variables compared with T2K measurements [115] that applied certain kinematic restrictions to the proton momentum and angle, namely $p_N > 0.45$ GeV and $\cos\theta_N^L > 0.4$. Based on the results of the GENIE-SuSAv2 2p2h model and GENIE's pion absorption predictions there are angular bins with areas heavily dominated by non-QE channels, especially for the cross sections as function of Δp and $|\Delta \mathbf{p}|$ in bins with small scattering angle and low momentum of the muon. For the $|\Delta \mathbf{p}|$ distribution there is a clear preference to require significant non-QE contributions in the high momentum imbalance tail for the higher muon momentum, intermediate muon scattering angle slices, where the microscopic calculation shows small FSI effects by comparing the RPWIA results with the ED-RMF and rROP predictions. Regarding the comparison of the different QE predictions, the biggest differences between the GENIE-SuSAv2, the ED-RMF and rROP microscopic results can be found at forward angles and low muon momentum, especially in the Δp and $|\Delta \mathbf{p}|$ cross sections, where the GENIE-SuSAv2 estimation can be up to 50% higher than the ED-RMF result.

This might be caused by the limitations of SuSAv2 model to describe correctly low-energy nuclear effects and scaling violations in the forward region. Even with this severe reduction compared with the results from GENIE-SuSAv2, the ED-RMF and rROP models still overestimate the cross-section measurements in these forward angles and/or low momentum bins due to a large contribution coming from non-QE channels. This might be related to an overestimation of the 2p2h contribution associated to the extrapolation performed in GENIE to connect the inclusive 2p2h hadronic tensor evaluated microscopically to the semi-inclusive one used to simulate these cross sections. The disagreement may eventually be resolved by performing a fully semi-inclusive calculation where both the leptonic and hadronic variables are consistently handled. Notice that the agreement with the cross-section measurements is improved in the bin with forward angles and high muon momentum ($k' > 0.75$ GeV) at low $|\Delta\mathbf{p}|$, but that the non-QE contributions at higher $|\Delta\mathbf{p}|$ seems to remain too large. It is also interesting to note that for the $\Delta\theta$ cross section in the bin with the most backward-going muons, the GENIE-SuSAv2 prediction falls below cross-section measurements and is even lower than the ROP estimation around zero imbalance, which might indicate too strong FSI. Additionally, the bin with the largest non-QE contribution seems to be $0.0 < \cos\theta_l < 0.8$ and $k' < 0.25$ GeV according to the GENIE simulation, which is described well by all the different models in the $\Delta\theta$ case but significantly overestimated by all the models in the Δp and $|\Delta\mathbf{p}|$ cases as discussed earlier. The χ^2-values shown in Table D.1 are large compared with the *d.o.f.* for the three inferred variables, with the worst agreement obtained for the $\Delta\theta$ distribution. For this specific case, as explained in Appendix D, large contributions to χ^2 come from two specific bins with very small cross section. If those bins are removed, agreement of the models based on RDWIA with the measurements is matched (rROP and ED-RMF) or improved (ROP) with respect to the GENIE-SuSAv2 model.

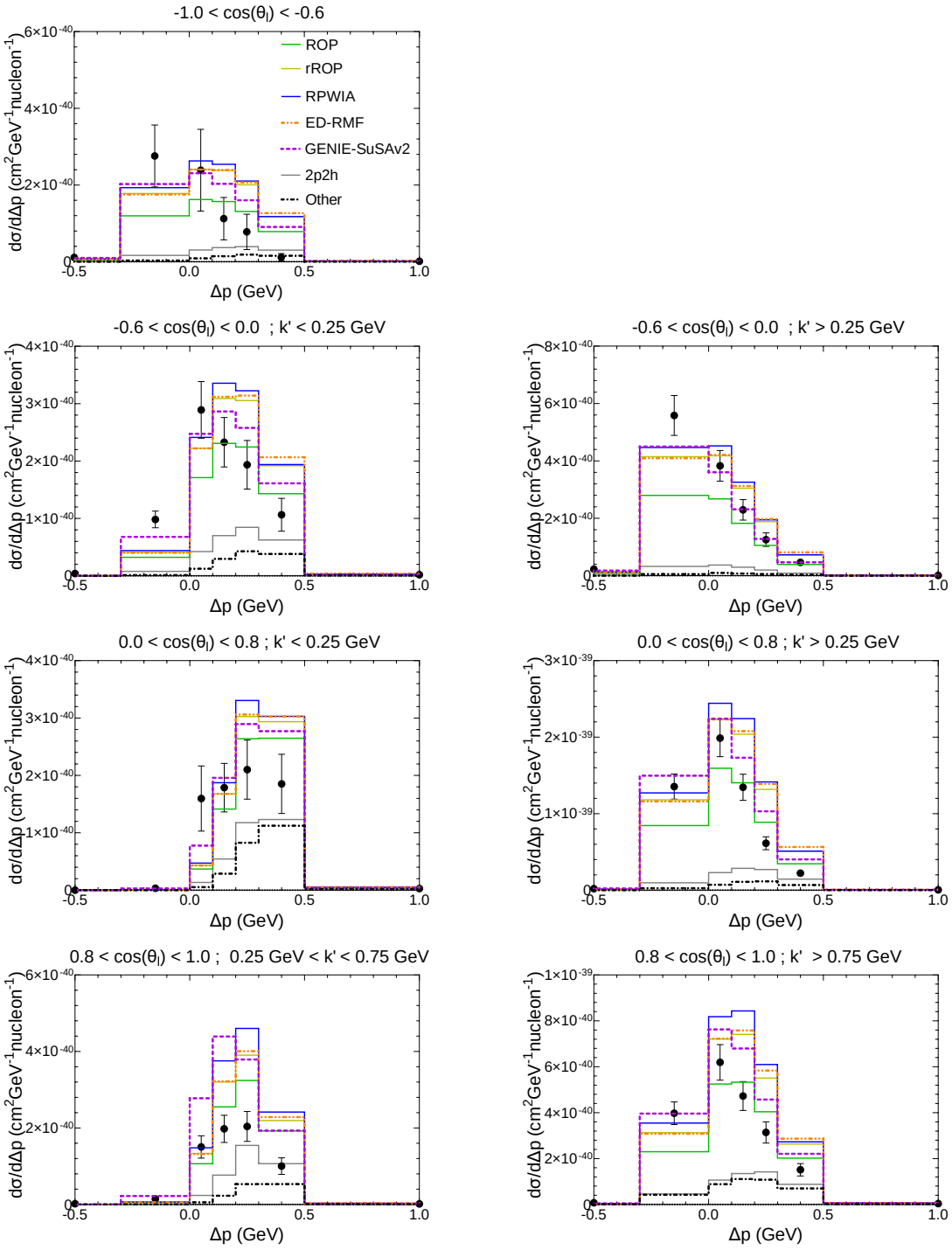

Figure 5·4: T2K 1μCC0πNp semi-inclusive $\nu_\mu - ^{12}$C cross section as function of the inferred variable Δp for different muon kinematic bins. All curves include the 2p2h and pion absorption (denoted "other") contributions evaluated using GENIE (shown separately). Cross-section measurements taken from [115].

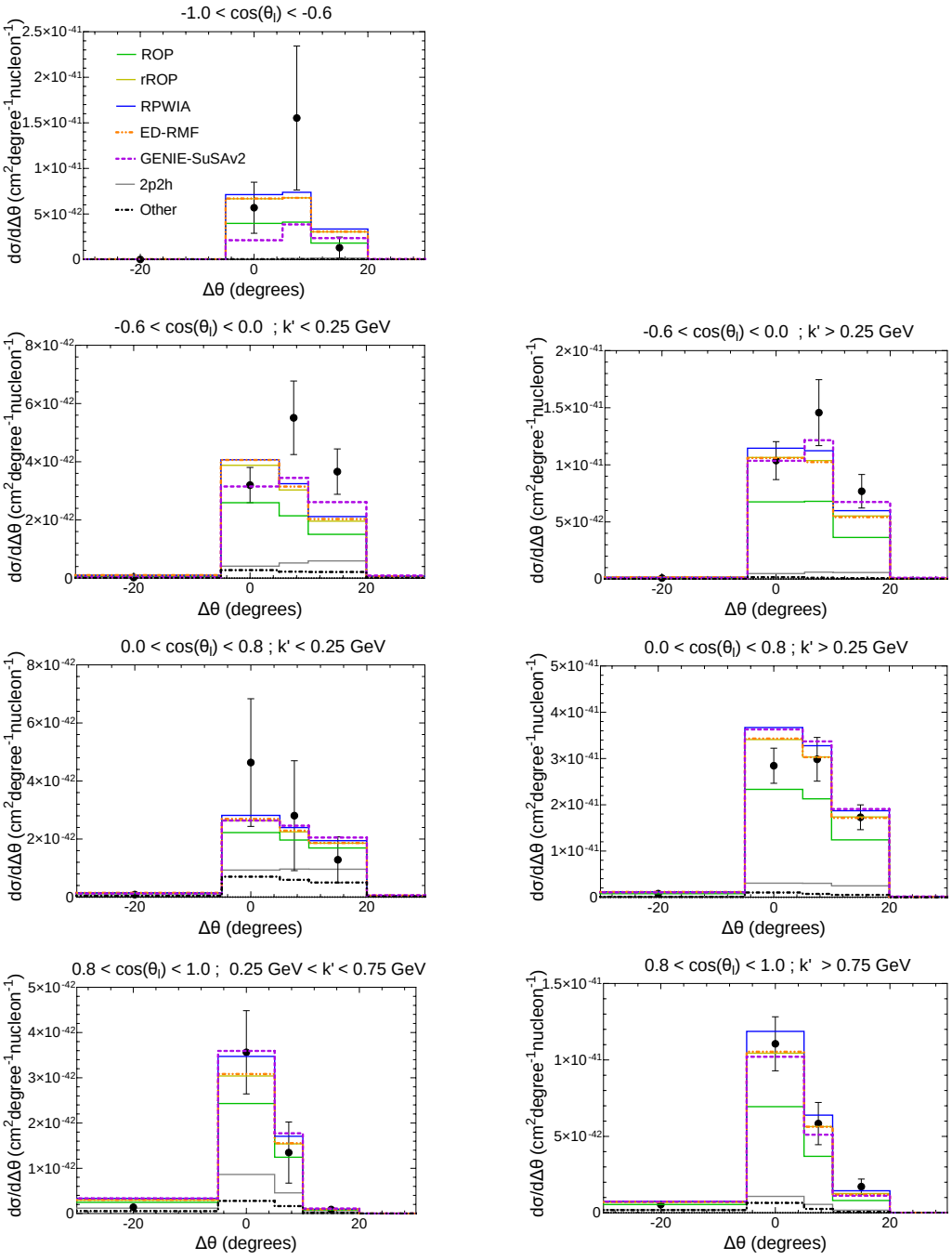

Figure 5·5: T2K 1μCC0πNp semi-inclusive $\nu_\mu - ^{12}$C cross section as function of the inferred variable $\Delta\theta$ in different muon kinematic bins. All curves include the 2p2h and pion absorption (denoted "other") contributions evaluated using GENIE (shown separately). Cross-section measurements taken from [115]. For readability, the axis range has been reduced to $[-30°, +30°]$ hiding an experimental bin above 30° with very low cross section and centering the $[-360°, -5°]$ experimental bin around $-20°$.

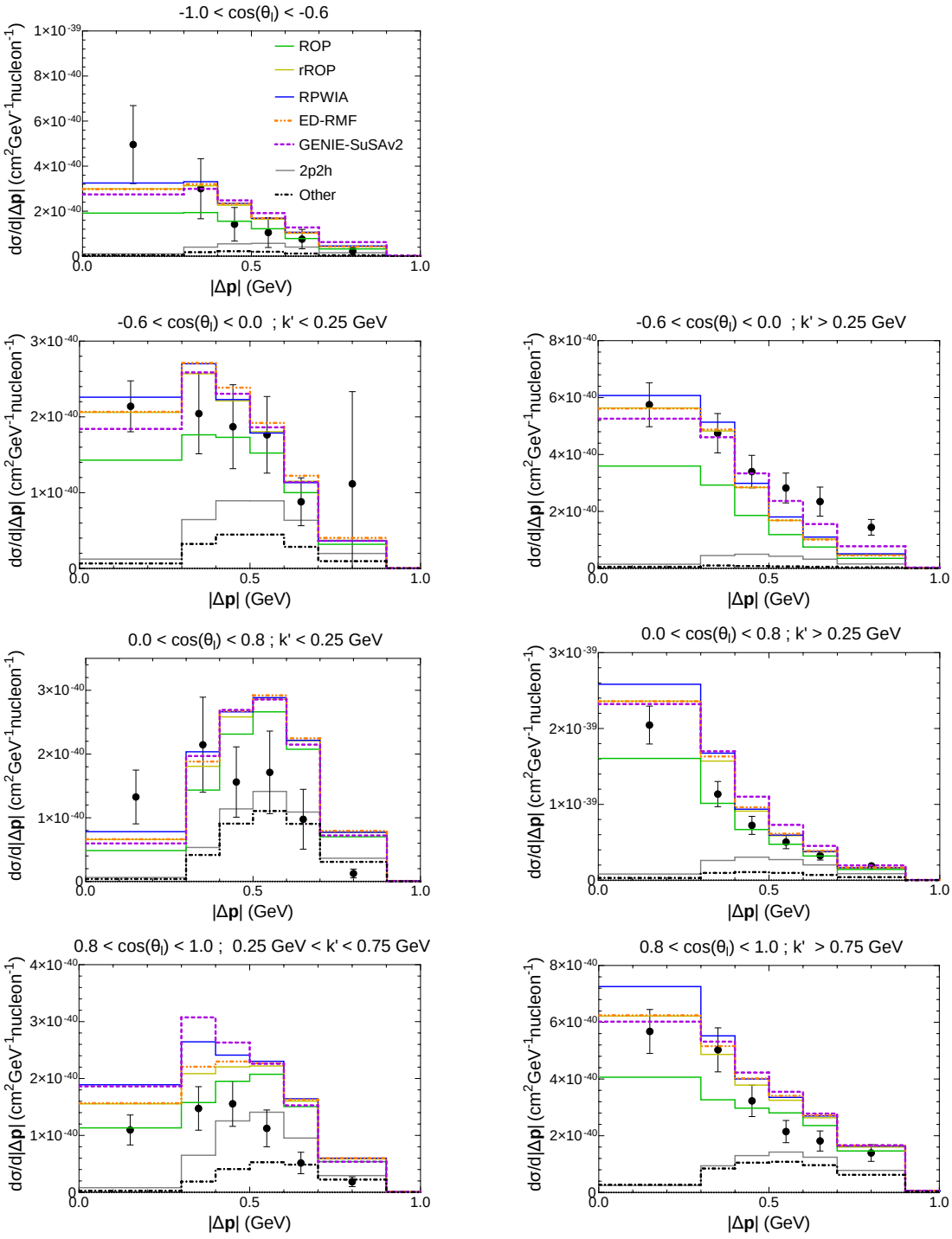

Figure 5·6: T2K 1μCC0πNp semi-inclusive $\nu_\mu - ^{12}$C cross section as function of the inferred variable $|\mathbf{\Delta p}|$ in different muon kinematic bins. All curves include the 2p2h and pion absorption (denoted "other") contributions evaluated using GENIE (shown separately). Cross-section measurements taken from [115].

5.1.4 1μCC0πNp: Transverse kinematic imbalances

Another type of variables that can be used to analyze correlations between the particles detected in the final in semi-inclusive reactions are the so-called transverse kinematic imbalances (TKI) [120]. TKI are designed to enhance experimental sensitivity to nuclear effects, and therefore discriminate between different models, with minimal dependence on the neutrino energy. In particular, the use of TKI can help in disentangling effects linked to FSI, initial state correlations and/or multi-nucleon excitations (2p2h). They are defined by projecting the final lepton and the ejected nucleon momenta on the plane perpendicular to the neutrino direction (transverse plane) as can be seen in Fig. 5·7. More specifically, the vector magnitude

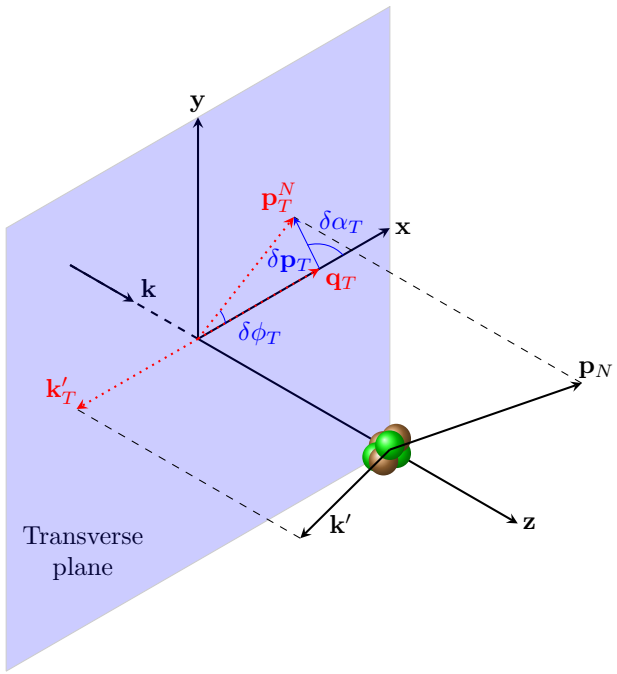

Figure 5·7: Scheme showing transverse kinematic imbalances (TKI): δp_T, $\delta\alpha_T$ and $\delta\phi_T$. The final lepton and nucleon momenta are projected on the plane perpendicular to the neutrino direction (xy-plane or transverse plane). The transverse component of the transferred momentum ($\mathbf{q}_T$) equals $-\mathbf{k}'_T$ and defines the x-axis.

of the momentum imbalance (δp_T) and the two angles ($\delta\alpha_T$ and $\delta\phi_T$) are:

$$\delta p_T = |\delta \mathbf{p_T}| = |\mathbf{k'_T} + \mathbf{p_{N,T}}| \ , \tag{5.3}$$

$$\delta\alpha_T = \arccos\left(-\frac{\mathbf{k'_T}\cdot\delta\mathbf{p_T}}{|\mathbf{k'_T}|\ |\delta\mathbf{p_T}|}\right) \ , \tag{5.4}$$

$$\delta\phi_T = \arccos\left(-\frac{\mathbf{k'_T}\cdot\mathbf{p_{N,T}}}{|\mathbf{k'_T}|\ |\mathbf{p_{N,T}}|}\right) \ , \tag{5.5}$$

where $\mathbf{k'_T}$ and $\mathbf{p_{N,T}}$ are, respectively, the projections of the final lepton and nucleon momentum on the transverse plane (if the neutrino direction is taken as the z-axis, then the projections only have components in the xy-plane as it is shown in Fig. 5·7). In the absence of FSI and assuming a pure QE event, the momentum imbalance is generated entirely by the description of the initial nuclear state dynamics [120, 121]. In this approximation δp_T is a direct measurement of the transverse component of the bound nucleon momentum distribution, therefore the RFG model, widely used in neutrino event generators, would be at a disadvantage compared to more realistic nuclear models like the independent-particle shell model or the spectral function model [115, 121]. This was explicitly shown in Ref. [51], where the RFG was found to give a much poorer description of the δp_T distribution than the IPSM in PWIA. Also in the PWIA limit, the $\delta\alpha_T$ distribution is expected to be flat due to the isotropy property shown by the nucleon momentum distribution, although presence of FSI and other effects beyond the impulse approximation break this behavior.

The comparison of the cross sections as function of the transverse kinematic imbalances for the different models with T2K measurements is presented in Fig. 5·8. For these data, the following phase-space restrictions are applied: $k' > 0.25$ GeV, $\cos\theta_l > -0.6$, $0.45 < p_N < 1.0$ GeV and $\cos\theta_N^L > 0.4$. The δp_T distribution shown in Fig. 5·8 favours the ED-RMF and rROP calculations over the GENIE-SuSAv2 predictions in the low δp_T region, which is mainly dominated by initial-state effects with negligible contribution from the 2p2h and pion absorption channels. This could be caused by the inconsistencies of the implementation

of the SuSAv2 model, which is based on the RMF theory, in GENIE, that generates the initial state nucleon using a local Fermi gas model. For imbalances above the Fermi level, nucleon-nucleon correlations become more important and the microscopic calculation predicts small FSI effects. In this region all the microscopic models except the ROP model overestimate the cross-section measurements after including the non-QE contributions calculated with GENIE. Note that this comparison between theory and experiment does present some inconsistency because the 2p2h contribution is calculated with a Fermi gas while the microscopic calculations for the QE process use the RMF model with corrections to include nucleon-nucleon correlations. In any case, it is clear that the QE contribution with nucleon-nucleon correlations included is not enough to describe the region of high-momentum imbalance and additional contributions are essential to describe the experimental results. For the distribution as function of δp_T shown in Fig. 5·8 there is an additional model called "RFG", which corresponds to the predictions based on the plane-wave approximation using the RFG model for the initial state as described in Sec. 2.3.1. The RFG prediction greatly overestimates the measurements, while RPWIA with a realistic description of the initial state (see Sec. 3.1) yields a lower and shifted to the left cross section. Of course some kind of FSI and non-QE contributions must be added to improve the agreement with the data, but qualitatively one can see that, even in the plane-wave limit, this imbalance is largely affected by the description of the initial nuclear state.

Regarding the angular TKI, $\delta\phi_T$ is more dependent on the neutrino energy and less sensitive to nuclear effects than δp_T [120]. The variable $\delta\alpha_T$ measures with good approximation the angle between the initial nucleon momentum and the transferred momentum [120]. All the model predictions except ROP as function of $\delta\phi_T$ shown in Fig. 5·8 overestimate the cross-section measurements, although the overestimation is less severe in the case of the ED-RMF and rROP models for low values of $\delta\phi_T$ compared with GENIE-SuSAv2. In the case of $\delta\alpha_T$, it is expected to have a rather flat distribution due to the isotropy of the momentum

distribution of the bound nucleon which is broken mainly by non-QE effects and FSI, although this deviation from flatness is partially washed out by the constraint on the outgoing proton kinematics in current experimentally accessible signal definitions. However, it is interesting to note that all of the microscopic models, including RPWIA, predict a significant QE-driven rise in $\delta\alpha_T$ when there is no or low proton momentum threshold (although this is not shown here), in contrast to what is often predicted by neutrino event generators. In the results presented in Fig. 5·8 there is an overestimation of the cross-section measurements by all the models except the ROP, which is less significant for the microscopic calculations using the ED-RMF and rROP models compared with GENIE-SuSAv2 results specially at high $\delta\alpha_T$ values. The non-QE contributions become more relevant for higher values of $\delta\alpha_T$ where the biggest differences between the microscopic and the GENIE-SuSAv2 calculations also appear, with the former in better agreement with the cross-section measurements. The differences between both kinds of calculations could be explained by the different treatment of FSI. Simulations performed with the neutrino event generator NuWro [122], which also uses a semi-classical cascade model for FSI with tuned parameters, are in better agreement with the microscopic calculation than with GENIE-SuSAv2. Quantitatively, χ^2 values summarized in Table D.1 correspond to values of $\chi^2/d.o.f.$ close to 1 for the ROP model for the three TKI variables, with the best agreement found for the $\delta\alpha_T$ distribution.

5.2 MINERνA

The MINERνA collaboration measured [116, 117] semi-inclusive 1μCC0πNp events on ^{12}C and presented the differential cross section results as function of the muon and leading proton kinematics, and also as function of TKI. The experimental constrains applied in this case are summarized in Table 5.1.

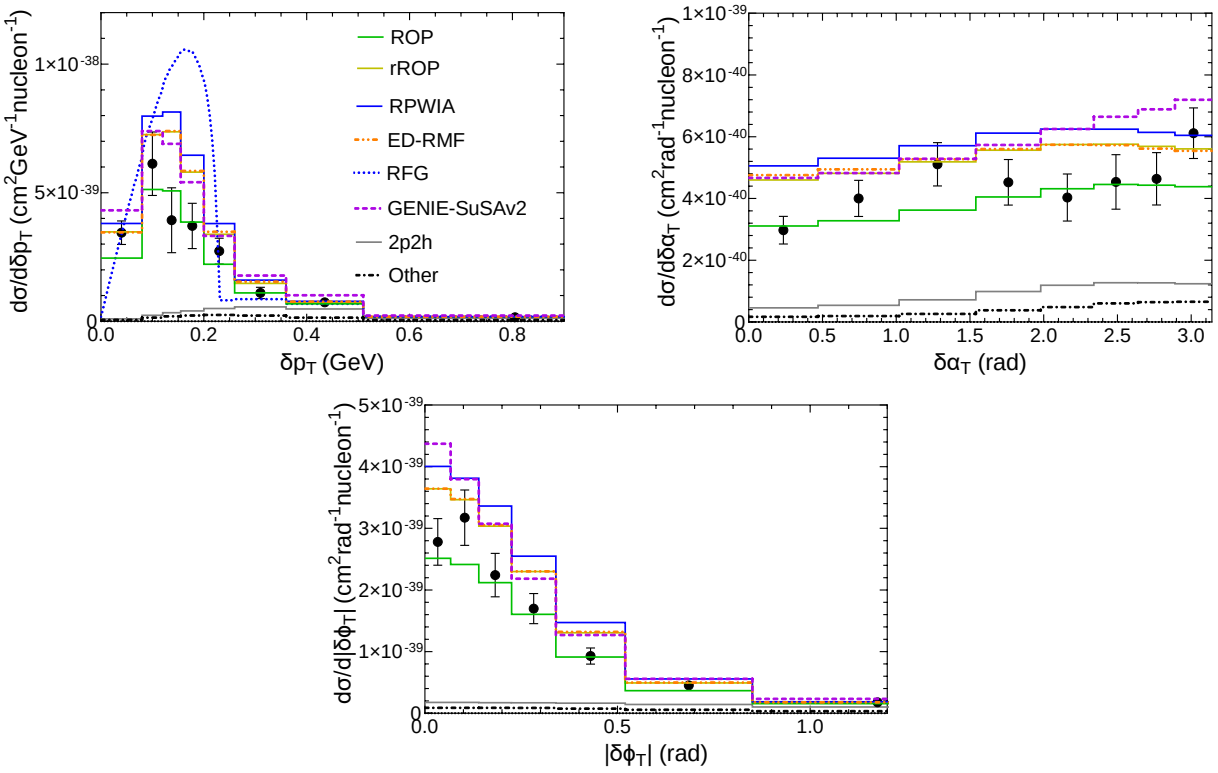

Figure 5·8: T2K 1μCC0πNp semi-inclusive $\nu_\mu - {}^{12}$C cross sections as function of the transverse kinematic imbalances δp_T, $\delta\alpha_T$ and $|\delta\phi_T|$. All curves include the 2p2h and pion absorption (denoted "other") contributions evaluated using GENIE (shown separately). Cross-section measurements taken from [115].

MINERνA	k' (GeV)	$\cos\theta_l$	p_N (GeV)	$\cos\theta_N^L$	ϕ_N^L (°)
	1.5-10	> 0.939	0.45-1.2	> 0.342	-

Table 5.1: Phase-space restrictions applied to the semi-inclusive CC0π cross-section measurements with one muon and at least one proton in the final state shown by MINERνA collaboration in [116, 117].

5.2.1 1μCC0πNp: Muon and proton kinematics

Despite a larger contribution from non-quasielastic channels, due to the higher energy neutrino beam compared with T2K (see Fig. 2·4), the semi-inclusive cross sections predicted by ROP, shown in Fig. 5·9 as function of the muon and proton kinematics together with the

other models, seem qualitatively in reasonable agreement with experimental measurements, except for the θ_N^L cross section where there is an overestimation in the high-θ_N^L region. This is partially confirmed by the χ^2-values presented in the legend of Fig. 5·9, which shows ROP as the favored model that best matches the measurements of muon and proton kinematic variables. Whilst all models other than ROP overestimate the cross section data, the agreement between the ED-RMF, rROP and the GENIE-SuSAv2 predictions is very good except for the p_N distribution where differences can be seen in the whole interval of proton momentum. It should be noted that the apparent overestimation of the non-ROP models (and the outstanding agreement with the data of the ROP model) may be due to a mismodeling of the strength of the 2p2h or pion absorption contributions calculated with GENIE and may therefore not suggest an issue in the modeling of the QE channel.

5.2.2 1μCC0πNp: Transverse kinematic imbalances

In Fig. 5·10 the results of the different FSI models with the MINERνA cross-section measurements of the TKI distributions are presented. Even without adding the non-QE contributions, all the models except ROP overestimate the data in the peak of the δp_T distribution. In the high-momentum imbalance tail the contribution from the non-QE channels are sufficient and clearly necessary to match any prediction with the experimental cross section. A similar situation is found for the $\delta\phi_T$ cross section where all the models except ROP overestimate the cross-section measurements near zero imbalance and non-QE contributions are clearly required to describe the tail of the distribution. Regarding the $\delta\alpha_T$ results, it is interesting to point out the appearance of a clear peak at large values of the imbalance in the MINERνA cross-section data that is not present in the T2K cross-sections shown in Fig. 5·8, which might be caused by additional non-quasielastic contributions present in MINERνA due to the higher energy of the neutrinos. In case of T2K results shown in Fig. 5·8, it has been shown [123] that the T2K restriction of the proton momentum to be above 0.45

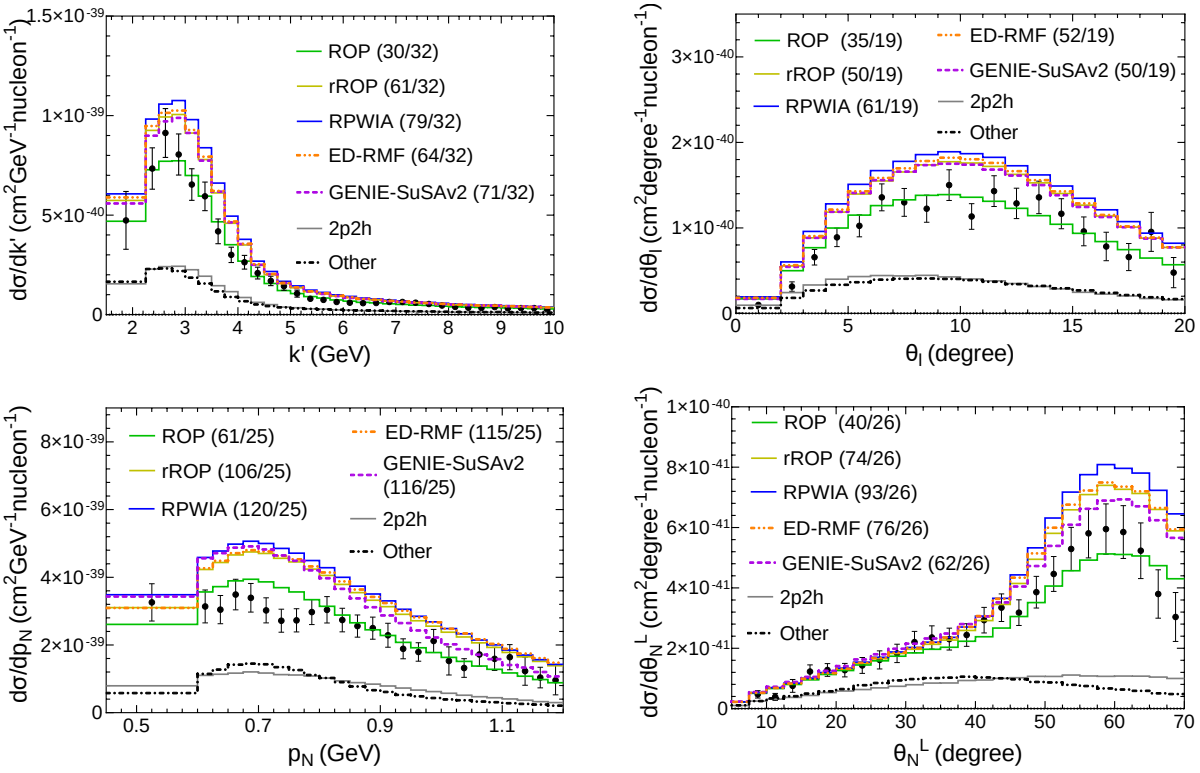

Figure 5·9: MINERνA 1μCC0πNp semi-inclusive $\nu_\mu - {}^{12}$C cross section as function of the final muon momentum and scattering angle (top) and as function of the final proton momentum and polar angle (bottom). All curves include the 2p2h and pion absorption (denoted "other") contributions evaluated using GENIE (shown separately). The original paper from MINERνA was [117] but the cross-section measurements shown here were taken from [116] which corrected a mismodelling in GENIE's elastic FSI that affected the cross-section measurements presented in the first paper. The $\chi^2/d.o.f.$ ratio is given in brackets in the legend of each distribution.

GeV removes most of the interactions in which FSI plays an important role eliminating the peak at large $\delta\alpha_T$. The GENIE-SuSAv2 prediction and all the RDWIA results except the ROP overestimate the cross-section data, although the shape of the rise in $\delta\alpha_T$ seems to be well described by the combination of FSI and non-QE contributions except the last bin. Additional projections on the plane perpendicular to the neutrino direction of the momentum imbalance δp_T are also presented in Fig. 5·10. If the interaction occurred on a free nucleon at rest, then we would expect a delta-function at $\delta p_T = 0$ because the muon

and the proton in the final state would be perfectly balanced in that case. Therefore, the width of the QE peak is mostly consequence of the Fermi motion. In PWIA δp_{T_y} is exactly the projection on the y-axis of the initial nucleon momentum and, due to the isotropy of the nucleon momentum distribution, the δp_{T_y} distribution is symmetrical. On the other hand δp_{T_x} is parallel to the transferred momentum in the transverse plane (see Fig. 5·7), which is translated into a small shift of the peaks towards positive values of δp_{T_x}. In the δp_{T_x} distribution the GENIE-SuSAv2 prediction is very similar to the ED-RMF and rROP models in the region of the peak, with all the results overestimating the cross-section measurements in this region except for ROP. Furthermore, GENIE-SuSAv2 differs slightly from the other models in the prediction of the asymmetric tail of the distribution where the non-QE channels contribute more than the 1p1h channel. The non-QE contributions seems to perfectly match the tails of the distribution when added to ROP, although alterations to the uncertain contributions coming from the pion absorption (and, to some extent, 2p2h) contribution calculated with GENIE may allow all the models other than RPWIA to match the cross-section measurements. Note that in all comparisons there is no evidence for a need of a significant enhancement of the 2p2h contribution, as is often suggested to be required by MINERνA measurements [117, 124]. The χ^2 comparison for each TKI variable is shown in the legends of Fig. 5·10 and shows that the best agreement is systematically obtained with the ROP model, although the $\chi^2/d.o.f.$ values are far above 1 for all the TKI variables.

5.3 MicroBooNE

In this section the semi-inclusive cross section measurements on argon performed by MicroBooNE collaboration [118, 119, 125] are compared with the RDWIA calculation using the ROP and ED-RMF models and the GENIE-SuSAv2 predictions. So far we have only shown ν_μ semi-inclusive cross sections, however the MicroBooNE collaboration presented for the first time cross section measurements using a ν_e beam. The differential cross sections are available

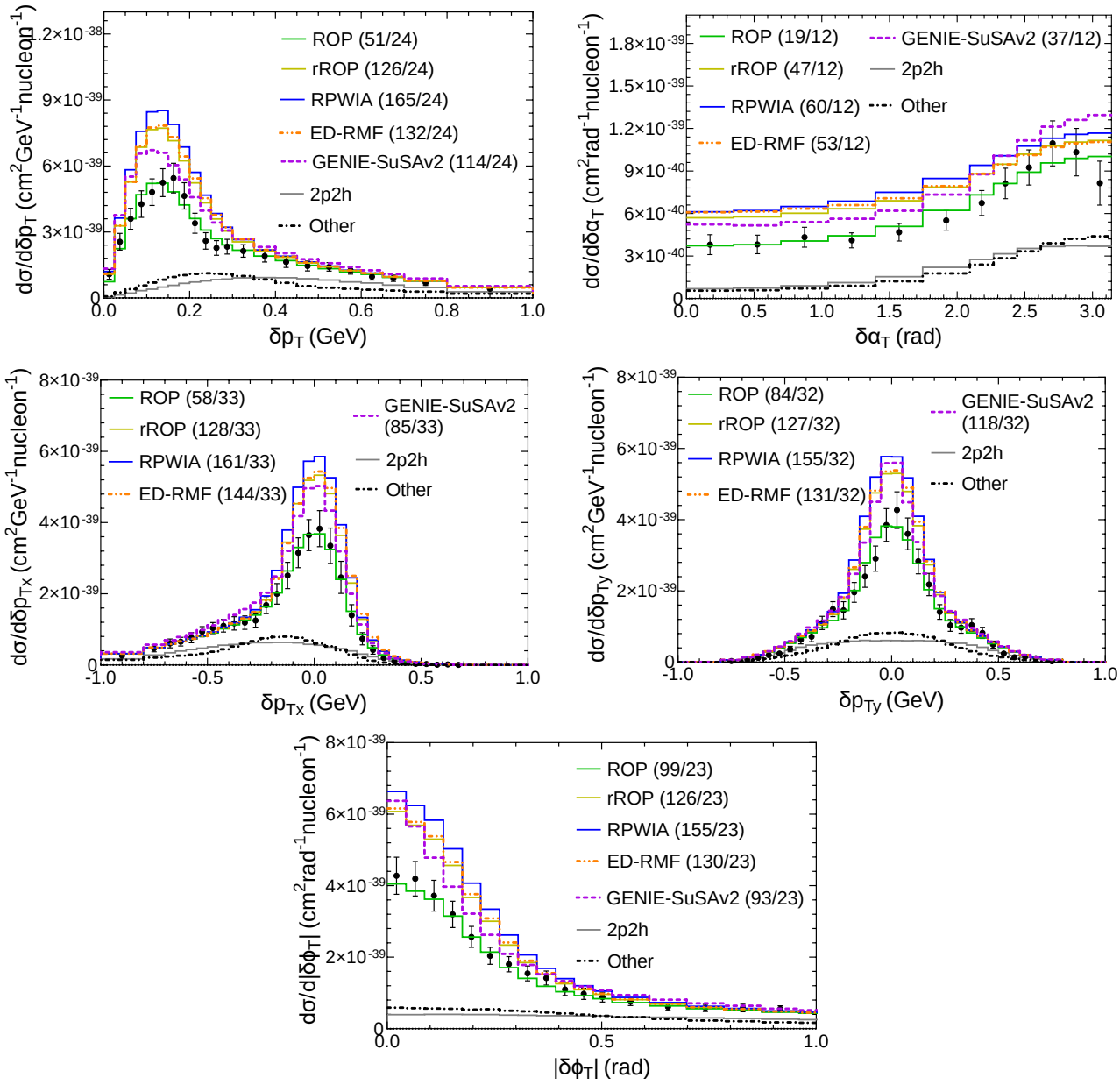

Figure 5·10: MINERνA 1μCC0πNp semi-inclusive ν_μ–^{12}C cross sections as function of the transverse kinematic imbalances δp_T, δp_{Tx}, δp_{Ty}, $\delta\alpha_T$ and $|\delta\phi_T|$. All curves include the 2p2h and pion absorption (denoted "other") contributions evaluated using GENIE (shown separately). The original paper from MINERνA was [117] but the cross-section measurements shown here were taken from [116] which corrected a mismodeling in GENIE's elastic FSI that affected the cross-section measurements presented in the first paper. Notice that the convention used in [116] to define the x and y axis to project δp_T on is the opposite to the convention used in this thesis. The $\chi^2/d.o.f.$ ratio is given in brackets in the legend of each distribution.

1μCC0πNp	k' (GeV)	$\cos\theta_l$	p_N (GeV)	$\cos\theta_N^L$	ϕ_N^L (°)	$\theta_{\mu p}$ (°)	δp_T (GeV)
	> 0.1	-	0.3-1.2	-	-	-	-
1eCC0πNp							
	> 0.0305	-	> 0.3105	-	-	-	-
1μCC0π1p							
	0.1-1.5	-0.65-0.95	0.3-1.0	> 0.15	145-215	35-145	< 0.35

Table 5.2: Phase-space restrictions applied to ν_μ−^{40}Ar 1μCC0πNp [118] and 1μCC0π1p [119] and ν_e−^{40}Ar $1e$CC0πNp [125] cross section measurements performed by MicroBooNE collaboration. The opening angle $\theta_{\mu p}$ is defined as the angle between the muon and the ejected proton and δp_T is the transverse momentum imbalance.

for three different final-state topologies: 1μCC0πNp (one muon and at least one proton), $1e$CC0πNp (one electron and at least one proton) and 1μCC0π1p (one muon, exactly one proton above experimental threshold and any protons below threshold). As explained in Sec. 3.1, the RDWIA results for argon are presented with colored bands that show the uncertainty in the theoretical QE calculation due to the uncertainty on the modeling of the ^{40}Ar missing energy profile (see Table 3.2 and Fig. 3·2). The phase-space restrictions applied to each set of measurements divided by topologies are summarized in Table 5.2.

5.3.1 1μCC0πNp: Reconstructed muon and proton kinematics

In Fig. 5·11 we compare the ROP and ED-RMF results and the GENIE-SuSAv2 predictions with MicroBooNE 1μCC0πNp data for ^{40}Ar [118]. The cross sections are shown as function of the muon and proton kinematics and also the opening angle $\theta_{\mu p}$, which is defined as the angle between the muon and the leading proton momenta. The experimental cross sections are given as function of reconstructed variables, while our models predict the results as function of true variables. Therefore, we have applied the smearing matrix[1] [118] to all the

[1]Note that the matrix needs to be applied to distributions proportional to the number of events on each bin, not to cross section distributions. Therefore, starting with a cross section distribution as function of a true variable one needs to multiply the distribution by each bin size, apply the smearing matrix, and divide

theoretical results shown in Fig. 5·11. Although not shown here, the cross sections as function of k'^{reco} and p_N^{reco} are the ones most affected by the smearing. All the models presented in the k'^{reco} distribution in Fig. 5·11 exhibit large χ^2 values compared with the *d.o.f.*, giving the ROP model the lowest value. Whilst the GENIE-SuSAv2 and ED-RMF models are in poor agreement with the measured k'^{reco} distribution in Fig. 5·11, the ROP model provides a reasonable description of it with a χ^2 of $\sim$10 for 6 *d.o.f.*.

The shape of the p_N^{reco} distribution is correctly reproduced by the ED-RMF and ROP models once the non-QE contributions are taken in account, although the ED-RMF model overestimates the measurements in the $0.65 < p_N^{\mathrm{reco}} < 0.9$ GeV bins and ROP underestimates the data for low values of p_N. It is interesting to note that the GENIE-SuSAv2 model overestimates the experimental measurement at very low p_N^{reco} (although its good agreement at large p_N^{reco} actually leads to a lower χ^2).

The shape and magnitude of the $\cos\theta_l^{\mathrm{reco}}$ and $\cos\theta_N^{L\,\mathrm{reco}}$ angular distributions are well described by all the models except at very forward muon scattering angles where all the models overestimate the cross-section measurements, although it is worth noting that the underestimation is much less severe in the case of ROP, which provides a quantitatively good description of the distribution. Regarding the $\theta_{\mu p}^{\mathrm{reco}}$ distribution, ED-RMF appears to better describe the shape of the experimental measurement, but both ROP and ED-RMF are quantitatively compatible with the measurement.

The small uncertainty bands obtained for the RDWIA results presented in Fig. 5·11 indicates that the cross sections as function of the muon and proton kinematics, and also as function of the opening angle, are not largely affected by the modification of the parameters that model the missing energy profile of the initial nuclear state.

---

the result again by the bin size in order to obtain the correct cross section distribution as function of a reconstructed variable.

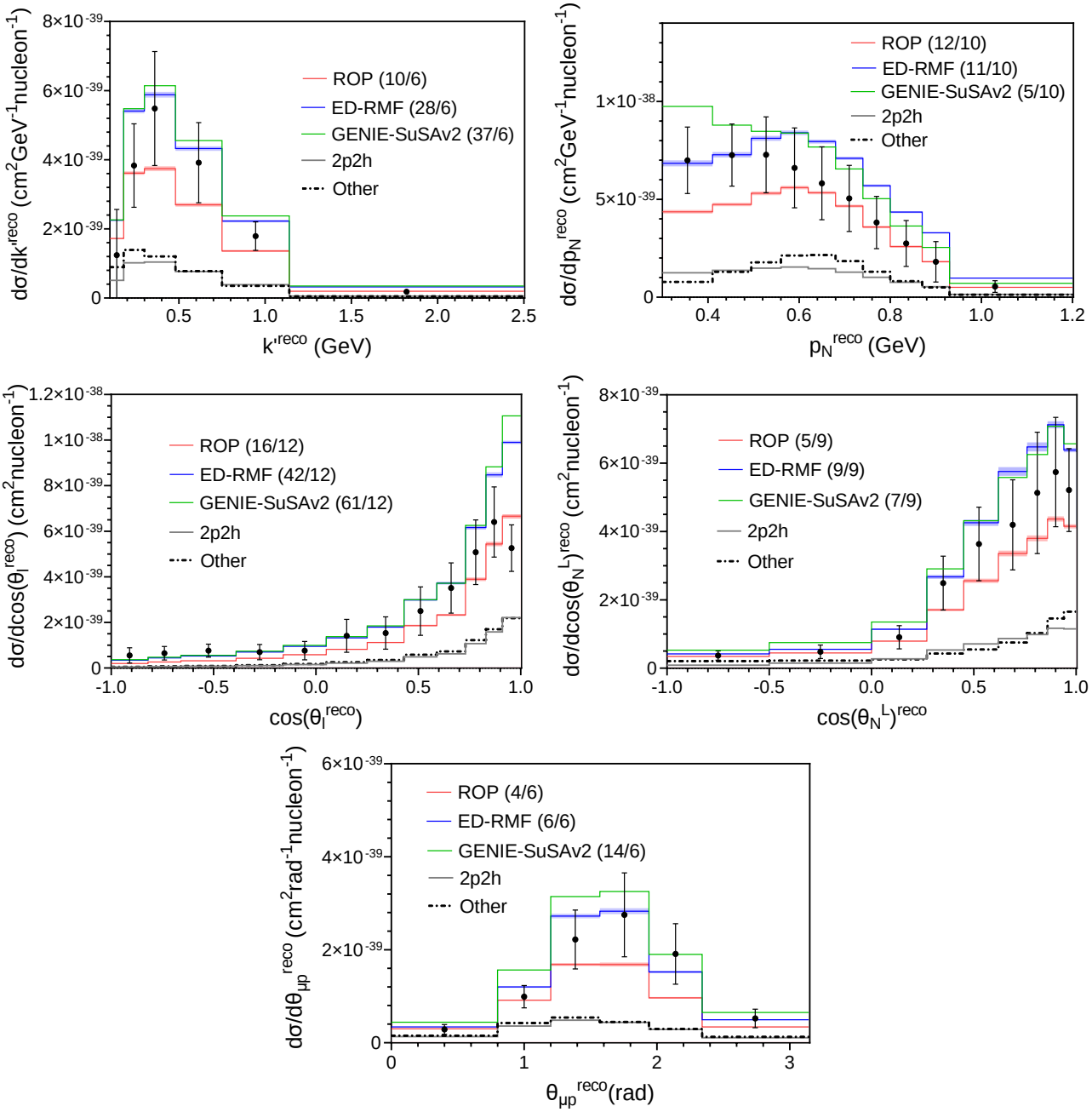

Figure 5·11: MicroBooNE 1μCC0πNp semi-inclusive $\nu_\mu - {}^{40}$Ar cross sections as function of the reconstructed muon and proton momenta and scattering angles and the opening angle $\theta_{\mu p}^{\text{reco}}$. All curves include the 2p2h and pion absorption (denoted "other") contributions evaluated using GENIE (shown separately). Experimental results are from [118]. The bands, drawn for the ED-RMF and ROP models, represent the uncertainties associated with the modeling of the initial nuclear state. The $\chi^2/d.o.f.$ ratio is given in brackets in the legend of each distribution.

5.3.2 $1e$CC0πNp: Electron and proton kinematics

In Fig. 5·12 the different theoretical models are compared with MicroBooNE $1e$CC0πNp data on ^{40}Ar [125] as function of the electron energy and scattering angle and the final proton kinetic energy (T_N) and scattering angle. Additionally, for the T_N distribution presented in Fig. 5·12, MicroBooNE collaboration provides one extra data point ($0 < T_N < 50$ MeV) that corresponds to events with one electron, no protons above $T_N = 50$ MeV threshold and at least one proton below the threshold. Until now we have analyzed ν_μ interactions, however ν_e cross sections differ only in the final lepton mass which appears in kinematic factors in the cross-section expression. Although the experimental measurements are statistically limited and the error bars are large, the ROP model seems to describe better all the measurements presented in Fig. 5·12, whilst both GENIE-SuSAv2 and ED-RMF models tend to overestimate them (nevertheless it should be noted that there is little quantitative power to statistically separate the models). This is consistent with the analysis performed in [125] where the results obtained with different modern neutrino event generators are shown. In that analysis a preference for predictions with lower total cross section was found. As it happened in our previous comparison, these results with ν_e are also not strongly affected by variations in the model of the energy profile of the initial state according to the RDWIA predictions.

5.3.3 1μCC0π1p: Muon and proton kinematics

The MicroBooNE CC0π1p $\nu_\mu-^{40}$Ar measurements [119] are shown in Figs. 5·13 and 5·14 as function of the muon and proton kinematics, together with the RDWIA and GENIE-SuSAv2 predictions.

A noticeable difference with respect to the 1μCC0πNp topology is the negligible contribution of the 2p2h channel in all the distributions. The reason is the kinematic cuts applied to the 1μCC0π1p signal which are summarized in Table 5.2. From a theoretical point of view,

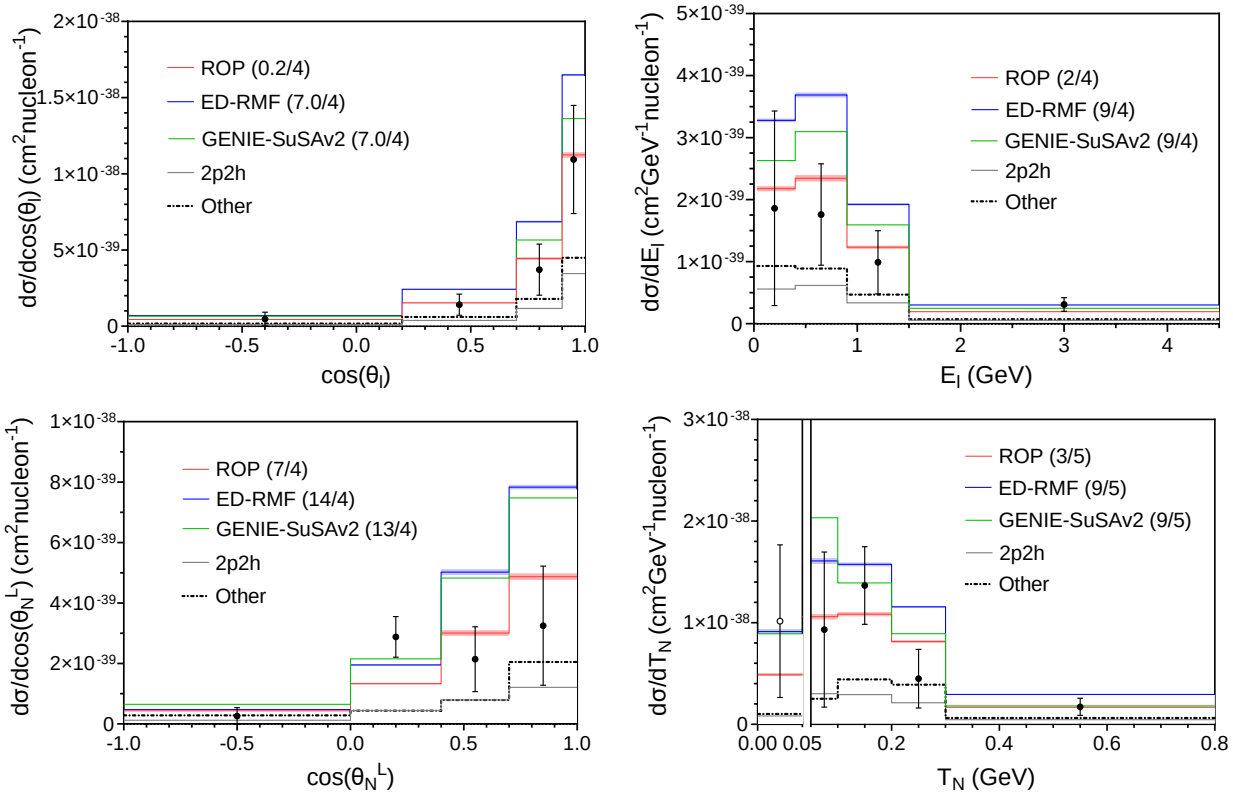

Figure 5·12: MicroBooNE $1e$CC0πNp semi-inclusive ν_e–^{40}Ar cross sections as function of the electron scattering angle and energy and proton kinetic energy and scattering angle. All curves include the 2p2h and pion absorption (denoted "other") contributions evaluated using GENIE (shown separately). Experimental results are from [125]. The bands, drawn for the ED-RMF and ROP models, represent the uncertainties associated with the modeling of the initial nuclear state. The single white point in the T_N distribution between $0 < T_N < 50$ MeV corresponds to an extra $1e$CC0π0p (one electron, no protons above $T_N = 50$ MeV threshold and at least one proton with kinetic energy below the 50 MeV threshold) measurement performed by MicroBooNE [125]. For this single point, additional phase space restrictions on the electron energy ($E_l > 0.5$ GeV) and the electron scattering angle ($\cos\theta_l > 0.6$) are applied. The $\chi^2/d.o.f.$ ratio is given in brackets in the legend of each distribution.

the 1μCC0π1p topology, leaving aside the non-quasielastic contributions, is closer to the picture drawn by the ROP model, in which the imaginary part of the optical potential subtracts all the inelastic nuclear FSI, leaving only the elastic channel (i.e. the outgoing proton interacting elastically with the residual system). The inclusion of the correlated part of the spectral function introduces, in an effective way, states with multiple nucleons being knocked out. Notice that this contribution is very minor in the cross sections shown in Figs. 5·13 and 5·14, in fact, the result obtained after its subtraction is contained within the uncertainty for both RDWIA predictions. The results presented as function of the proton kinematics show good agreement between the ROP and data, while the predictions by the other models overestimate the measured cross sections, especially the ED-RMF model. Regarding the lepton kinematics, the bins around the peak of the k' distributions are slightly underestimated by the ROP but the ED-RMF and GENIE-SuSAv2 overestimate the data in the rest of the bins.

Finally, the $\cos\theta_l$ distribution is shown in Fig. 5·14. The ROP and GENIE-SuSAv2 predictions are within the experimental uncertainty except for the forward angle bin that is overestimated by the GENIE-SuSAv2 and ED-RMF models. However, recent work by the MicroBooNE collaboration [126] shows a $\cos\theta_l$ distribution that is reproduced correctly by different neutrino generators. This suggests that the discrepancy observed in Fig. 5·14 at small muon scattering angles might be due to the use of an old version of the GENIE configuration that accounts for efficiency corrections and beam-induced backgrounds.

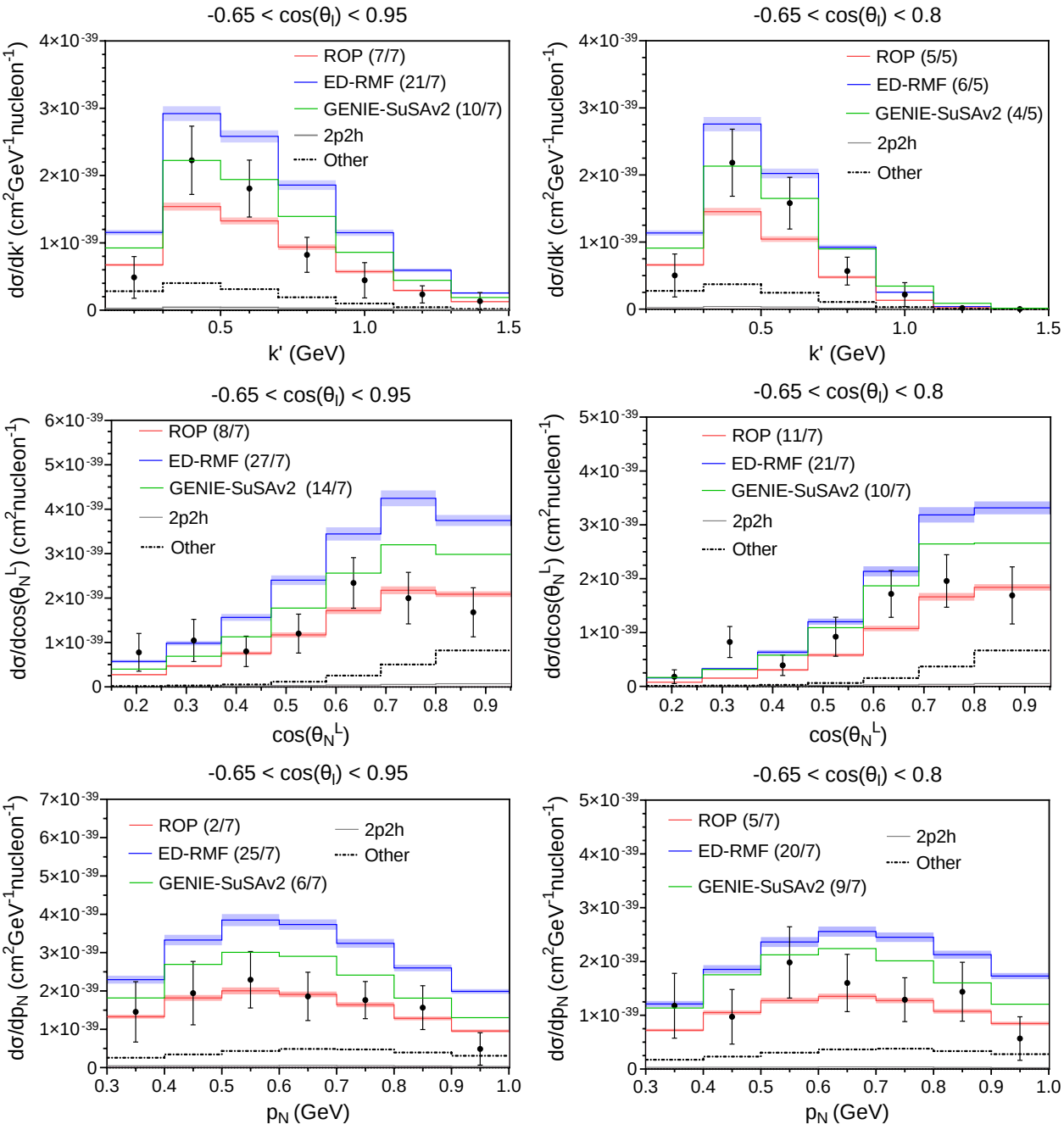

Figure 5·13: MicroBooNE 1μCC0π1p semi-inclusive $\nu_\mu - {}^{40}$Ar cross sections as function of the muon and proton momenta and proton polar scattering angle. All curves include the 2p2h and pion absorption (denoted "other") contributions evaluated using GENIE (shown separately). Experimental results are from [118]. The bands, drawn for the ED-RMF and ROP models, represent the uncertainties associated with the modeling of the initial nuclear state. The $\chi^2/d.o.f.$ ratio is given in brackets in the legend of each distribution.

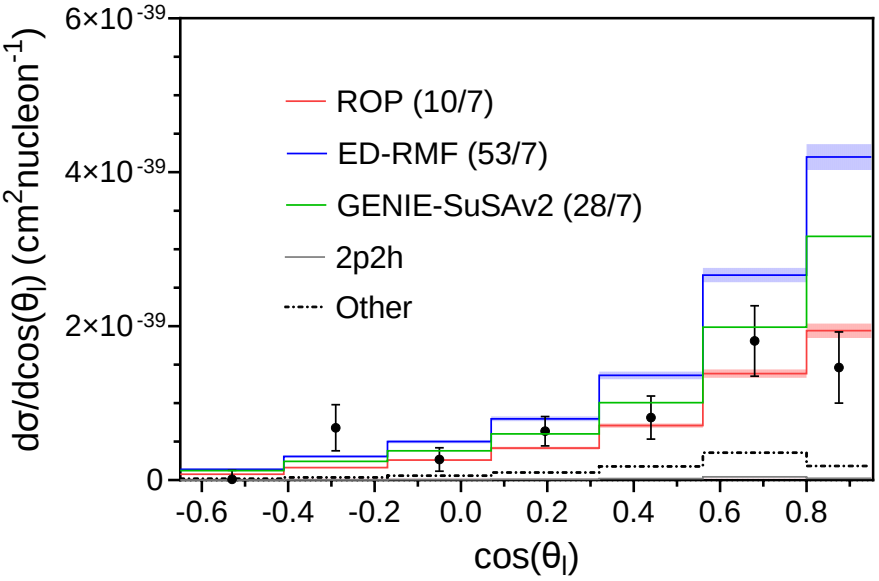

Figure 5·14: MicroBooNE 1μCC0π1p semi-inclusive $\nu_\mu - {}^{40}$Ar cross sections as function of the muon scattering angle. All curves include the 2p2h and pion absorption (denoted "other") contributions evaluated using GENIE (shown separately). Experimental results were taken from [119]. The bands drawn for the ED-RMF and ROP models are related with the uncertainties associated with the modeling of the initial nuclear state. The $\chi^2/d.o.f.$ ratio is given in brackets in the legend of each distribution.

5.3.4 1μCC0π1p: Reconstructed E_ν and Q^2

In Fig. 5·15, we also present the 1μCC0π1p predictions as function of the reconstructed neutrino energy and $Q^2_{\rm CCQE}$, which are defined as follows [119]

$$E_\nu^{\rm cal} = E_l + T_N + 40\ {\rm MeV}\,,$$
$$Q^2_{\rm CCQE} = \left(E_\nu^{\rm cal} - E_l\right)^2 - (\mathbf{k} - \mathbf{k}')^2\,, \tag{5.6}$$

where the argon binding energy is assumed to be 40 MeV. Both RDWIA calculations tend to underestimate (ROP) or overestimate (ED-RMF) the measurements as function of $Q^2_{\rm CCQE}$, being the ED-RMF prediction closer to data in the bin that excludes forward muon angles, i.e. $-0.65 < \cos\theta_l < 0.8$. In the case of the cross section as function of $E_\nu^{\rm cal}$, all the models overpredict the data in the tail of the distribution (large $E_\nu^{\rm cal}$-values). Given that a good

description of $E_\nu^{\rm cal}$ requires a description of the fully exclusive final state (including very low momentum hadrons below detection threshold), the poor agreement is unsurprising.

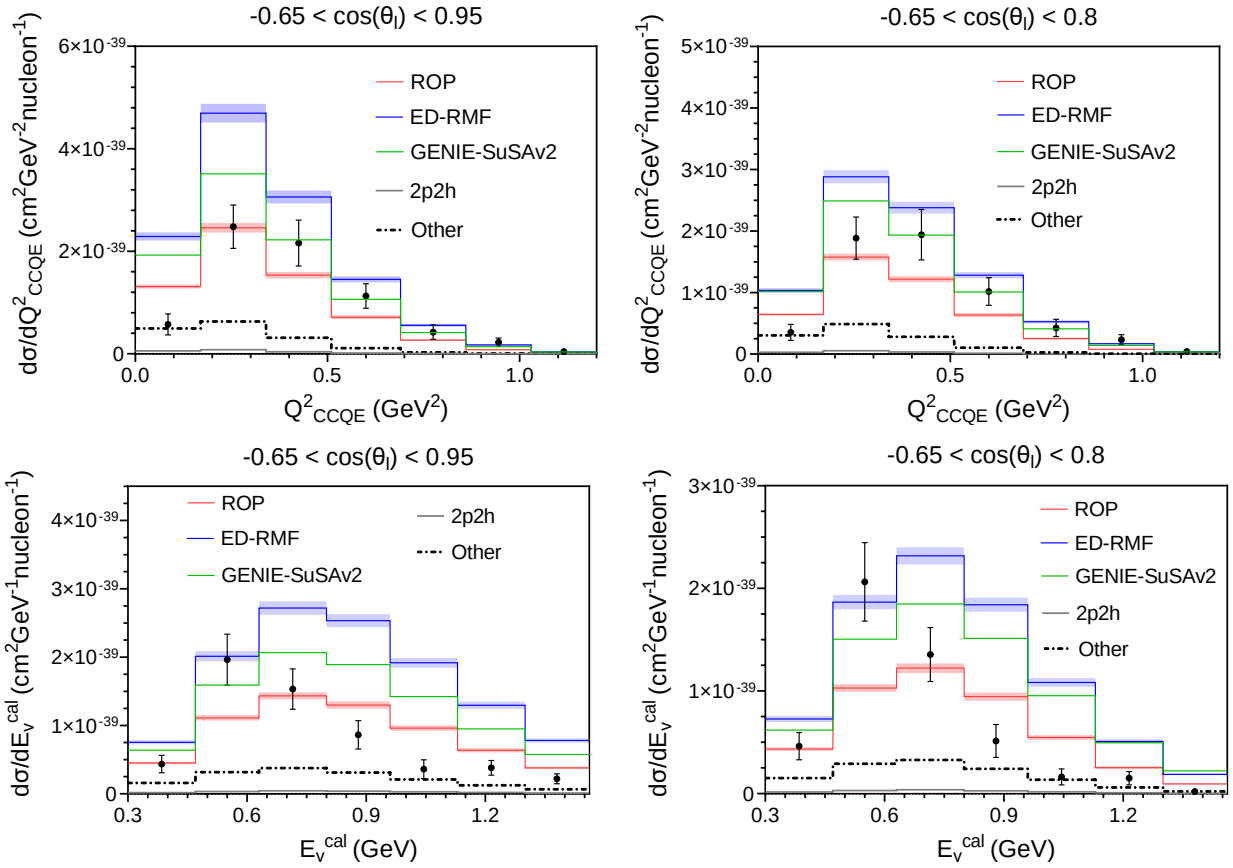

Figure 5·15: MicroBooNE 1μCC0π1p semi-inclusive $\nu_\mu - {}^{40}$Ar cross sections as function of $Q^2_{\rm CCQE}$ and $E_\nu^{\rm cal}$. All curves include the 2p2h and pion absorption (denoted "other") contributions evaluated using GENIE (shown separately). Experimental results are from [118]. The bands, drawn for the ED-RMF and ROP models, represent the uncertainties associated with the modeling of the initial nuclear state. The covariance matrix is not available for the cross section as function of these variable, therefore it is not possible to calculate the χ^2 values.

Chapter 6

Summary and conclusions

The discovery of neutrino oscillations opened a new frontier in particle physics. Past, ongoing, and forthcoming experiments are dedicated to unraveling the mechanisms responsible for neutrino oscillations by measuring the physical parameters governing this phenomenon. As for now, the neutrino mass hierarchy remains unknown, yet it is an important physical information. Additionally, neutrino oscillations have hinted at the existence of charge-parity violation within the lepton sector. To determine the presence of such violation, a fundamental parameter of the PMNS paradigm needs to be measured. Presently, accelerator-based neutrino experiments are actively gathering data, while new experiments are in development, all geared towards quantifying the degree of CP violation present in neutrino oscillations. One of the main limiting systematic errors in neutrino oscillation physics comes from our limited knowledge of neutrino-nucleus interactions. To help to constrain nuclear effects for the modeling of neutrino-nucleus interactions and improve the reconstruction of the neutrino energy for oscillation experiments, in this thesis we have studied semi-inclusive neutrino interactions with complex nuclei at intermediate lepton energies, $i.e.$, neutrino beam energies ranging from 0.5 up to 10 GeV. Due to the kinematics of the particles involved and the complexity of the interaction, we have developed a fully relativistic and quantum mechanical model able to describe not only inclusive but also semi-inclusive electron and neutrino reactions with complex nuclei.

Although there are multiple neutrino-nucleus interaction mechanisms, the focus of this

thesis has been the description of quasielastic scattering of an incoming neutrino by nuclei and the detection in coincidence of a lepton and an ejected proton, also known as one-proton knockout process. The study of this process can be used, with the right selection of experimental observables, to identify relevant nuclear effects related to both the initial state dynamics and to final-state interactions (FSI), as well as to the influence of two-particle-two-hole excitations. After describing the general kinematics of the reaction, we have provided the expressions of the flux-averaged sixth-differential CC neutrino-nucleus cross sections in the plane-wave impulse approximation (PWIA) for different nuclear models, namely the relativistic Fermi gas (RFG), the independent-particle shell model (IPSM), the natural orbitals (NO) shell model and the spectral function model (SF). The results in PWIA show that RFG, the simplest approach considered, differs completely from the two shell-based models, IPSM and NO. Not only the shape of the semi-inclusive cross section is totally different, without any sub-shell structure, but also its magnitude and behavior with the kinematic variables, particularly, with the azimuthal angle of the outgoing nucleon ϕ_N^L. On the contrary, IPSM and NO lead to rather similar results showing only some discrepancies in the low missing momentum region because of the different wave-functions used to construct the momentum distributions.

Aiming to give a state-of-the-art description of the quasielastic contribution of the one-proton knockout process, we have included FSI using the relativistic distorted-wave impulse approximation (RDWIA) framework. Additionally, for the description of the initial nuclear state, we have used the relativistic mean field (RMF) model extended to include effects beyond the mean-field approximation, like the depletion of the occupation of the shell-model states and the appearance of nucleons at higher missing-energies due to nucleon-nucleon correlations, using the SF model as reference. Within RDWIA, two different approaches to describe FSI were discussed: on one hand, the relativistic optical potential (ROP) model which uses complex phenomenological potentials fitted to reproduce elastic proton-nucleus

scattering data; and on the other hand, an extension of the RMF model called energy-dependent relativistic mean field (ED-RMF) model that preserves orthogonality for small values of the proton momentum and improves the agreement with inclusive electron and neutrino scattering data.

The RDWIA approach was used to generate theoretical predictions to compare with experimental semi-inclusive measurements performed by T2K, MINERνA and MicroBooNE collaborations using ^{12}C and ^{40}Ar nuclei as targets. In the specific case of MicroBooNE, the cross-section measurements were collected using both ν_μ and ν_e beams. Although the quasielastic scattering is the dominant contribution in the energy range that has been studied, additional contributions beyond the quasielastic need to be included to compare with the cross-section measurements. These contributions, the two-particle-two-hole (2p2h) and pion production and reabsorption, have been included based on the predictions of GENIE neutrino event generator. Additionally, the quasielastic predictions from the inclusive model SuSAv2 implemented in GENIE were also included in the comparison with the data.

Overall, we have seen that the predictions based on the RDWIA approach match or improve the agreement of the GENIE-SuSAv2 model with the ^{12}C semi-inclusive data measured by T2K and MINERνA collaborations. In particular, the microscopic calculation based on the ED-RMF model improves the agreement with the experimental results at forward lepton angles, i.e. low momentum and energy transfer, where scaling violations and low-energy effects not included in the SuSAv2 model are relevant.

The detection in coincidence of two particles in the final state, a lepton and the ejected proton, opens the possibility of extracting cross sections as function of variables that measure correlations between both detected particles. These can help to explore better different nuclear effects like initial-state physics, FSI or 2p2h. For instance, the transverse kinematic imbalance (TKI) δp_T is particularly sensitive to the model used for the initial nuclear state, therefore realistic models of the nuclei, like the RMF model, are needed in order to describe

correctly this distribution. The tails of the distributions as function of δp_T as well as the inferred variable $|\Delta p|$, exclusively measured by T2K, can help to explore the size and shape of the 2p2h contribution. The $|\Delta p|$ distribution is especially interesting for forward muon scattering angles because of the clear differences between the high and low muon momentum cases, with the former enhancing the relative 2p2h contribution over the latter. It is important to point out the limitations in the predictive power for nucleon kinematics of the implementation of the SuSAv2 2p2h model within GENIE, as well as of the pion absorption contribution, that are included in all the comparisons with experimental data presented in this thesis. It is shown that different models of the 2p2h channel can yield very different semi-inclusive cross-section predictions for this channel, therefore the impact of the factorization approximation used to generate semi-inclusive predictions from inclusive models implemented in GENIE, or any other neutrino event generator that uses the same approximations, and the inconsistencies introduced by using different nuclear models need to be studied carefully.

In addition to the ^{12}C cross sections, we have also analyzed the semi-inclusive $\nu_\mu-^{40}$Ar and ν_e-^{40}Ar cross section data measured by the MicroBooNE collaboration. We have constructed a SF model for neutrons on argon based on RMF results, phenomenology and exclusive $(e, e'p)$ measurements. Also, the RDWIA calculation is performed taking into account conservative uncertainties associated with the modeling of the SF used for the description of the initial state. Among the two RDWIA approaches considered in this work, the ROP model provides the best overall agreement with data for both CC0πNp and CC0π1p topologies, although the former presents large uncertainties. It is worth mentioning in the CC0π1p case the accordance between the ROP predictions and data as function of the muon and proton kinematics, except for the forward muon scattering angles where the reported very low data point appears not to be present in subsequent analyses.

Finally, there are ongoing efforts from different experimental collaborations to improve

the measurements of more neutrino-nucleus exclusive channels, like the one-proton knockout process. For example, the upgraded version of the T2K near detector ND280 with improved reconstruction capabilities will be able to detect protons with much lower momentum, hence we can expect much more precise measurements of interactions with proton production that will require models able to predict hadrons kinematics like the RDWIA. Also, the majority of the neutrino event generators simulate FSI using semi-classical cascade models. However, recent studies suggest that this framework only provides reliable predictions for nucleons with momentum above 200 MeV, while the optical potential approach produces more sensible results. This could justify investigating in the future how to implement in neutrino event generators more exclusive models and more sophisticated descriptions of the initial state that go beyond a simple Fermi gas, which would improve the treatment of semi-inclusive reactions by neutrino event generators.

Appendix A

Single nucleon hadronic tensor in PWIA

In this appendix a detailed derivation of the single-nucleon hadronic tensor in PWIA is presented. Since the main difference between the RPWIA and PWIA is the inclusion of both positive- and negative-energy Dirac spinors, the positive-energy projector involving the free Dirac spinor $u(\mathbf{p}, s)$ can be used in the initial and final nucleon states to obtain

$$4m_N^2 \mathcal{W}^{\mu\nu} = Tr\left[\left(\not{P}_N + m_N\right) \hat{J}_N^{\mu} \left(\not{\overline{P}} + m_N\right) \overline{\hat{J}_N^{\nu}}\right], \tag{A.1}$$

where $P_N^{\mu} = (E_N, \mathbf{p_N})$ and $\overline{P}^{\mu} = \left(\overline{E}, \overline{\mathbf{p}}\right)$ are on-shell 4-momentum corresponding to the final and initial nucleons, respectively, and $\hat{J}_N^{\mu}$ is the weak nucleon current operator. As discussed in several works[59, 127, 128], the choice of the vector part of the current operator $\hat{J}_N^{\mu} = \hat{J}^{\mu}$ is to some extent arbitrary because of the off-shell character of the bound nucleons. This affects the specific form of the current operator that includes also the dependence with the (off-shell) nucleon structure given through its form factors. In what follows we simplify this complex problem by restricting ourselves to the two usual prescriptions for the vector current [127],

$$\begin{aligned} \left[\hat{J}^{\mu}\right]_{\mathrm{CC2}} &= F_1 \gamma^{\mu} + \frac{iF_2}{2m_N} \sigma^{\mu\nu} Q_{\nu} \\ \left[\hat{J}^{\mu}\right]_{\mathrm{CC1}} &= \left(F_1 + F_2\right) \gamma^{\mu} - \frac{F_2}{2m_N} \left(\overline{P} + P_N\right)^{\mu}, \end{aligned} \tag{A.2}$$

with F_1 and F_2 the isovector nucleon form factors, $2\sigma^{\mu\nu} = i\left[\gamma^\mu, \gamma^\nu\right]$ and Q_ν the 4-momentum transferred. The current operator CC1 can be obtained from the CC2 operator by replacing Q_ν with $\overline{Q}_\nu = \left(P_N - \overline{P}\right)_\nu$ and using the Gordon decomposition, *i.e.* assuming that the initial and final nucleons satisfy the free Dirac equation, where one fulfills the identity

$$\overline{u}(p_N) i\sigma^{\mu\nu}(P_N - \overline{P})_\nu u(\overline{p}) = \overline{u}(p_N)\left[2m_N\gamma^\mu - (P_N + \overline{P})^\mu\right] u(\overline{p}). \tag{A.3}$$

Notice that in the case of the initial nucleon being bound in the target nucleus, the two prescriptions give different nuclear responses while in the case of plane waves they are completely equivalent. Let us consider the case of the CC2 weak single-nucleon hadronic current given by

$$\hat{J}^\mu = \left(F_1\gamma^\mu + \frac{iF_2}{2m_N}\sigma^{\mu\alpha}Q_\alpha + G_A\gamma^\mu\gamma^5 + \frac{G_P}{2m_N}\gamma^5 Q^\mu\right), \tag{A.4}$$

with the isovector nucleon form factors given by [129]. A dipole form with cut-off mass $M_A = 1.05$ GeV is assumed for the axial form factor (G_A), while the pseudoscalar form factor (G_P) can be related to the axial form factor assuming a pion-pole dominance and using the partial conservation of the axial current [130]. Inserting the expression of the CC2 single-nucleon hadronic current in (A.1) gives the following single nucleon hadronic tensor

$$\begin{aligned} 4m_N^2\mathcal{W}^{\mu\nu} = Tr\Bigg[&\left(\not{P}_N + m_N\right)\left(F_1\gamma^\mu + \frac{iF_2}{2m_N}\sigma^{\mu\alpha}Q_\alpha + G_A\gamma^\mu\gamma^5 + \frac{G_P}{2m_N}\gamma^5 Q^\mu\right) \\ &\left(\overline{\not{P}} + m_N\right)\left(F_1\gamma^\nu - \frac{iF_2}{2m_N}\sigma^{\nu\beta}Q_\beta + G_A\gamma^\nu\gamma^5 - \frac{G_P}{2m_N}\gamma^5 Q^\nu\right)\Bigg], \end{aligned} \tag{A.5}$$

where we have used the relations $\overline{\gamma^5} = \gamma^0{\gamma^5}^+\gamma^0 = -\gamma^5$, $\overline{\gamma^\mu} = \gamma^\mu$ and $\overline{\sigma^{\mu\nu}} = \sigma^{\mu\nu}$. Eq. (A.5) can be divided in three different contributions: vector-vector $\mathcal{W}^{\mu\nu}_{VV}$, axial-axial $\mathcal{W}^{\mu\nu}_{AA}$ and vector-axial $\mathcal{W}^{\mu\nu}_{VA}$, depending on which specific components of the weak hadronic current are used to build the tensor. In what follows the detailed calculation step by step of the full

single hadronic tensor for the CC2 current is presented. Starting with the vector-vector part

$$4m_N^2\mathcal{W}_{VV}^{\mu\nu} = Tr\left[\left(\not{P}_N + m_N\right)\left(F_1\gamma^\mu + \frac{iF_2}{2m_N}\sigma^{\mu\alpha}Q_\alpha\right)\left(\not{\overline{P}} + m_N\right)\left(F_1\gamma^\nu - \frac{iF_2}{2m_N}\sigma^{\nu\beta}Q_\beta\right)\right]$$

and knowing that $\sigma^{\mu\nu} = i\left(\gamma^\mu\gamma^\nu - g^{\mu\nu}\right)$, then

$$4m_N^2\mathcal{W}_{VV}^{\mu\nu} = \underbrace{Tr\left[\left(\not{P}_N + m_N\right)\left(F_1\gamma^\mu - \frac{F_2}{2m_N}\left(\gamma^\mu\gamma^\alpha Q_\alpha - Q^\mu\right)\right)\left(\not{\overline{P}} + m_N\right)F_1\gamma^\nu\right]}_{A^{\mu\nu}} +$$

$$\underbrace{Tr\left[\left(\not{P}_N + m_N\right)\left(F_1\gamma^\mu - \frac{F_2}{2m_N}\left(\gamma^\mu\gamma^\alpha Q_\alpha - Q^\mu\right)\right)\left(\not{\overline{P}} + m_N\right)\frac{F_2}{2m_N}\left(\gamma^\nu\gamma^\beta Q_\beta - Q^\nu\right)\right]}_{B^{\mu\nu}}.$$

Taking into account that $Tr\left(\gamma^a\gamma^b\right) = 4g^{ab}$, $Tr\left(\gamma^a\gamma^b\gamma^c\gamma^d\right) = 4\left(g^{ab}g^{cd} - g^{ac}g^{bd} + g^{ad}g^{bc}\right)$, $Tr\left(g^{ab}\right) = Tr\left(\mathbb{1}_4\right)g^{ab} = 4g^{ab}$ and that the trace of an odd number of gamma matrices is zero, then

$$A^{\mu\nu} = F_1^2 Tr\Big(\left(\not{P}_N + m_N\right)\gamma^\mu\left(\not{\overline{P}} + m_N\right)\gamma^\nu\Big) - \frac{F_1F_2}{2m_N}Tr\Big(\left(\not{P}_N + m_N\right)\left(\gamma^\mu\gamma^\alpha Q_\alpha - Q^\mu\right)$$
$$\left(\not{\overline{P}} + m_N\right)\gamma^\nu\Big) = 4F_1^2\Big(\left[m_N^2 - P_N\cdot\overline{P}\right]g^{\mu\nu} + P_N^\mu\overline{P}^\nu + P_N^\nu\overline{P}^\mu\Big) + 2F_1F_2\Big(\cancel{Q^\mu\left(P_N + \overline{P}\right)^\nu}$$
$$- \overline{Q}^\mu Q^\nu - \cancel{Q^\mu\left(P_N + \overline{P}\right)^\nu} + \overline{Q}\cdot Q g^{\mu\nu}\Big)$$

and

$$B^{\mu\nu} = \underbrace{\frac{F_1F_2}{2m_N}Tr\left[\left(\not{P}_N + m_N\right)\gamma^\mu\left(\not{\overline{P}} + m_N\right)\left(\gamma^\nu\gamma^\beta Q_\beta - Q^\nu\right)\right]}_{B_1^{\mu\nu}} -$$

$$\underbrace{\frac{F_2^2}{4m_N^2}Tr\left[\left(\not{P}_N + m_N\right)\left(\gamma^\mu\gamma^\alpha Q_\alpha - Q^\mu\right)\left(\not{\overline{P}} + m_N\right)\left(\gamma^\nu\gamma^\beta Q_\beta - Q^\nu\right)\right]}_{B_2^{\mu\nu}}.$$

Expanding both terms, one finds that

$$B_1^{\mu\nu} = \frac{F_1 F_2}{2m_N}\Big[m_N\, Tr\left(\not{P}_N\gamma^\mu\gamma^\nu\not{Q}\right) - m_N\, Tr\left(\not{\overline{P}}\gamma^\mu\right)Q^\nu - m_N\, Tr\left(\not{P}_N\gamma^\mu\right)Q^\nu +$$
$$m_N\, Tr\left(\gamma^\mu\not{\overline{P}}\gamma^\nu\not{Q}\right)\Big] = 2F_1F_2\Big[\cancel{P_N^\mu Q^\nu} - Q^\mu P_N^\nu + P_N\cdot Q g^{\mu\nu} - \cancel{\overline{P}^\mu Q^\nu} - \cancel{P_N^\mu Q^\nu} + \cancel{\overline{P}^\mu Q^\nu}$$
$$- \overline{P}\cdot Q g^{\mu\nu} + Q^\mu\overline{P}^\nu\Big] = 2F_1F_2\left(\overline{Q}\cdot Q g^{\mu\nu} - Q^\mu\overline{Q}^\nu\right)$$

and

$$B_2^{\mu\nu} = \underbrace{\frac{F_2^2}{4m_N^2}\Big[Tr\big[\left(\not{P}_N + m_N\right)\left(\gamma^\mu\not{Q} - Q^\mu\right)\left(\not{\overline{P}} + m_N\right)\gamma^\nu\not{Q}\big]}_{C^{\mu\nu}}$$
$$\underbrace{- Tr\big[\left(\not{P}_N + m_N\right)\left(\gamma^\mu\not{Q} - Q^\mu\right)\left(\not{\overline{P}} + m_N\right)Q^\nu\big]\Big]}_{D^{\mu\nu}}.$$

Since the trace of a 6-γ product can be expressed as 4-γ products as follows $Tr\left(\gamma^\kappa\gamma^\lambda\gamma^\mu\gamma^\nu\gamma^\rho\gamma^\sigma\right) = g^{\kappa\lambda}\times Tr\left(\gamma^\mu\gamma^\nu\gamma^\rho\gamma^\sigma\right) - g^{\kappa\mu}\times Tr\left(\gamma^\lambda\gamma^\nu\gamma^\rho\gamma^\sigma\right) + g^{\kappa\nu}\times Tr\left(\gamma^\lambda\gamma^\mu\gamma^\rho\gamma^\sigma\right) - g^{\kappa\rho}\times Tr\left(\gamma^\lambda\gamma^\mu\gamma^\nu\gamma^\sigma\right) + g^{\kappa\sigma}\times Tr\left(\gamma^\lambda\gamma^\mu\gamma^\nu\gamma^\rho\right)$, we have

$$C^{\mu\nu} = Tr\left[\not{P}_N\gamma^\mu\not{Q}\left(\not{\overline{P}} + \cancel{m_N}\right)\gamma^\nu\not{Q}\right] + m_N^2\, Tr\left[\gamma^\mu\not{Q}\gamma^\nu\not{Q}\right] - Tr\left[\left(\not{P}_N + m_N\right)Q^\mu\left(\not{\overline{P}} + m_N\right)\gamma^\nu\not{Q}\right]$$
$$= 4\Big[P_N^\mu\left(\cancel{Q\cdot\overline{P}Q^\nu} - \cancel{Q\cdot\overline{P}Q^\nu} + Q^2\overline{P}^\nu\right) - P_N\cdot Q\left(\overline{P}^\mu Q^\nu - \overline{P}\cdot Q g^{\mu\nu} + Q^\mu\overline{P}^\nu\right) + P_N\cdot\overline{P}\big(2Q^\mu Q^\nu$$
$$- Q^2 g^{\mu\nu}\big) - P_N^\nu\left(Q^\mu\overline{P}\cdot Q - \overline{P}^\mu Q^2 + Q^\mu\overline{P}\cdot Q\right) + P_N\cdot Q\left(Q^\mu\overline{P}^\nu - \overline{P}^\mu Q^\nu + \overline{P}\cdot Q g^{\mu\nu}\right) + m_N^2$$
$$\left(2Q^\mu Q^\nu - Q^2 g^{\mu\nu}\right) - \left(P_N\cdot\overline{P}Q^\mu Q^\nu - Q^\mu P_N^\nu\overline{P}\cdot Q + Q^\mu\overline{P}^\nu P_N\cdot Q + m_N^2 Q^\mu Q^\nu\right)\Big]$$

and

$$D^{\mu\nu} = Tr\left(\not{P}_N\gamma^\mu\not{Q}\not{\overline{P}}\right)Q^\nu - Tr\left(\not{P}_N\not{\overline{P}}\right)Q^\mu Q^\nu + m_N^2\,Tr\left(\gamma^\mu\not{Q}\right)Q^\nu - m_N^2\,Tr\left(\mathbb{1}_{4x4}\right)Q^\mu Q^\nu = 4\Big[$$
$$- P_N\cdot Q\overline{P}^\mu Q^\nu + P_N^\mu Q^\nu\overline{P}\cdot Q + \cancel{P_N\cdot\overline{P}Q^\mu Q^\nu} - \cancel{P_N\cdot\overline{P}Q^\mu Q^\nu} + \cancel{m_N^2 Q^\mu Q^\nu} - \cancel{m_N^2 Q^\mu Q^\nu}\Big].$$

Using that $\overline{Q}^2 = \left(P_N - \overline{P}\right)^2 = 2m_N^2 - 2P_N\cdot\overline{P}$, then the vector-vector component of the CC2 single-nucleon hadronic tensor can be reduced to

$$\begin{aligned} m_N^2\mathcal{W}_{VV}^{\mu\nu} = {} & F_1^2\left(\overline{P}^\mu P_N^\nu + \overline{P}^\nu P_N^\mu + \frac{\overline{Q}^2}{2}g^{\mu\nu}\right) + F_1F_2\left(Q\cdot\overline{Q}g^{\mu\nu} - \frac{Q^\mu\overline{Q}^\nu + Q^\nu\overline{Q}^\mu}{2}\right) \\ & + \frac{F_2^2}{4m_N^2}\Big[P_N\cdot Q(\overline{P}^\mu Q^\nu + \overline{P}^\nu Q^\mu) + \overline{P}\cdot Q(P_N^\mu Q^\nu + P_N^\nu Q^\mu) - Q^2(P_N^\nu\overline{P}^\mu \\ & + P_N^\mu\overline{P}^\nu) - \left(2m_N^2 - \frac{\overline{Q}^2}{2}\right)Q^\mu Q^\nu + g^{\mu\nu}\left(2m_N^2Q^2 - \frac{Q^2\overline{Q}^2}{2} - 2(P_N\cdot Q)(\overline{P}\cdot Q)\right)\Big]. \end{aligned} \tag{A.6}$$

Following with the axial-axial part of the tensor we have

$$4m_N^2\mathcal{W}_{AA}^{\mu\nu} = Tr\left[\left(\not{P}_N + m_N\right)\left(G_A\gamma^\mu\gamma^5 + \frac{G_P}{2m_N}\gamma^5 Q^\mu\right)\left(\not{\overline{P}} + m_N\right)\left(G_A\gamma^\nu\gamma^5 - \frac{G_P}{2m_N}\gamma^5 Q^\nu\right)\right].$$

Since γ^5 anti-commutes with γ^μ and $(\gamma^5)^2 = \mathbb{1}_4$

$$\begin{aligned} 4m_N^2\mathcal{W}_{AA}^{\mu\nu} = {} & -G_A^2\,Tr\left[\left(\not{P}_N + m_N\right)\gamma^\mu\left(-\not{\overline{P}} + m_N\right)\gamma^\nu\right] - \frac{G_AG_P}{2m_N}\Big(Tr\big[\left(\not{P}_N + m_N\right)\gamma^\mu \\ & \left(-\not{\overline{P}} + m_N\right)Q^\nu\big] + Tr\big[\left(\not{P}_N + m_N\right)Q^\mu\left(-\not{\overline{P}} + m_N\right)\gamma^\nu\big]\Big) - \frac{G_P^2}{4m_N^2}Tr\Big[\left(\not{P}_N + m_N\right)Q^\mu \\ & \left(-\not{\overline{P}} + m_N\right)Q^\nu\Big], \end{aligned}$$

which is reduced to

$$m_N^2 \mathcal{W}_{AA}^{\mu\nu} = G_A^2 \left[P_N^\mu \overline{P}^\nu + P_N^\nu \overline{P}^\mu - g^{\mu\nu} \left(2m_N^2 - \frac{\overline{Q}^2}{2} \right) \right] - \frac{G_P^2 \overline{Q}^2}{8m_N^2} Q^\mu Q^\nu - \frac{G_A G_P}{2} \left(\overline{Q}^\mu Q^\nu + \overline{Q}^\nu Q^\mu \right). \tag{A.7}$$

Finally, the vector-axial component of the hadronic tensor is

$$4m_N^2 \mathcal{W}_{VA}^{\mu\nu} = \underbrace{Tr\left[\left(\not{P}_N + m_N \right) \left(F_1 \gamma^\mu + \frac{iF_2}{2m_N} \sigma^{\mu\alpha} Q_\alpha \right) \left(\overline{\not{P}} + m_N \right) \left(G_A \gamma^\nu \gamma^5 - \frac{G_P}{2m_N} \gamma^5 Q^\nu \right) \right]}_{A^{\mu\nu}} +$$

$$\underbrace{Tr\left[\left(\not{P}_N + m_N \right) \left(G_A \gamma^\mu \gamma^5 + \frac{G_P}{2m_N} \gamma^5 Q^\mu \right) \left(\overline{\not{P}} + m_N \right) \left(F_1 \gamma^\nu - \frac{iF_2}{2m_N} \sigma^{\nu\beta} Q_\beta \right) \right]}_{B^{\mu\nu}},$$

with the first term further divided into

$$A^{\mu\nu} = F_1 \underbrace{Tr\left[\left(\not{P}_N + m_N \right) \gamma^\mu \left(\overline{\not{P}} + m_N \right) \left(G_A \gamma^\nu \gamma^5 - \frac{G_P}{2m_N} \gamma^5 Q^\nu \right) \right]}_{A_1^{\mu\nu}} +$$

$$\frac{iF_2}{2m_N} \underbrace{Tr\left[\left(\not{P}_N + m_N \right) \sigma^{\mu\alpha} Q_\alpha \left(\overline{\not{P}} + m_N \right) \left(G_A \gamma^\nu \gamma^5 - \frac{G_P}{2m_N} \gamma^5 Q^\nu \right) \right]}_{A_2^{\mu\nu}}.$$

Knowing that $Tr\left(\gamma^5 \gamma^\kappa \gamma^\lambda \gamma^\mu \gamma^\nu\right) = -4i\epsilon^{\kappa\lambda\mu\nu}$, where $\epsilon^{\kappa\lambda\mu\nu}$ is the totally antisymmetric rank - 4 Levi-Civita tensor, $Tr\left(\gamma^5 \gamma^\mu \gamma^\nu\right) = 0$ and that the trace of γ^5 multiplied by any odd number of γ^μ matrices is zero, then to the $A_1^{\mu\nu}$ term defined above only contributes one trace $Tr\left(\not{P}_N \gamma^\mu \overline{\not{P}} \gamma^\nu \gamma^5\right)$ proportional to G_A and $A_2^{\mu\nu}$ is given by

$$A_2^{\mu\nu} = i \left[m_N G_A \left(Tr\left(\not{P}_N \gamma^\mu \gamma^\alpha \gamma^\nu \gamma^5 \right) + Tr\left(\gamma^\mu \gamma^\alpha \overline{\not{P}} \gamma^\nu \gamma^5 \right) \right) - \frac{G_P}{2m_N} Tr\left(\gamma^5 \not{P}_N \gamma^\mu \gamma^\alpha \overline{\not{P}} \right) Q^\nu \right] Q_\alpha,$$

where we have used that $\sigma^{\mu\alpha} = i\left(\gamma^{\mu}\gamma^{\alpha} - g^{\mu\nu}\right)$ to reduce the number of traces that are not zero. Then we have that

$$A^{\mu\nu} = -4i\left[F_1 G_A \epsilon^{\alpha\mu\beta\nu} P_{N\alpha}\overline{P}_{\beta} + \frac{F_2}{2m_N}\left(-G_A m_N \epsilon^{\mu\nu\alpha\beta}\left(\overline{P} + P_N\right)_{\beta} + \frac{G_P}{2m_N}\epsilon^{\beta\mu\alpha\sigma} P_{N\beta}\overline{P}_{\sigma} Q^{\nu}\right) Q_{\alpha}\right].$$

Equivalently, the $B^{\mu\nu}$ term is given by

$$B^{\mu\nu} = -4i\left[F_1 G_A \epsilon^{\alpha\mu\beta\nu} P_{N\alpha}\overline{P}_{\beta} + \frac{F_2}{2m_N}\left(-G_A m_N \epsilon^{\mu\nu\alpha\beta}\left(\overline{P} + P_N\right)_{\beta} - \frac{G_P}{2m_N}\epsilon^{\beta\nu\alpha\sigma} P_{N\beta}\overline{P}_{\sigma} Q^{\mu}\right) Q_{\alpha}\right].$$

Therefore, the final expression of the vector-axial component of the CC2 hadronic tensor is

$$m_N^2 \mathcal{W}_{VA}^{\mu\nu} = i\left[G_A \epsilon^{\mu\nu\alpha\beta}\left(2F_1 P_{N\alpha}\overline{P}_{\beta} - F_2\left(P_N + \overline{P}\right)_{\alpha}\right) + \frac{G_P F_2}{4m_N^2}\left(-Q^{\mu}\epsilon^{\nu\alpha\beta\sigma} + Q^{\nu}\epsilon^{\mu\alpha\beta\sigma}\right) P_{N\alpha}\overline{P}_{\sigma}\right] Q_{\beta}. \tag{A.8}$$

For completeness, we also present here the expression of the single nucleon hadronic tensor calculated using the CC1 current. Following a similar procedure to the one used above for CC2, for the CC1 case the vector-vector and vector-axial components of the hadronic tensor are given by

$$\begin{aligned} m_N^2 \mathcal{W}_{VV}^{\mu\nu} =& \left(F_1 + F_2\right)^2\left(\overline{P}^{\mu} P_N^{\nu} + \overline{P}^{\nu} P_N^{\mu} + \frac{\bar{Q}^2}{2} g^{\mu\nu}\right) \\ &- \left[F_2\left(F_1 + F_2\right) - \frac{F_2^2}{2}\left(1 - \frac{\overline{Q}^2}{4m_N^2}\right)\right]\left(\overline{P} + P_N\right)^{\mu}\left(\overline{P} + P_N\right)^{\nu} \end{aligned} \tag{A.9}$$

and

$$m_N^2 \mathcal{W}_{VA}^{\mu\nu} = 2iG_A\left(F_1 + F_2\right)\epsilon^{\alpha\beta\mu\nu} P_{N\alpha}\overline{P}_{\beta}. \tag{A.10}$$

Appendix B

Single nucleon responses in PWIA

As in the case of exclusive $(e, e'p)$ scattering in PWIA [59, 131, 132], the semi-inclusive neutrino-nucleus cross section in PWIA can be reduced to the neutrino-nucleon cross section times a spectral function, describing the probability of finding a nucleon in the target nucleus with certain energy and momentum which should be compatible with the kinematics of the process. This factorization property is broken in general when FSI effects or other ingredients beyond the impulse approximation are introduced. Moreover, even in RPWIA, *i.e.*, the plane-wave approach but the bound nucleons wave functions are the full relativistic solutions of the Dirac equation in presence of potentials (positive and negative energy components included), factorization is lost. In general, the elementary neutrino-nucleon cross section is proportional to the contraction of the leptonic $L_{\mu\nu}$ and the hadronic $\mathcal{W}^{\mu\nu}$ tensors. In Appendix A we have obtained in detail the single nucleon hadronic tensor under PWIA for both CC1 and CC2 prescriptions of the weak nucleon current. The weak leptonic current for CC processes is defined as $J^l_\mu = \overline{u_l}\left(k', s'\right)\left(\gamma_\mu - \chi\gamma_\mu\gamma^5\right) u_{\nu_l}\left(k, s\right)$, where u_l and u_{ν_l} are the free Dirac spinors that describe the final lepton and the initial neutrino and $\chi = 1(-1)$ corresponds to neutrino (antineutrino) processes. The leptonic tensor constructed from this current reads,

$$L_{\mu\nu} = K_\mu K'_\nu + K_\nu K'_\mu - K \cdot K' g_{\mu\nu} - i\chi\epsilon_{\mu\nu\alpha\beta}K^\alpha K'^\beta\,, \tag{B.1}$$

with K_μ and K'_μ the 4-momenta of the neutrino and the final lepton. Defining a coordinate system where the three momentum $\mathbf{q}$ is along the z-axis (see Fig. B·1), then the 4-momenta of the initial and final nucleons and leptons can be expressed as

$$\begin{aligned}
P_N^\mu &= (E_N, p_N \sin\theta_N \cos\phi_N, p_N \sin\theta_N \sin\phi_N, p_N \cos\theta_N)\,, \\
\overline{P}^\mu &= \left(\overline{E}, p_N \sin\theta_N \cos\phi_N, p_N \sin\theta_N \sin\phi_N, p_N \cos\theta_N - q\right)\,, \\
K_\mu &= \left(k, \frac{-kk' \sin\theta_l}{q}, 0, -\frac{k(k - k'\cos\theta_l)}{q}\right), \\
K'_\mu &= \left(E_l, -\frac{kk' \sin\theta_l}{q}, 0, \frac{k'(k' - k\cos\theta_l)}{q}\right).
\end{aligned} \tag{B.2}$$

Also, the transferred 4-momenta take trivial forms in this coordinate system: $Q^\mu = (\omega, 0, 0, q)$ and $\overline{Q}^\mu = (\overline{\omega}, 0, 0, q)$, with $\overline{\omega} = E_N - \overline{E}$. The main advantage of using this coordinate system with the momentum transfer fixed on the z-axis is the possibility of expressing the contraction of the leptonic and hadronic tensors as the linear combination of 10 nuclear response functions, defined as specific components of the hadronic tensor, and factorizing the ϕ_N dependence, which is simply reduced to $\cos\phi_N$ or $\cos 2\phi_N$ terms. The contraction of

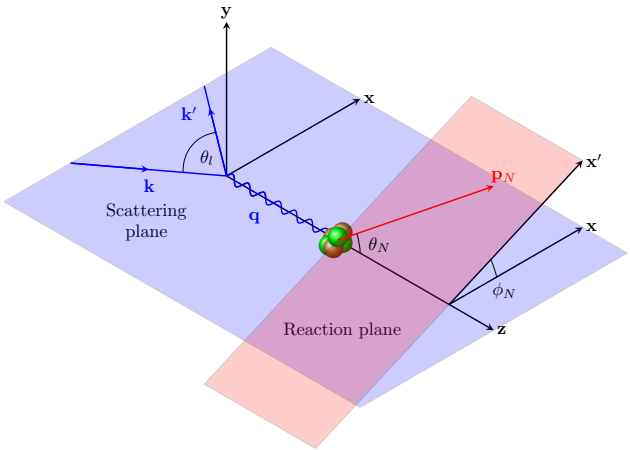

Figure B·1: Definition of the coordinate system where the momentum transfer q lies on the z-axis. Notice that the leptons are contained in the x-z plane (scattering plane) and the plane containing the ejected nucleon with momentum p_N and polar angle θ_N forms an angle ϕ_N with the scattering plane.

the hadronic and leptonic tensors, a Lorentz invariant that has the same value in any system of reference, can be expressed as [49]

$$\begin{aligned}\mathcal{F}_{\chi}^{2} = \frac{2}{\upsilon_0} L_{\mu\nu}\mathcal{W}^{\mu\nu} &= V_{CC}(R_{VV}^{CC} + R_{AA}^{CC}) + 2V_{CL}(R_{VV}^{CL} + R_{AA}^{CL}) + V_{LL}(R_{VV}^{LL} + R_{AA}^{LL}) \\ &+ V_{T}(R_{VV}^{T} + R_{AA}^{T}) + V_{TT}(R_{VV}^{TT} + R_{AA}^{TT})\cos 2\phi_N + V_{TC}(R_{VV}^{TC} + R_{AA}^{TC})\cos\phi_N \\ &+ V_{TL}(R_{VV}^{TL} + R_{AA}^{TL})\cos\phi_N + \chi\left(V_{T'}R_{VA}^{T'} + V_{TC'}R_{VA}^{TC'}\cos\phi_N + V_{TL'}R_{VA}^{TL'}\cos\phi_N\right), \end{aligned} \tag{B.3}$$

where $\upsilon_0 = (k + E_l)^2 - q^2$. The different weak hadronic responses are given by specific components of the single nucleon hadronic tensor $\mathcal{W}^{\mu\nu}$

$$\begin{aligned} R^{CC} &= \mathcal{W}^{00}, \\ R^{CL} &= \mathcal{W}^{03}, \\ R^{LL} &= \mathcal{W}^{33}, \\ R^{T} &= \mathcal{W}^{11} + \mathcal{W}^{22}, \\ R^{TT} &= \mathcal{W}^{22} - \mathcal{W}^{11}, \\ R^{TC} &= 2\sqrt{2}\mathcal{W}^{01}, \\ R^{TL} &= 2\sqrt{2}\mathcal{W}^{31}, \\ R^{T'} &= 2i\mathcal{W}^{12}, \\ R^{TC'} &= 2\sqrt{2}i\mathcal{W}^{02}, \\ R^{TL'} &= 2\sqrt{2}i\mathcal{W}^{32}, \end{aligned} \tag{B.4}$$

and the leptonic factors are specific components of the leptonic tensor given in Eq. (B.1)

$$
\begin{aligned}
V_{CC} &= \frac{2}{\upsilon_0} L_{00}, \\
V_{CL} &= \frac{2}{\upsilon_0} L_{03}, \\
V_{LL} &= \frac{2}{\upsilon_0} L_{33}, \\
V_{T} &= \frac{L_{11} + L_{22}}{\upsilon_0}, \\
V_{TT} &= \frac{L_{22} - L_{11}}{\upsilon_0}, \\
V_{TC} &= \frac{2}{\sqrt{2}\upsilon_0} L_{01}, \\
V_{TL} &= \frac{2}{\sqrt{2}\upsilon_0} L_{31}, \\
V_{T'} &= -\frac{2i}{\upsilon_0} L_{12}, \\
V_{TC'} &= -\frac{2i}{\sqrt{2}\upsilon_0} L_{02}, \\
V_{TL'} &= -\frac{2i}{\sqrt{2}\upsilon_0} L_{32}.
\end{aligned}
\tag{B.5}
$$

Notice that due to momentum conservation $\mathbf{q} = \mathbf{p}_N - \overline{\mathbf{p}}$ the x and y components of the 3-momenta of the initial and ejected nucleon are equal because $\mathbf{q}$ only has z component. Exploiting this, we can derive the ϕ_N dependence of the invariant $\mathcal{F}_\chi^2$ as follows: the responses that contain both 0 and 3 indices (R^{CC}, R^{CL} and R^{LL}) cannot have ϕ_N dependence because they depend on the first and last components of the 4-momenta (the energy and the projection on the z-axis) that do not have any ϕ_N dependence. The response that has both 1 and 2 indices, *i.e.* $R^{T'}$, is calculated only with the vector-axial component of the hadronic tensor. As it can be seen in Eq. (A.8) and Eq. (A.10), this response is proportional to $\epsilon^{12\alpha\beta} P_{N\alpha} \overline{P}_\beta$ or $\epsilon^{12\alpha\beta} \left(P_N + \overline{P}\right)_\alpha Q_\beta$ for both CC1 and CC2 currents, which again involve components of the 4-momenta that are ϕ_N-independent. The R^T response is constructed by the sum of the 11 and 22 components of the hadronic tensor and the

only dependence on ϕ_N is introduced by terms proportional to $\overline{P}^1 P_N^1 + \overline{P}^2 P_N^2$, or using Eq. (B.2), proportional to $p_N^2 \sin^2\theta_N \left(\cos^2\phi_N + \sin^2\phi_N\right) = p_N^2 \sin^2\theta_N$, hence R^T does not present any ϕ_N dependence. The same argument can be used for $R^{TT} = \mathcal{W}^{22} - \mathcal{W}^{11}$, where the difference, instead of the sum as in the previous case, leads the response to be proportional to $p_N^2 \sin^2\theta_N \left(\cos^2\phi_N - \sin^2\phi_N\right) = p_N^2 \sin^2\theta_N \cos 2\phi_N$. The terms that do not contain this angular dependence are zero or are eliminated when the subtraction is performed. The responses R^{TC} and R^{TL} have ϕ_N dependence introduced by terms proportional to P_N^1 or $\overline{P}^1$ thus, they are proportional to $p_N \sin\theta_N \cos\phi_N$. Finally, for the $R^{TC'}$ and $R^{TL'}$ responses only the terms proportional to $p_N \sin\theta_N \cos\phi_N$ survive, with the cross terms that depend on $\cos\phi_N \sin\phi_N$ eliminated due to the antisymmetry properties of the Levi-Civita tensor.

Although we have used the special properties found by considering a coordinate system with direction of q fixed in the z-axis, from the point of view of an accelerator-based neutrino experiment it is common to have fixed the direction of the incoming neutrino k instead. This coordinate system, presented in Fig. 2·3 and used to generate cross sections that can be directly compared with experimental measurements, can be related with the one with fixed direction of q, shown in Fig. B·1, by a rotation in the scattering plane of an angle

$$\cos\theta_q = \frac{k - k'\cos\theta_l}{q}, \tag{B.6}$$

which is the angle between $\mathbf{q}$ and $\mathbf{k}$. The angular variables identifying the ejected nucleon in both coordinate systems can be related using the following expressions

$$\cos\theta_N = \cos\theta_N^L \cos\theta_q - \cos\phi_N^L \sin\theta_N^L \sin\theta_q\,, \tag{B.7}$$

$$\sin\theta_N = \sqrt{1 - \cos^2\theta_N}\,, \tag{B.8}$$

$$\cos\phi_N = \frac{\cos\phi_N^L \sin\theta_N^L \cos\theta_q + \cos\theta_N^L \sin\theta_q}{\sin\theta_N}\,, \tag{B.9}$$

$$\sin\phi_N = \frac{\sin\phi_N^L \sin\theta_N^L}{\sin\theta_N}\,. \tag{B.10}$$

To conclude, since we already found out the complete expression of the single nucleon hadronic current in Appendix A, in what follows we present the exact analytic expressions, for the CC2 current, of all the hadronic and leptonic responses calculated as defined in Eq. (B.4) and Eq. (B.5). Since we have already derived the entire ϕ_N dependence of the invariant, the 4-momenta defined in Eq. (B.2) will be evaluated at $\phi_N = 0$ to simplify the calculations. Taking into account the following definitions

$$\begin{aligned} p_\perp &= p_N \sin\theta_N \,, \\ p_\parallel &= p_N \cos\theta_N - q \,, \\ \delta &= E_N - \overline{E} - \omega \,, \end{aligned} \tag{B.11}$$

and that the relevant Lorentz invariants are

$$\begin{aligned} \overline{P}\cdot Q &= -\frac{Q^2}{2} - \frac{\delta^2}{2} - \delta(\overline{E}+\omega) \,, \\ P_N \cdot Q &= \frac{Q^2}{2} - \frac{\delta^2}{2} - \delta\overline{E} \,, \\ \overline{Q}^2 &= Q^2 + \delta^2 + 2\omega\delta \,, \end{aligned} \tag{B.12}$$

the single nucleon hadronic responses are

$$\begin{aligned} 8m_N^4 R_{VV}^{CC} &= 4\overline{E}^2(4F_1^2 m_N^2 + F_2^2|Q^2|) + 4\overline{E}\omega(4F_1^2 m_N^2 + F_2^2|Q^2|) - 4F_1^2 m_N^2|Q^2| \\ &- 8F_1F_2 m_N^2(\omega^2 + |Q^2|) + F_2^2(\omega^2|Q^2| - 4m_N^2(\omega^2 + |Q^2|)) \\ &- 2\delta(2\overline{E}+\omega)(F_2^2(2\overline{E}\omega + \omega^2 - |Q^2|) - 4F_1^2 m_N^2) + \delta^2(-4F_2^2\overline{E}^2 \\ &- 12F_2^2\omega\overline{E} + 4F_1^2 m_N^2 + F_2^2(|Q^2| - 5\omega^2)) - 4\delta^3 F_2^2(\overline{E}+\omega) - \delta^4 F_2^2 \,, \end{aligned} \tag{B.13}$$

$$
\begin{aligned}
8m_N^4 R_{AA}^{CC} = {} & 16\overline{E}^2 G_A^2 m_N^2 + 16\overline{E} G_A^2 m_N^2 \omega - 8 G_A G_P \omega^2 m_N^2 \\
& - 4G_A^2 m_N^2 (4m_N^2 + |Q^2|) + G_P^2 \omega^2 |Q^2| + \delta(16\overline{E} G_A^2 m_N^2 \\
& + 8G_A^2 m_N^2 \omega - 8 G_A G_P m_N^2 \omega - 2G_P^2 \omega^3) + \delta^2 (4G_A^2 m_N^2 - G_P^2 \omega^2)\,,
\end{aligned} \tag{B.14}
$$

$$
\begin{aligned}
8m_N^4 R_{VV}^{CL} = {} & 2\overline{E}(2p_\parallel + q)(4F_1^2 m_N^2 + F_2^2 |Q^2|) + \omega(8F_1^2 m_N^2 p_\parallel \\
& - 8F_1 F_2 q m_N^2 + F_2^2(-4m_N^2 q + 2p_\parallel |Q^2| + q|Q^2|)) \\
& + \delta\Bigg(F_2^2 \left[-(4\overline{E}^2 q + \overline{E}\omega(4p_\parallel + 6q) + 2\omega^2(p_\parallel + q) - |Q^2|(2p_\parallel + q)) \right] \\
& + 8F_1^2 m_N^2 p_\parallel - 4F_1 F_2 q m_N^2 \Bigg) - \delta^2 F_2^2 (4\overline{E} q + 2\omega p_\parallel + 3\omega q) - \delta^3 F_2^2 q\,,
\end{aligned} \tag{B.15}
$$

$$
\begin{aligned}
8m_N^4 R_{AA}^{CL} = {} & 8\overline{E} G_A^2 m_N^2 (2p_\parallel + q) + \omega(8G_A^2 m_N^2 p_\parallel - 8G_A G_P q m_N^2 + G_P^2 q |Q^2|) \\
& + \delta(8G_A^2 m_N^2 p_\parallel - 4G_A G_P m_N^2 q - 2G_P^2 \omega^2 q) - \delta^2 G_P^2 \omega q\,,
\end{aligned} \tag{B.16}
$$

$$
\begin{aligned}
8m_N^4 R_{VV}^{LL} = {} & F_1^2(16m_N^2 p_\parallel(p_\parallel + q) + 4m_N^2 |Q^2|) - 8F_1 F_2 m_N^2 \omega^2 + F_2^2 \big[4p_\parallel q(\omega(\overline{E} + \omega) \\
& - q(p_\parallel + q)) + |Q^2|((2p_\parallel + q)^2 + 4m_N^2 - |Q^2| + 2\overline{E}\omega) - 4m_N^2 q^2 \big] \\
& + \delta\omega(-8F_1^2 m_N^2 - 8F_1 F_2 m_N^2 + F_2^2 \left[2q(2p_\parallel + q) - 4\omega^2 - 8\omega\overline{E} - 4\overline{E}^2 \right]) \\
& - \delta^2(4F_1^2 m_N^2 + F_2^2 \left[6\omega(\overline{E} + \omega) - \omega^2 \right]) - 2F_2^2 \delta^3 \omega\,,
\end{aligned} \tag{B.17}
$$

$$
\begin{aligned}
8m_N^4 R_{AA}^{LL} = {} & G_A^2(16m_N^2 p_\parallel(p_\parallel + q) + 16m_N^4 + 4m_N^2 |Q^2|) + G_P^2 q^2 |Q^2| - \delta(2G_P^2 q^2 \omega \\
& + G_A^2 8m_N^2 \omega) - \delta^2(4G_A^2 m_N^2 + G_P^2 q^2) - 8m_N^2 G_A G_P q^2\,,
\end{aligned} \tag{B.18}
$$

$$8m_N^4 R_{VV}^T = 16F_1F_2m_N^2|Q^2| + 4F_2^2(2m_N^2 + p_\perp^2)|Q^2| + 8F_1^2m_N^2(2p_\perp^2 + |Q^2|) - 16\delta F_1(F_1+F_2)m_N^2\omega + \delta^2(8F_2^2\overline{E}^2 + 8F_2^2\omega\overline{E} - 8F_1^2m_N^2 - 2F_2^2|Q^2|) + 4\delta^3F_2^2(2\overline{E}+\omega) + 2\delta^4F_2^2\,, \tag{B.19}$$

$$8m_N^4 R_{AA}^T = 8G_A^2m_N^2(4m_N^2 + 2p_\perp^2 + |Q^2|) - 16\delta G_A^2m_N^2\omega - 8\delta^2G_A^2m_N^2\,, \tag{B.20}$$

$$8m_N^4 R_{VV}^{TT} = -4p_\perp^2(4F_1^2m_N^2 + F_2^2|Q^2|)\,, \tag{B.21}$$

$$8m_N^4 R_{AA}^{TT} = -16G_A^2m_N^2p_\perp^2\,, \tag{B.22}$$

$$8m_N^4 R_{VV}^{TC} = 4\sqrt{2}p_\perp(2\overline{E}+\omega)(4F_1^2m_N^2 + F_2^2|Q^2|) + 4\sqrt{2}\delta p_\perp(F_2^2(-2\overline{E}\omega - \omega^2 + |Q^2|) + 4F_1^2m_N^2) - 4\delta^2\sqrt{2}F_2^2\omega p_\perp\,, \tag{B.23}$$

$$8m_N^4 R_{AA}^{TC} = 16\sqrt{2}G_A^2m_N^2p_\perp(2\overline{E}+\omega) + 16\sqrt{2}\delta G_A^2m_N^2p_\perp\,, \tag{B.24}$$

$$8m_N^4 R_{VV}^{TL} = 4\sqrt{2}p_\perp(2p_\parallel + q)(4F_1^2m_N^2 + F_2^2|Q^2|) - 4\sqrt{2}\delta F_2^2p_\perp q(2\overline{E}+\omega) - 4\sqrt{2}\delta^2F_2^2p_\perp q\,, \tag{B.25}$$

$$8m_N^4 R_{AA}^{TL} = 16\sqrt{2}G_A^2m_N^2p_\perp(2p_\parallel + q)\,, \tag{B.26}$$

$$8m_N^4 R_{VA}^{T'} = -32G_A m_N^2(F_1+F_2)(\omega p_\parallel - \overline{E}q) - 16\delta G_A m_N^2(2F_1 p_\parallel - F_2 q)\,, \tag{B.27}$$

$$8m_N^4 R_{VA}^{TC'} = 32\sqrt{2}G_A m_N^2 p_\perp q(F_1+F_2) + 4\sqrt{2}\delta F_2 G_P \omega p_\perp q\,, \tag{B.28}$$

$$8m_N^4 R_{VA}^{TL'} = 32\sqrt{2}G_A p_\perp \omega m_N^2(F_1+F_2) + 4\sqrt{2}p_\perp \delta(8G_A F_1 m_N^2 + G_P F_2 q^2)\,, \tag{B.29}$$

and the leptonic responses are

$$V_{CC} = 1 - \frac{\Delta_1}{\upsilon_0}, \tag{B.30}$$

$$V_{CL} = -\frac{1}{q}\left(\omega + \frac{\Delta_4 \kappa}{\upsilon_0}\right), \tag{B.31}$$

$$V_{LL} = \frac{\omega^2}{q^2} + \frac{\Delta_1}{\upsilon_0} + \frac{\Delta_4^2}{\upsilon_0 q^2} + \frac{2\Delta_4 \kappa \omega}{q^2 \upsilon_0}, \tag{B.32}$$

$$V_T = |Q^2|\left(\frac{1}{2q^2} + \frac{1}{\upsilon_0}\right) + \Delta_1\left(\frac{1}{2q^2} + \frac{1}{\upsilon_0}\right) - \frac{\Delta_1^2 - \Delta_3 + \Delta_1|Q^2|}{2\upsilon_0 q^2}, \tag{B.33}$$

$$V_{TT} = -\left[\frac{\Delta_1 + |Q^2|}{2q^2}\left(1 - \frac{\Delta_1}{\upsilon_0}\right) + \frac{\Delta_3}{2q^2\upsilon_0}\right], \tag{B.34}$$

$$V_{TC} = -\frac{1}{\sqrt{2}\upsilon_0}\sqrt{1 + \frac{\upsilon_0}{q^2}}\sqrt{\Delta_3 + (\Delta_1 + |Q^2|)(\upsilon_0 - \Delta_1)}, \tag{B.35}$$

$$V_{TL} = \frac{1}{\sqrt{2}q^2 v_0}\sqrt{\Delta_3 + (\Delta_1 + |Q^2|)(v_0 - \Delta_1)}(\Delta_4 + \omega\kappa), \tag{B.36}$$

$$V_{T'} = \frac{1}{v_0}\left(|Q^2|\sqrt{1 + \frac{v_0}{q^2}} - \frac{\Delta_4\omega}{q}\right), \tag{B.37}$$

$$V_{TC'} = -\frac{1}{\sqrt{2}v_0}\sqrt{\Delta_3 + (\Delta_1 + |Q^2|)(v_0 - \Delta_1)}, \tag{B.38}$$

$$V_{TL'} = \frac{\omega}{\sqrt{2}qv_0}\sqrt{\Delta_3 + (\Delta_1 + |Q^2|)(v_0 - \Delta_1)}, \tag{B.39}$$

with

$$\begin{aligned}
\Delta_1 &= m_\nu^2 + m_l^2 = m_l^2, \\
\Delta_2 &= 2kE_l - 2kk', \\
\Delta_3 &= 4k^2k'^2 - 4k^2E_l^2, \\
\Delta_4 &= m_l^2 - m_v^2 = m_l^2, \\
\kappa &= k + E_l, \\
v_0 &= (k + E_l)^2 - q^2 = \Delta_2 + \Delta_1 + 4kk'\cos^2\frac{\theta_l}{2}.
\end{aligned} \tag{B.40}$$

Appendix C

Relativistic description of the nucleus: the Relativistic Mean Field model

The relativistic mean field (RMF) model of finite nuclei [61, 62, 63] is derived from a relativistic Lagrangian that contains mesonic and nucleonic degrees of freedom. Because of the relatively high values of the coupling constants, the relativistic quantum field theory of finite nuclei cannot be treated using perturbation theory. The mean field approximation, which gives the correct solution of the field equations for high values of the nuclear density, turns out to be a reasonable approximation for a phenomenological description of nuclei where the parameters of the theory are adjusted to reproduce properties of the many-body system of nuclear matter and finite nuclei rather than adjusted to nucleon-nucleon scattering data. Compared with non-relativistic models of nuclei, for example the non-relativistic shell model, the RMF approach starts on a more fundamental level, including explicitly the mesonic degrees of freedom, and naturally includes relativistic effects, such as two types of potentials (scalar and vector), a strong spin-orbit term, and saturation of nuclear matter due to the difference between the scalar and vector densities.

Under the approximations of the RMF theory, the nucleons are considered to be point-like particles characterized by Dirac spinors ψ. The nucleons inside a nucleus can interact by exchanging effective point-like particles called mesons ϕ_m. The mesons are characterized by their quantum numbers, their mass m_m, and by coupling constants g_m. In a phenomenological theory the number of these mesons, which is minimized to keep the theory simple, their

quantum numbers, such as spin (J), isospin (T) and parity (P), the values of their masses and coupling constants are fitted to reproduce as well as possible the experimental data. One could use the mesons detected in free space by different experiments (π, ω, ρ, etc) to take advantage of their known properties, however the parameters of the mesons within the nuclear medium do not necessarily have the same values as in free space. Within the theory, the exchange of a phenomenological scalar $\sigma-$meson with quantum numbers $J = 0$, $T = 0$ and $P = +1$ leads to an attractive force between nucleons, while the repulsive part of the interaction is generated by the exchange of a vector $\omega-$meson with quantum numbers $J = 1$, $T = 0$ and $P = -1$. Additionally, the isospin dependence of the strong force is introduced by the exchange of $\rho-$mesons with quantum numbers $J = 1$, $T = 1$ and $P = -1$. The classical RMF Lagrangian density is given by

$$\mathcal{L} = \mathcal{L}_N + \mathcal{L}_m + \mathcal{L}_A + \mathcal{L}_{\text{int}}, \tag{C.1}$$

which is the sum of the free nucleons Lagrangian density

$$\mathcal{L}_N = \overline{\psi} \left(i\gamma^\mu \partial_\mu - m \right) \psi, \tag{C.2}$$

the Lagrangian for the free mesons

$$\mathcal{L}_m = \frac{1}{2} \left(\partial_\mu \sigma \partial^\mu \sigma - m_\sigma^2 \sigma^2 \right) - \frac{1}{2} \left(\Omega_{\mu\nu} \Omega^{\mu\nu} - \frac{1}{2} m_\omega^2 \omega_\mu \omega^\mu \right) - \frac{1}{2} \left(\mathbf{R}_{\mu\nu} \mathbf{R}^{\mu\nu} - \frac{1}{2} m_\rho^2 \boldsymbol{\rho}_\mu \boldsymbol{\rho}^\mu \right), \tag{C.3}$$

where bold indicate tensors in isospin space and the field tensors of the $\omega-$ and ρ-meson are

$$\Omega^{\mu\nu} = \partial^\mu \omega^\nu - \partial^\nu \omega^\mu,$$
$$\mathbf{R}^{\mu\nu} = \partial^\mu \boldsymbol{\rho}^\nu - \partial^\nu \boldsymbol{\rho}^\mu,$$

the Lagrangian associated to the photon field A

$$\mathcal{L}_A = -\frac{1}{2} F_{\mu\nu} F^{\mu\nu}, \tag{C.4}$$

with the electromagnetic field tensor $F_{\mu\nu} = \partial_\mu A_\nu - \partial_\nu A_\mu$, and finally the part of the Lagrangian that gives the interaction between the nucleons, the mesons and the photon

$$\mathcal{L}_{\text{int}} = -g_\sigma \overline{\psi}\sigma\psi - g_\omega \overline{\psi}\gamma_\mu \omega^\mu \psi - g_\rho \overline{\psi}\gamma_\mu \boldsymbol{\tau}\boldsymbol{\rho}^\mu \psi - e\overline{\psi}\gamma_\mu \frac{\mathbb{1}+\tau_3}{2} A^\mu \psi - U(\sigma), \tag{C.5}$$

where all the terms are linear except $U(\sigma) = \frac{1}{3} g_2 \sigma^3 + \frac{1}{4} g_3 \sigma^4$ that is necessary in order to reproduce correctly surface properties of finite nuclei.

In the mean field approximation, *i.e.* in the classic limit where the mesons masses and coupling constants are fitted to experimental data, the Euler-Lagrange equations of motion for the Lagrangian density defined in Eq. (C.1) yield

$$\begin{aligned}
\left\{ \gamma_\mu \big(i\partial^\mu + g_\omega \omega^\mu + g_\rho \boldsymbol{\tau}\boldsymbol{\rho}^\mu + e\frac{\mathbb{1}+\tau_3}{2} A^\mu \big) + m + g_\sigma \sigma \right\} \psi_i &= 0, \\
(\Box + m_\sigma)\, \sigma &= -g_\sigma \rho_s - g_2 \sigma^2 - g_3 \sigma^3, \\
(\Box + m_\omega)\, \omega^\mu &= g_\omega J^\mu, \\
(\Box + m_\rho)\, \boldsymbol{\rho}^\mu &= g_\rho \mathbf{J}^\mu, \\
\Box A^\mu &= e J_e^\mu,
\end{aligned} \tag{C.6}$$

where the index i runs up to the number of nucleons A, the currents are defined as

$$\begin{aligned} J^{\mu}(x) &= \sum_{i=1}^{A} \overline{\psi}_i(x)\gamma^{\mu}\psi_i(x), \\ \boldsymbol{J}^{\mu}(x) &= \sum_{i=1}^{A} \overline{\psi}_i(x)\gamma^{\mu}\boldsymbol{\tau}\psi_i(x), \\ J_e^{\mu}(x) &= \sum_{i=1}^{A} \overline{\psi}_i\frac{\mathbb{1}+\tau_3}{2}\gamma^{\mu}\psi_i(x), \end{aligned} \tag{C.7}$$

and the scalar density given by

$$\rho_s(x) = \sum_{i=1}^{A} \overline{\psi}_i(x)\psi_i(x). \tag{C.8}$$

In the static limit where the meson fields are considered time-independent and the time dependence of the spinors ψ_i is given by $\exp(i\epsilon_i t)$, the isotropic stationary RMF equations are reduced to

$$\begin{aligned} \Big\{ -i\boldsymbol{\alpha}\boldsymbol{\nabla} + \beta(m+S) - (\epsilon_i - V)\Big\}\psi_i &= 0, \\ \Big\{ -\nabla + m_{\sigma}\Big\}\sigma &= -g_{\sigma}\rho_s - g_2\sigma^2 - g_3\sigma^3, \\ \Big\{ -\nabla + m_{\omega}\Big\}\omega^0 &= g_{\omega}\rho_v, \\ \Big\{ -\nabla + m_{\rho}\Big\}\rho_3^0 &= g_{\rho}\rho_3, \\ -\nabla\rho_c^0 &= e\rho_c, \end{aligned} \tag{C.9}$$

with the baryon, isovector and charge densities

$$\begin{aligned}\rho_v &= \sum_{i=1}^{A} \psi_i^+ \psi_i \\ \rho_3 &= \sum_{i=1}^{A} \psi_i^+ \tau_3 \psi_i, \\ \rho_c &= \sum_{i=1}^{A} \psi_i^+ \frac{\mathbb{1} + \tau_3}{2} \psi_i. \end{aligned} \tag{C.10}$$

In Eq. (C.9) two radial potentials appear, one called vector potential

$$V(r) = g_\omega \omega^0(r) + g_\rho \tau_3 \rho_3^0(r) + eA^0(r), \tag{C.11}$$

and a scalar potential

$$S(r) = g_\sigma \sigma(r), \tag{C.12}$$

that behaves like a Lorentz scalar and together with the nucleon mass defines an effective Dirac mass

$$m^*(r) = m + S(r). \tag{C.13}$$

The RMF equations presented in Eq. (C.9) are a set of coupled equations where the variables are the nucleon field ψ_i, the mesons fields $\sigma, \omega^0, \rho_3^0$ and the Coulomb field A^0. These equations are solved by iteration: starting from an initial guess for the potentials V and S, one solves the Dirac equation for the nucleon field ψ_i and then this result is used to calculate the densities ρ_s, ρ_v, ρ_3 and ρ_c given in Eq. (C.8) and Eq. (C.10). With these results acting as sources in Eq. (C.9), one can calculate the mesons and the Coulomb fields and a new set of vector C.11 and scalar C.12 potentials can be obtained. The calculation starts again with

the new values of the potentials until it converges. Different sets of the free parameters of the model, the nucleon and mesons masses m, m_σ, m_ω and m_ρ, the coupling constants of the mesons fields, g_σ, g_ω and g_ρ, and the non-linear parameters g_2 and g_3, are summarized in Table C.1 together with some nuclear properties predictions like baryon density ρ_0, binding energy per particle E/A, incompressibility K which is related with the second derivative of E/A evaluated at the saturation density, effective mass m^*/m and asymmetry parameter J which is defined as [61]

$$J = \frac{k_F^2}{6\sqrt{k_F^2 + m^{*2}}} + \frac{1}{3\pi^2}\left(\frac{g_\rho}{m_\rho}\right)^2 k_F^3, \tag{C.14}$$

where k_F is the Fermi momentum.

Table C.1: RMF parameters [61] from different models [133, 134, 135, 136] and predictions of different nuclear properties (see text above) for symmetric nuclear matter.

Parameter	HS	NL1	NL2	NLSH
m (MeV)	939	938	938	939
m_σ (MeV)	520	492.25	504.89	526.059
m_ω (MeV)	783	795.359	780	783
m_ρ (MeV)	770	763	763	763
g_σ	10.47	10.138	9.111	10.444
g_ω	13.8	13.285	11.493	12.945
g_ρ	4.035	4.976	5.507	4.383
g_2 (fm^{-1})	0	-12.172	-2.304	-6.9099
g_3	0	-36.265	13.783	-15.8337
ρ_0 (fm^{-3})	0.148	0.151	0.146	0.146
E/A (MeV)	-15.731	-16.426	-17.018	-16.346
K (MeV)	546.3	211.11	399.2	355.4
m^*/m	0.541	0.573	0.670	0.597
J (MeV)	34.9	43.5	45.1	36.1

Appendix D

T2K χ^2 analysis

Using the covariance matrices provided by the T2K [115] collaboration, we compute the χ^2 between the predictions of the different models considered in this work and the cross section measurements. Within this section we use the unregularised TKI measurements provided by T2K [115], as these are more suitable for quantitative χ^2 analysis. Nevertheless, it was verified that differences in the χ^2 analysis when using the regularised results are marginal. The results are compiled in Table D.1. The large χ^2 with respect to the number of degrees of freedom for all measurements indicates a poor overall agreement, with the exception of ROP's good description of the 1μCC0πNp and TKI measurements. However, the low χ^2 could be driven by poor agreement in a handful of outlying bins (for example, the high muon momentum overflow bins reported by the T2K collaboration in the 1μCC0π0p results or the muon kinematic slices with very small cross section in the IV results). To study this, Fig. D·1 shows the evolution of the χ^2 between each model and the T2K cross-section measurements when the bins contributing the largest χ^2 are progressively removed. The bin contributing the largest χ^2 is identified by re-calculating the χ^2 after removing each bin (and its corresponding rows and columns in the covariance matrix) and choosing the largest one. The bins removed for each model are therefore different.

Fig. D·1 immediately shows that the extreme χ^2-values of all the microscopic models for the $\Delta\theta$ variable are mainly caused by two bins, which indeed are associated to very small values of the cross section (the -360 $< \Delta\theta <$ -5 bin in the first two panels of Fig. 5·5 which

are not entirely shown to improve the readability of the plot). It also shows that the ROP and ED-RMF models are both in good agreement with the 1μCC0π0p results once $\sim$5 of the worst bins are removed, many of which correspond to bins with extreme muon kinematics for most models, and that the difference between models is reduced. Beyond some of the extreme muon kinematic bins, it is interesting to note that large RPWIA χ^2-values are driven mostly by the forward going muon bins, which is not surprising given the strong suppressive effect of FSI in the corresponding low momentum transfer region.

For the 1μCC0πNp and $\delta\phi_T$ results, Fig. D·1 further shows that the preference for ROP is not driven by only outlying bins. Conversely, the ROP preference is reduced for the other TKI by eliminating the lowest $\delta\alpha_T$ bin or the third δp_T bin.

	rROP	ROP	RPWIA	ED-RMF	GENIE-SuSAv2
1μCC0π0p (59)	232	127	1172	180	209
1μCC0πNp (24)	64	28	82	76	69
Δp (49)	666	373	756	773	366
$\Delta\theta$ (35)	1170	466	1285	1379	159
$\Delta\theta^*$ (33)	129	92	152	146	123
$\lvert\Delta\mathbf{p}\rvert$ (49)	348	290	357	376	336
δp_T (8)	38	16	60	41	36
$\delta\alpha_T$ (8)	29	13	41	33	49
$\delta\phi_T$ (8)	23	20	38	24	40

Table D.1: χ^2 values for different T2K topologies and variables. The degrees of freedom are given in brackets in the first column. $\Delta\theta^*$ means that bins 0 and 5 were eliminated (-360 $< \Delta\theta <$ -5 bin in the first two panels of Fig. 5·5 which are not entirely shown to improve the readability of the plot).

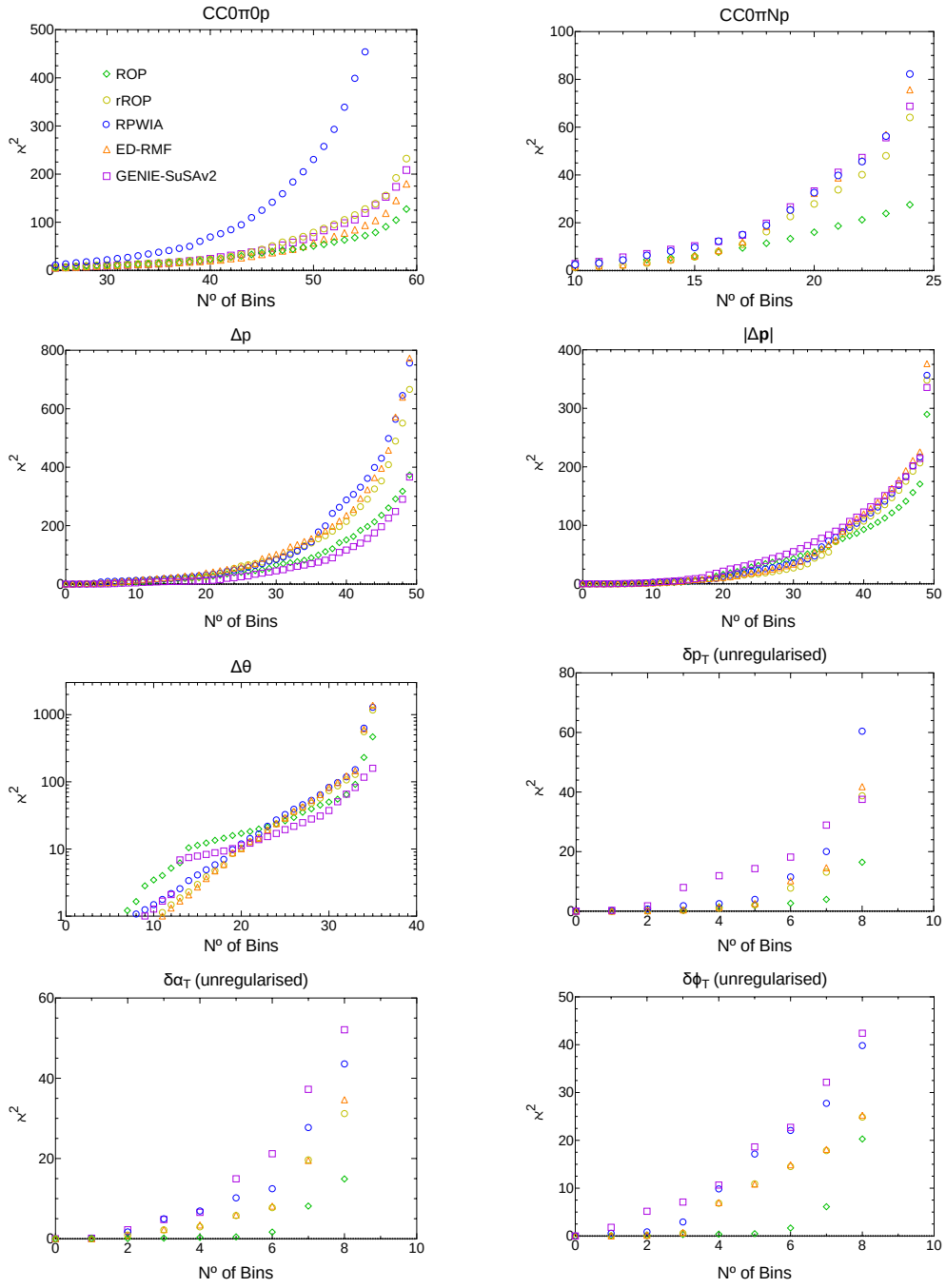

Figure D·1: Evolution of χ^2 between each model and T2K semi-inclusive cross section measurements when the bins contributing the largest χ^2 are progressively removed. For example, the right-most points of the top left plot correspond to the total χ^2 in Table D.1 (calculated using all 58 bins reported by T2K), whilst the points just to the left of them show the χ^2 value once the bin contributing the largest χ^2 is removed. Points further to the left remove more bins following the same rule.

Bibliography

[1] F. Reines and C. L. Cowan. "Detection of the Free Neutrino". In: *Phys. Rev.* 92 (3 Nov. 1953), pp. 830–831. DOI: 10.1103/PhysRev.92.830. URL: https://link.aps.org/doi/10.1103/PhysRev.92.830.

[2] M. Gell-Mann and A. Pais. "Behavior of Neutral Particles under Charge Conjugation". In: *Phys. Rev.* 97 (5 Mar. 1955), pp. 1387–1389. DOI: 10.1103/PhysRev.97.1387. URL: https://link.aps.org/doi/10.1103/PhysRev.97.1387.

[3] B. Pontecorvo. "Neutrino Experiments and the Problem of Conservation of Leptonic Charge". In: *Soviet Journal of Experimental and Theoretical Physics* 26 (May 1968), p. 984.

[4] Y. Fukuda et al. "Measurement of the Flux and Zenith-Angle Distribution of Upward Throughgoing Muons by Super-Kamiokande". In: *Phys. Rev. Lett.* 82 (13 Mar. 1999), pp. 2644–2648. DOI: 10.1103/PhysRevLett.82.2644. URL: https://link.aps.org/doi/10.1103/PhysRevLett.82.2644.

[5] Y. Fukuda et al. "Evidence for Oscillation of Atmospheric Neutrinos". In: *Phys. Rev. Lett.* 81 (8 Aug. 1998), pp. 1562–1567. DOI: 10.1103/PhysRevLett.81.1562. URL: https://link.aps.org/doi/10.1103/PhysRevLett.81.1562.

[6] S. Abe et al. "Search for the Majorana Nature of Neutrinos in the Inverted Mass Ordering Region with KamLAND-Zen". In: *Phys. Rev. Lett.* 130 (5 Jan. 2023), p. 051801. DOI: 10.1103/PhysRevLett.130.051801. URL: https://link.aps.org/doi/10.1103/PhysRevLett.130.051801.

[7] Ivan Esteban et al. "The fate of hints: updated global analysis of three-flavor neutrino oscillations". In: *Journal of High Energy Physics* 2020.9 (Sept. 2020). DOI: 10.1007/jhep09(2020)178. URL: https://doi.org/10.1007%2Fjhep09%282020%29178.

[8] *NuFIT 5.2(2022)*. URL: http://www.nu-fit.org/.

[9] C. Giganti, S. Lavignac, and M. Zito. "Neutrino oscillations: The rise of the PMNS paradigm". In: *Progress in Particle and Nuclear Physics* 98 (2018), pp. 1–54. ISSN: 0146-6410. DOI: https://doi.org/10.1016/j.ppnp.2017.10.001. URL: https://www.sciencedirect.com/science/article/pii/S014664101730087X.

[10] Jiro Arafune, Masafumi Koike, and Joe Sato. "CP violation and matter effect in long baseline neutrino oscillation experiments". In: *Phys. Rev. D* 56 (5 Sept. 1997), pp. 3093–3099. DOI: 10.1103/PhysRevD.56.3093. URL: https://link.aps.org/doi/10.1103/PhysRevD.56.3093.

[11] J. Altegoer et al. "The NOMAD experiment at the CERN SPS". In: *Nuclear Instruments and Methods in Physics Research Section A: Accelerators, Spectrometers, Detectors and Associated Equipment* 404.1 (1998), pp. 96–128. ISSN: 0168-9002. DOI: https://doi.org/10.1016/S0168-9002(97)01079-6. URL: https://www.sciencedirect.com/science/article/pii/S0168900297010796.

[12] P. Astier et al. "Search for $\nu_\mu \to \nu_e$ oscillations in the NOMAD experiment". In: *Physics Letters B* 570.1 (2003), pp. 19–31. ISSN: 0370-2693. DOI: https://doi.org/10.1016/j.physletb.2003.07.029. URL: https://www.sciencedirect.com/science/article/pii/S0370269303010505.

[13] F. Vannucci. "The NOMAD experiment at the CERN". In: *Advances in High Energy Physics* vol 2014.Article ID 129694 (2014), 20 pages. DOI: https://doi.org/10.1155/2014/129694.

[14] M. H. Ahn et al. "Indications of Neutrino Oscillation in a 250 km Long-Baseline Experiment". In: *Phys. Rev. Lett.* 90 (4 Jan. 2003), p. 041801. DOI: 10.1103/PhysRevLett.90.041801. URL: https://link.aps.org/doi/10.1103/PhysRevLett.90.041801.

[15] M. H. Ahn et al. "Measurement of neutrino oscillation by the K2K experiment". In: *Phys. Rev. D* 74 (7 Oct. 2006), p. 072003. DOI: 10.1103/PhysRevD.74.072003. URL: https://link.aps.org/doi/10.1103/PhysRevD.74.072003.

[16] *Artificial Neutrino Beam Detected After Passing Through 250 km of Earth.* URL: https://neutrino.kek.jp/news/990628.1stSK/.

[17] P. Adamson et al. "The NuMI neutrino beam". In: *Nuclear Instruments and Methods in Physics Research Section A: Accelerators, Spectrometers, Detectors and Associated Equipment* 806 (2016), pp. 279–306. ISSN: 0168-9002. DOI: https://doi.org/10.1016/j.nima.2015.08.063. URL: https://www.sciencedirect.com/science/article/pii/S016890021501027X.

[18] D.G. Michael et al. "The magnetized steel and scintillator calorimeters of the MINOS experiment". In: *Nuclear Instruments and Methods in Physics Research Section A: Accelerators, Spectrometers, Detectors and Associated Equipment* 596.2 (2008), pp. 190–228. ISSN: 0168-9002. DOI: https://doi.org/10.1016/j.nima.2008.08.003. URL: https://www.sciencedirect.com/science/article/pii/S0168900208011613.

[19] P. Adamson et al. "Combined Analysis of ν_μ Disappearance and $\nu_\mu \to \nu_e$ Appearance in MINOS Using Accelerator and Atmospheric Neutrinos". In: *Phys. Rev. Lett.* 112 (19 May 2014), p. 191801. DOI: 10.1103/PhysRevLett.112.191801. URL: https://link.aps.org/doi/10.1103/PhysRevLett.112.191801.

[20] M. A. Acero et al. "First measurement of neutrino oscillation parameters using neutrinos and antineutrinos by NOvA". In: *Phys. Rev. Lett.* 123 (15 Oct. 2019), p. 151803. DOI: 10.1103/PhysRevLett.123.151803. URL: https://link.aps.org/doi/10.1103/PhysRevLett.123.151803.

[21] M. A. Acero et al. "Improved measurement of neutrino oscillation parameters by the NOvA experiment". In: *Phys. Rev. D* 106 (3 Aug. 2022), p. 032004. DOI: 10.1103/PhysRevD.106.032004. URL: https://link.aps.org/doi/10.1103/PhysRevD.106.032004.

[22] L. Aliaga et al. "Design, calibration, and performance of the MINERvA detector". In: *Nuclear Instruments and Methods in Physics Research Section A: Accelerators, Spectrometers, Detectors and Associated Equipment* 743 (2014), pp. 130–159. ISSN: 0168-9002. DOI: https://doi.org/10.1016/j.nima.2013.12.053. URL: https://www.sciencedirect.com/science/article/pii/S0168900214000035.

[23] J. Kleykamp et al. *Simultaneous measurement of muon neutrino quasielastic-like cross sections on CH, C, water, Fe, and Pb as a function of muon kinematics at MINERvA*. 2023. arXiv: 2301.02272 [hep-ex].

[24] K. Abe et al. "The T2K experiment". In: *Nuclear Instruments and Methods in Physics Research Section A: Accelerators, Spectrometers, Detectors and Associated Equipment* 659.1 (2011), pp. 106–135. ISSN: 0168-9002. DOI: https://doi.org/10.1016/j.nima.2011.06.067. URL: https://www.sciencedirect.com/science/article/pii/S0168900211011910.

[25] K. Abe et al. "Improved constraints on neutrino mixing from the T2K experiment with 3.13×10^{21} protons on target". In: *Phys. Rev. D* 103 (11 June 2021), p. 112008. DOI: 10.1103/PhysRevD.103.112008. URL: https://link.aps.org/doi/10.1103/PhysRevD.103.112008.

[26] Mathieu Lamoureux and for T2K Collaboration. *Upgrade of the T2K near detector ND280: effect on oscillation and cross-section analysis*. 2018. arXiv: 1803.02645 [physics.ins-det].

[27] Hyper-Kamiokande Proto-Collaboration et al. *Hyper-Kamiokande Design Report*. 2018. arXiv: 1805.04163 [physics.ins-det].

[28] C. Athanassopoulos et al. "Candidate Events in a Search for $\overline{\nu}_\mu \to \overline{\nu}_e$ Oscillations". In: *Phys. Rev. Lett.* 75 (14 Oct. 1995), pp. 2650–2653. DOI: 10.1103/PhysRevLett.75.2650. URL: https://link.aps.org/doi/10.1103/PhysRevLett.75.2650.

[29] A. Aguilar et al. "Evidence for neutrino oscillations from the observation of $\overline{\nu}_e$ appearance in a $\overline{\nu}_\mu$ beam". In: *Phys. Rev. D* 64 (11 Nov. 2001), p. 112007. DOI: 10.1103/PhysRevD.64.112007. URL: https://link.aps.org/doi/10.1103/PhysRevD.64.112007.

[30] A. A. Aguilar-Arevalo et al. "Significant Excess of Electronlike Events in the MiniBooNE Short-Baseline Neutrino Experiment". In: *Phys. Rev. Lett.* 121 (22 Nov. 2018), p. 221801. DOI: 10.1103/PhysRevLett.121.221801. URL: https://link.aps.org/doi/10.1103/PhysRevLett.121.221801.

[31] R. Acciarri et al. *A Proposal for a Three Detector Short-Baseline Neutrino Oscillation Program in the Fermilab Booster Neutrino Beam*. 2015. arXiv: 1503.01520.

[32] DUNE Collaboration et al. *The DUNE Far Detector Interim Design Report Volume 1: Physics, Technology and Strategies*. 2018. arXiv: 1807.10334 [physics.ins-det].

[33] M. Martini, M. Ericson, and G. Chanfray. "Neutrino energy reconstruction problems and neutrino oscillations". In: *Phys. Rev. D* 85 (9 May 2012), p. 093012. DOI: 10.1103/PhysRevD.85.093012. URL: https://link.aps.org/doi/10.1103/PhysRevD.85.093012.

[34] J. Nieves et al. "Neutrino energy reconstruction and the shape of the charged current quasielastic-like total cross section". In: *Phys. Rev. D* 85 (11 June 2012), p. 113008. DOI: 10.1103/PhysRevD.85.113008. URL: https://link.aps.org/doi/10.1103/PhysRevD.85.113008.

[35] A. A. Aguilar-Arevalo et al. "First measurement of the muon neutrino charged current quasielastic double differential cross section". In: *Phys. Rev. D* 81 (9 May 2010), p. 092005. DOI: 10.1103/PhysRevD.81.092005. URL: https://link.aps.org/doi/10.1103/PhysRevD.81.092005.

[36] A. A. Aguilar-Arevalo et al. "First measurement of the muon antineutrino double-differential charged-current quasielastic cross section". In: *Phys. Rev. D* 88 (3 Aug. 2013), p. 032001. DOI: 10.1103/PhysRevD.88.032001. URL: https://link.aps.org/doi/10.1103/PhysRevD.88.032001.

[37] G. M. Radecky et al. "Study of single-pion production by weak charged currents in low-energy νd interactions". In: *Phys. Rev. D* 25 (5 Mar. 1982), pp. 1161–1173. DOI: 10.1103/PhysRevD.25.1161. URL: https://link.aps.org/doi/10.1103/PhysRevD.25.1161.

[38] T. Kitagaki et al. "Study of $\nu d \to \mu^- p p_s$ and $\nu d \to \mu^- \Delta^{++}(1232) n_s$ using the BNL 7-foot deuterium-filled bubble chamber". In: *Phys. Rev. D* 42 (5 Sept. 1990), pp. 1331–1338. DOI: 10.1103/PhysRevD.42.1331. URL: https://link.aps.org/doi/10.1103/PhysRevD.42.1331.

[39] N. J. Baker et al. "Quasielastic neutrino scattering: A measurement of the weak nucleon axial-vector form factor". In: *Phys. Rev. D* 23 (11 June 1981), pp. 2499–2505. DOI: 10.1103/PhysRevD.23.2499. URL: https://link.aps.org/doi/10.1103/PhysRevD.23.2499.

[40] V. Lyubushkin et al. "A study of quasi-elastic muon neutrino and antineutrino scattering in the NOMAD experiment". In: *Eur. Phys. J. C* 63 (Aug. 2009), pp. 355–381. DOI: 10.1140/epjc/s10052-009-1113-0. URL: https://doi.org/10.1140/epjc/s10052-009-1113-0.

[41] M. Martini et al. "Unified approach for nucleon knock-out and coherent and incoherent pion production in neutrino interactions with nuclei". In: *Phys. Rev. C* 80 (6 Dec. 2009), p. 065501. DOI: 10.1103/PhysRevC.80.065501. URL: https://link.aps.org/doi/10.1103/PhysRevC.80.065501.

[42] M. Martini et al. "Neutrino and antineutrino quasielastic interactions with nuclei". In: *Phys. Rev. C* 81 (4 Apr. 2010), p. 045502. DOI: 10.1103/PhysRevC.81.045502. URL: https://link.aps.org/doi/10.1103/PhysRevC.81.045502.

[43] M. Martini, M. Ericson, and G. Chanfray. "Neutrino quasielastic interaction and nuclear dynamics". In: *Phys. Rev. C* 84 (5 Nov. 2011), p. 055502. DOI: 10.1103/PhysRevC.84.055502. URL: https://link.aps.org/doi/10.1103/PhysRevC.84.055502.

[44] J.E. Amaro et al. "Meson-exchange currents and quasielastic neutrino cross sections in the superscaling approximation model". In: *Physics Letters B* 696.1 (2011), pp. 151–155. ISSN: 0370-2693. DOI: https://doi.org/10.1016/j.physletb.2010.12.007. URL: https://www.sciencedirect.com/science/article/pii/S0370269310013547.

[45] J. E. Amaro et al. "Meson-Exchange Currents and Quasielastic Antineutrino Cross Sections in the Superscaling Approximation". In: *Phys. Rev. Lett.* 108 (15 Apr. 2012), p. 152501. DOI: 10.1103/PhysRevLett.108.152501. URL: https://link.aps.org/doi/10.1103/PhysRevLett.108.152501.

[46] J. Nieves, I. Ruiz Simo, and M.J. Vicente Vacas. "The nucleon axial mass and the MiniBooNE quasielastic neutrino–nucleus scattering problem". In: *Physics Letters B* 707.1 (2012), pp. 72–75. ISSN: 0370-2693. DOI: https://doi.org/10.1016/j.physletb.2011.11.061. URL: https://www.sciencedirect.com/science/article/pii/S0370269311014407.

[47] A. M. Ankowski et al. "Comparison of the calorimetric and kinematic methods of neutrino energy reconstruction in disappearance experiments". In: *Phys. Rev. D* 92 (7 Oct. 2015), p. 073014. DOI: 10.1103/PhysRevD.92.073014. URL: https://link.aps.org/doi/10.1103/PhysRevD.92.073014.

[48] S. Dolan et al. "Sensitivity of the upgraded T2K Near Detector to constrain neutrino and antineutrino interactions with no mesons in the final state by exploiting nucleon-lepton correlations". In: *Phys. Rev. D* 105 (3 Feb. 2022), p. 032010. DOI: 10.1103/PhysRevD.105.032010. URL: https://link.aps.org/doi/10.1103/PhysRevD.105.032010.

[49] J. W. Van Orden and T. W. Donnelly. "Nuclear theory and event generators for charge-changing neutrino reactions". In: *Phys. Rev. C* 100 (4 Oct. 2019), p. 044620. DOI: 10.1103/PhysRevC.100.044620. URL: https://link.aps.org/doi/10.1103/PhysRevC.100.044620.

[50] J. M. Franco-Patino et al. "Semi-inclusive charged-current neutrino-nucleus cross sections in the relativistic plane-wave impulse approximation". In: *Phys. Rev. C* 102 (6 Dec. 2020), p. 064626. DOI: 10.1103/PhysRevC.102.064626. URL: https://link.aps.org/doi/10.1103/PhysRevC.102.064626.

[51] J. M. Franco-Patino et al. "Theoretical description of semi-inclusive T2K, MINERνA and MicroBooNE neutrino-nucleus data in the relativistic plane wave impulse approximation". In: *Phys. Rev. D* 104 (7 Oct. 2021), p. 073008. DOI: 10.1103/PhysRevD.104.073008. URL: https://link.aps.org/doi/10.1103/PhysRevD.104.073008.

[52] L. Alvarez-Ruso et al. "NuSTEC White Paper: Status and challenges of neutrino–nucleus scattering". In: *Progress in Particle and Nuclear Physics* 100 (2018), pp. 1–68. ISSN: 0146-6410. DOI: https://doi.org/10.1016/j.ppnp.2018.01.006. URL: https://www.sciencedirect.com/science/article/pii/S0146641018300061.

[53] J E Amaro et al. "Electron- versus neutrino-nucleus scattering". In: *Journal of Physics G: Nuclear and Particle Physics* 47.12 (Nov. 2020), p. 124001. DOI: 10.1088/1361-6471/abb128. URL: https://dx.doi.org/10.1088/1361-6471/abb128.

[54] O. Moreno et al. "Semi-inclusive charged-current neutrino-nucleus reactions". In: *Phys. Rev. D* 90 (1 July 2014), p. 013014. DOI: 10.1103/PhysRevD.90.013014. URL: https://link.aps.org/doi/10.1103/PhysRevD.90.013014.

[55] D B Day et al. "Scaling in Inclusive Electron-Nucleus Scattering". In: *Annual Review of Nuclear and Particle Science* 40.1 (1990), pp. 357–410. DOI: 10.1146/annurev.ns.40.120190.002041. eprint: https://doi.org/10.1146/annurev.ns.40.120190.002041. URL: https://doi.org/10.1146/annurev.ns.40.120190.002041.

[56] T. W. Donnelly and Ingo Sick. "Superscaling of inclusive electron scattering from nuclei". In: *Phys. Rev. C* 60 (6 Nov. 1999), p. 065502. DOI: 10.1103/PhysRevC.60.065502. URL: https://link.aps.org/doi/10.1103/PhysRevC.60.065502.

[57] Omar Benhar. "Electron- and neutrino-nucleus scattering". In: *Nuclear Physics B - Proceedings Supplements* 139 (2005). Proceedings of the Third International Workshop on Neutrino-Nucleus Interactions in the Few-GeV Region, pp. 15–20. ISSN: 0920-5632. DOI: https://doi.org/10.1016/j.nuclphysbps.2004.11.173. URL: https://www.sciencedirect.com/science/article/pii/S0920563204009272.

[58] Omar Benhar et al. "Electron- and neutrino-nucleus scattering in the impulse approximation regime". In: *Phys. Rev. D* 72 (5 Sept. 2005), p. 053005. DOI: 10.1103/PhysRevD.72.053005. URL: https://link.aps.org/doi/10.1103/PhysRevD.72.053005.

[59] J.A. Caballero et al. "Analysis of factorization in (e,e'p) reactions: A survey of the relativistic plane wave impulse approximation". In: *Nuclear Physics A* 632.3 (1998), pp. 323–362. ISSN: 0375-9474. DOI: https://doi.org/10.1016/S0375-9474(97)00817-8. URL: https://www.sciencedirect.com/science/article/pii/S0375947497008178.

[60] R. Cenni, T. W. Donnelly, and A. Molinari. "Relativistic electromagnetic charge response: Finite versus infinite systems, exclusive versus inclusive processes". In: *Phys. Rev. C* 56 (1 July 1997), pp. 276–291. DOI: 10.1103/PhysRevC.56.276. URL: https://link.aps.org/doi/10.1103/PhysRevC.56.276.

[61] P. Ring. "Relativistic mean field theory in finite nuclei". In: *Progress in Particle and Nuclear Physics* 37 (1996), pp. 193–263. ISSN: 0146-6410. DOI: https://doi.org/10.1016/0146-6410(96)00054-3. URL: https://www.sciencedirect.com/science/article/pii/0146641096000543.

[62] J.D Walecka. "A theory of highly condensed matter". In: *Annals of Physics* 83.2 (1974), pp. 491–529. ISSN: 0003-4916. DOI: https://doi.org/10.1016/0003-4916(74)90208-5. URL: https://www.sciencedirect.com/science/article/pii/0003491674902085.

[63] Brian D. Serot and John Dirk Walecka. "Relativistic Nuclear Many-Body Theory". In: *Recent Progress in Many-Body Theories: Volume 3*. Ed. by T. L. Ainsworth et al. Boston, MA: Springer US, 1992, pp. 49–92. ISBN: 978-1-4615-3466-2. DOI: 10.1007/978-1-4615-3466-2_5. URL: https://doi.org/10.1007/978-1-4615-3466-2_5.

[64] A. N. Antonov et al. "Scaling function, spectral function, and nucleon momentum distribution in nuclei". In: *Phys. Rev. C* 83 (4 Apr. 2011), p. 045504. DOI: 10.1103/PhysRevC.83.045504. URL: https://link.aps.org/doi/10.1103/PhysRevC.83.045504.

[65] J. A. Caballero et al. "Scaling function and nucleon momentum distribution". In: *Phys. Rev. C* 81 (5 May 2010), p. 055502. DOI: 10.1103/PhysRevC.81.055502. URL: https://link.aps.org/doi/10.1103/PhysRevC.81.055502.

[66] Per-Olov Löwdin. "Quantum Theory of Many-Particle Systems. I. Physical Interpretations by Means of Density Matrices, Natural Spin-Orbitals, and Convergence Problems in the Method of Configurational Interaction". In: *Phys. Rev.* 97 (6 Mar. 1955), pp. 1474–1489. DOI: 10.1103/PhysRev.97.1474. URL: https://link.aps.org/doi/10.1103/PhysRev.97.1474.

[67] M. V. Ivanov et al. "Charged-current quasielastic neutrino scattering cross sections on ^{12}C with realistic spectral and scaling functions". In: *Phys. Rev. C* 89 (1 Jan. 2014), p. 014607. DOI: 10.1103/PhysRevC.89.014607. URL: https://link.aps.org/doi/10.1103/PhysRevC.89.014607.

[68] O. Benhar et al. "Spectral function of finite nuclei and scattering of GeV electrons". In: *Nuclear Physics A* 579.3 (1994), pp. 493–517. ISSN: 0375-9474. DOI: https://doi.org/10.1016/0375-9474(94)90920-2. URL: https://www.sciencedirect.com/science/article/pii/0375947494909202.

[69] S. Turck-Chièze. "Present status of (ee'p) experiments". In: *From Collective States to Quarks in Nuclei*. Ed. by Hartmuth Arenhövel and Anna Maria Saruis. Berlin, Heidelberg: Springer Berlin Heidelberg, 1981, pp. 251–257. ISBN: 978-3-540-38539-4.

[70] J. M. Udías et al. "Spectroscopic factors in ^{40}Ca and ^{208}Pb from (e,e'p): Fully relativistic analysis". In: *Phys. Rev. C* 48 (6 Dec. 1993), pp. 2731–2739. DOI: 10.1103/PhysRevC.48.2731. URL: https://link.aps.org/doi/10.1103/PhysRevC.48.2731.

[71] J. M. Udías et al. "Relativistic versus nonrelativistic optical potentials in A(e,e'p)B reactions". In: *Phys. Rev. C* 51 (6 June 1995), pp. 3246–3255. DOI: 10.1103/PhysRevC.51.3246. URL: https://link.aps.org/doi/10.1103/PhysRevC.51.3246.

[72] J. M. Udías et al. "Relativistic mean field approximation to the analysis of $^{16}\mathrm{O}(e,e'p)^{15}\mathrm{N}$ data at $|Q^2|lt;\ 0.4(\mathrm{GeV}/c)^2$". In: *Phys. Rev. C* 64 (2 July 2001), p. 024614. DOI: 10.1103/PhysRevC.64.024614. URL: https://link.aps.org/doi/10.1103/PhysRevC.64.024614.

[73] R. González-Jiménez et al. "Neutrino energy reconstruction from semi-inclusive samples". In: *Phys. Rev. C* 105 (2 Feb. 2022), p. 025502. DOI: 10.1103/PhysRevC.105.025502. URL: https://link.aps.org/doi/10.1103/PhysRevC.105.025502.

[74] A. Nikolakopoulos et al. "Benchmarking intranuclear cascade models for neutrino scattering with relativistic optical potentials". In: *Phys. Rev. C* 105 (5 May 2022), p. 054603. DOI: 10.1103/PhysRevC.105.054603. URL: https://link.aps.org/doi/10.1103/PhysRevC.105.054603.

[75] J. M. Franco-Patino et al. "Final state interactions in semi-inclusive neutrino-nucleus scattering: Applications to the T2K and MINERνA experiments". In: *Phys. Rev. D* 106 (11 Dec. 2022), p. 113005. DOI: 10.1103/PhysRevD.106.113005. URL: https://link.aps.org/doi/10.1103/PhysRevD.106.113005.

[76] J. M. Franco-Patino et al. *Study of semi-inclusive charged-current electron and muon neutrino scattering from ^{40}Ar in the energy range of the MicroBooNE experiment.* 2023. arXiv: 2304.01916 [hep-ex].

[77] W. Greiner. *Relativistic Quantum Mechanics. Wave Equations.* Springer, 2000. ISBN: 9783540674573. URL: https://books.google.es/books?id=2DAInxwvlHYC.

[78] L. Jiang et al. "Determination of the argon spectral function from $(e,e'p)$ data". In: *Phys. Rev. D* 105 (11 June 2022), p. 112002. DOI: 10.1103/PhysRevD.105.112002. URL: https://link.aps.org/doi/10.1103/PhysRevD.105.112002.

[79] Wang et al. "The AME2016 atomic mass evaluation (II). Tables, graphs and references". In: *Chinese Physics C* 41.3 (Mar. 2017), p. 030003. DOI: 10.1088/1674-1137/41/3/030003. URL: https://dx.doi.org/10.1088/1674-1137/41/3/030003.

[80] W.H. Dickhoff and C. Barbieri. "Self-consistent Green's function method for nuclei and nuclear matter". In: *Progress in Particle and Nuclear Physics* 52.2 (2004), pp. 377–496. ISSN: 0146-6410. DOI: https://doi.org/10.1016/j.ppnp.2004.02.038. URL: https://www.sciencedirect.com/science/article/pii/S0146641004000535.

[81] G.A. Rijsdijk, K. Allaart, and W.H. Dickhoff. "Hole spectral functions and collective excitations". In: *Nuclear Physics A* 550.1 (1992), pp. 159–178. ISSN: 0375-9474. DOI: https://doi.org/10.1016/0375-9474(92)91137-E. URL: https://www.sciencedirect.com/science/article/pii/037594749291137E.

[82] Claudio Ciofi degli Atti. "In-medium short-range dynamics of nucleons: Recent theoretical and experimental advances". In: *Physics Reports* 590 (2015), pp. 1–85. ISSN: 0370-1573. DOI: https://doi.org/10.1016/j.physrep.2015.06.002. URL: https://www.sciencedirect.com/science/article/pii/S0370157315003245.

[83] M. Duer et al. "Probing high-momentum protons and neutrons in neutron-rich nuclei". In: *Nature* 560 (Aug. 2018), pp. 617–621. DOI: 10.1038/s41586-018-0400-z. URL: https://doi.org/10.1038/s41586-018-0400-z.

[84] K. S. Egiyan et al. "Measurement of Two- and Three-Nucleon Short-Range Correlation Probabilities in Nuclei". In: *Phys. Rev. Lett.* 96 (8 Mar. 2006), p. 082501. DOI: 10.1103/PhysRevLett.96.082501. URL: https://link.aps.org/doi/10.1103/PhysRevLett.96.082501.

[85] E. D. Cooper et al. "Global Dirac phenomenology for proton-nucleus elastic scattering". In: *Phys. Rev. C* 47 (1 Jan. 1993), pp. 297–311. DOI: 10.1103/PhysRevC.47.297. URL: https://link.aps.org/doi/10.1103/PhysRevC.47.297.

[86] R. González-Jiménez et al. "Nuclear effects in electron-nucleus and neutrino-nucleus scattering within a relativistic quantum mechanical framework". In: *Phys. Rev. C* 100 (4 Oct. 2019), p. 045501. DOI: 10.1103/PhysRevC.100.045501. URL: https://link.aps.org/doi/10.1103/PhysRevC.100.045501.

[87] R. González-Jiménez et al. "Constraints in modeling the quasielastic response in inclusive lepton-nucleus scattering". In: *Phys. Rev. C* 101 (1 Jan. 2020), p. 015503. DOI: 10.1103/PhysRevC.101.015503. URL: https://link.aps.org/doi/10.1103/PhysRevC.101.015503.

[88] S. Boffi et al. "Orthogonality and the Perey factor in knockout reactions induced by electromagnetic probes". In: *Nuclear Physics A* 379.3 (1982), pp. 509–522. ISSN: 0375-9474. DOI: https://doi.org/10.1016/0375-9474(82)90011-2. URL: https://www.sciencedirect.com/science/article/pii/0375947482900112.

[89] J.I. Johansson, H.S. Sherif, and F. Ghoddoussi. "Orthogonality effects in relativistic models of nucleon knockout reactions". In: *Nuclear Physics A* 665.3 (2000), pp. 403–415. ISSN: 0375-9474. DOI: https://doi.org/10.1016/S0375-9474(99)00434-0. URL: https://www.sciencedirect.com/science/article/pii/S0375947499004340.

[90] Andrea Meucci et al. "Relativistic descriptions of inclusive quasielastic electron scattering: Application to scaling and superscaling ideas". In: *Phys. Rev. C* 80 (2 Aug. 2009), p. 024605. DOI: 10.1103/PhysRevC.80.024605. URL: https://link.aps.org/doi/10.1103/PhysRevC.80.024605.

[91] R. González-Jiménez et al. "Extensions of superscaling from relativistic mean field theory: The SuSAv2 model". In: *Phys. Rev. C* 90 (3 Sept. 2014), p. 035501. DOI: 10.1103/PhysRevC.90.035501. URL: https://link.aps.org/doi/10.1103/PhysRevC.90.035501.

[92] J. E. Amaro et al. "Relativistic analyses of quasielastic neutrino cross sections at MiniBooNE kinematics". In: *Phys. Rev. D* 84 (3 Aug. 2011), p. 033004. DOI: 10.1103/PhysRevD.84.033004. URL: https://link.aps.org/doi/10.1103/PhysRevD.84.033004.

[93] M. B. Barbaro et al. "Mean-field and two-body nuclear effects in inclusive electron scattering on argon, carbon, and titanium: The superscaling approach". In: *Phys. Rev. C* 99 (4 Apr. 2019), p. 042501. DOI: 10.1103/PhysRevC.99.042501. URL: https://link.aps.org/doi/10.1103/PhysRevC.99.042501.

[94] G. D. Megias et al. "Inclusive electron scattering within the SuSAv2 meson-exchange current approach". In: *Phys. Rev. D* 94 (1 July 2016), p. 013012. DOI: 10.1103/PhysRevD.94.013012. URL: https://link.aps.org/doi/10.1103/PhysRevD.94.013012.

[95] G. D. Megias et al. "Charged-current neutrino-nucleus reactions within the superscaling meson-exchange current approach". In: *Phys. Rev. D* 94 (9 Nov. 2016), p. 093004. DOI: 10.1103/PhysRevD.94.093004. URL: https://link.aps.org/doi/10.1103/PhysRevD.94.093004.

[96] C. Andreopoulos et al. "The GENIE neutrino Monte Carlo generator". In: *Nucl. Instrum. Meth.* A614.1 (2010), pp. 87–104. ISSN: 0168-9002. DOI: https://doi.org/10.1016/j.nima.2009.12.009. URL: https://www.sciencedirect.com/science/article/pii/S0168900209023043.

[97] Costas Andreopoulos et al. "The GENIE Neutrino Monte Carlo Generator: Physics and User Manual". In: (2015). arXiv: 1510.05494 [hep-ph].

[98] Luis Alvarez-Ruso et al. "Recent highlights from GENIE v3". In: *The European Physical Journal Special Topics* 230.24 (Dec. 2021), pp. 4449–4467. DOI: 10.1140/epjs/s11734-021-00295-7. URL: https://doi.org/10.1140%2Fepjs%2Fs11734-021-00295-7.

[99] Y. Hayato. "Neut". In: *Nuclear Physics B - Proceedings Supplements* 112.1 (2002), pp. 171–176. ISSN: 0920-5632. DOI: https://doi.org/10.1016/S0920-5632(02)01759-0. URL: https://www.sciencedirect.com/science/article/pii/S0920563202017590.

[100] Yoshinari Hayato and Luke Pickering. "The NEUT neutrino interaction simulation program library". In: *Eur. Phys. J. ST* 230.24 (2021), pp. 4469–4481. DOI: 10.1140/epjs/s11734-021-00287-7. arXiv: 2106.15809 [hep-ph].

[101] Yoshinari Hayato. "A neutrino interaction simulation program library NEUT". In: *Acta Phys. Polon. B* 40 (2009). Ed. by Arthur Ankowski and Jan Sobczyk, pp. 2477–2489.

[102] T. Leitner et al. "Electron- and neutrino-nucleus scattering from the quasielastic to the resonance region". In: *Phys. Rev. C* 79 (3 Mar. 2009), p. 034601. DOI: 10.1103/PhysRevC.79.034601. URL: https://link.aps.org/doi/10.1103/PhysRevC.79.034601.

[103] Tomasz Golan, Cezary Juszczak, and Jan T. Sobczyk. "Effects of final-state interactions in neutrino-nucleus interactions". In: *Phys. Rev. C* 86 (1 July 2012), p. 015505. DOI: 10.1103/PhysRevC.86.015505. URL: https://link.aps.org/doi/10.1103/PhysRevC.86.015505.

[104] N. Jachowicz et al. "Continuum random phase approximation approach to charged-current neutrino-nucleus scattering". In: *Phys. Rev. C* 65 (2 Jan. 2002), p. 025501. DOI: 10.1103/PhysRevC.65.025501. URL: https://link.aps.org/doi/10.1103/PhysRevC.65.025501.

[105] V. Pandey et al. "Low-energy excitations and quasielastic contribution to electron-nucleus and neutrino-nucleus scattering in the continuum random-phase approximation". In: *Phys. Rev. C* 92 (2 Aug. 2015), p. 024606. DOI: 10.1103/PhysRevC.92.024606. URL: https://link.aps.org/doi/10.1103/PhysRevC.92.024606.

[106] S. Dolan, G. D. Megias, and S. Bolognesi. "Implementation of the SuSAv2-meson exchange current 1p1h and 2p2h models in GENIE and analysis of nuclear effects in T2K measurements". In: *Phys. Rev. D* 101 (3 Feb. 2020), p. 033003. DOI: 10.1103/PhysRevD.101.033003. URL: https://link.aps.org/doi/10.1103/PhysRevD.101.033003.

[107] S. Dolan et al. "Implementation of the continuum random phase approximation model in the GENIE generator and an analysis of nuclear effects in low-energy transfer neutrino interactions". In: *Phys. Rev. D* 106 (7 Oct. 2022), p. 073001. DOI: 10.1103/PhysRevD.106.073001. URL: https://link.aps.org/doi/10.1103/PhysRevD.106.073001.

[108] Alexis Nikolakopoulos et al. *From inclusive to semi-inclusive one-nucleon knockout in neutrino event generators*. 2023. arXiv: 2302.12182 [nucl-th].

[109] I. Ruiz-Simo et al. "Relativistic model of 2p-2h meson exchange currents in (anti)neutrino scattering". In: *J. Phys. G* 44.6 (2017), p. 065105. DOI: 10.1088/1361-6471/aa6a06. arXiv: 1604.08423 [nucl-th].

[110] I. Ruiz-Simo et al. "Emission of neutron-proton and proton-proton pairs in electron scattering induced by meson-exchange currents". In: *Phys. Rev. C* 94.5 (2016), p. 054610. DOI: 10.1103/PhysRevC.94.054610. arXiv: 1606.06480 [nucl-th].

[111] I. Ruiz Simo et al. "Emission of neutron–proton and proton–proton pairs in neutrino scattering". In: *Phys. Lett. B* 762 (2016), pp. 124–130. DOI: 10.1016/j.physletb.2016.09.021. arXiv: 1607.08451 [nucl-th].

[112] Dieter Rein and Lalit M Sehgal. "Neutrino-excitation of baryon resonances and single pion production". In: *Annals of Physics* 133.1 (1981), pp. 79–153. ISSN: 0003-4916. DOI: https://doi.org/10.1016/0003-4916(81)90242-6. URL: https://www.sciencedirect.com/science/article/pii/0003491681902426.

[113] Ch. Berger and L. M. Sehgal. "Lepton mass effects in single pion production by neutrinos". In: *Phys. Rev. D* 76 (2007), p. 113004. DOI: 10.1103/PhysRevD.76.113004. arXiv: 0709.4378 [hep-ph].

[114] A. Bodek and U.K. Yang. "Modeling deep inelastic cross sections in the few GeV region". In: *Nuclear Physics B - Proceedings Supplements* 112.1 (2002), pp. 70–76. ISSN: 0920-5632. DOI: https://doi.org/10.1016/S0920-5632(02)01755-3. URL: https://www.sciencedirect.com/science/article/pii/S0920563202017553.

[115] K. Abe et al. "Characterization of nuclear effects in muon-neutrino scattering on hydrocarbon with a measurement of final-state kinematics and correlations in charged-current pionless interactions at T2K". In: *Phys. Rev. D* 98 (3 Aug. 2018), p. 032003. DOI: 10.1103/PhysRevD.98.032003. URL: https://link.aps.org/doi/10.1103/PhysRevD.98.032003.

[116] T. Cai et al. "Nucleon binding energy and transverse momentum imbalance in neutrino-nucleus reactions". In: *Phys. Rev. D* 101 (9 May 2020), p. 092001. DOI: 10.1103/PhysRevD.101.092001. URL: https://link.aps.org/doi/10.1103/PhysRevD.101.092001.

[117] X.-G. Lu et al. "Measurement of Final-State Correlations in Neutrino Muon-Proton Mesonless Production on Hydrocarbon at $<E_\nu> = 3$ GeV". In: *Phys. Rev. Lett.* 121 (2 July 2018), p. 022504. DOI: 10.1103/PhysRevLett.121.022504. URL: https://link.aps.org/doi/10.1103/PhysRevLett.121.022504.

[118] P. Abratenko et al. "Measurement of differential cross sections for ν_μ-Ar charged-current interactions with protons and no pions in the final state with the MicroBooNE detector". In: *Phys. Rev. D* 102 (11 Dec. 2020), p. 112013. DOI: 10.1103/PhysRevD.102.112013. URL: https://link.aps.org/doi/10.1103/PhysRevD.102.112013.

[119] P. Abratenko et al. "First Measurement of Differential Charged Current Quasielasticlike ν_μ-Argon Scattering Cross Sections with the MicroBooNE Detector". In: *Phys. Rev. Lett.* 125 (20 Nov. 2020), p. 201803. DOI: 10.1103/PhysRevLett.125.201803. URL: https://link.aps.org/doi/10.1103/PhysRevLett.125.201803.

[120] X.-G. Lu et al. "Measurement of nuclear effects in neutrino interactions with minimal dependence on neutrino energy". In: *Phys. Rev. C* 94 (1 July 2016), p. 015503. DOI: 10.1103/PhysRevC.94.015503. URL: https://link.aps.org/doi/10.1103/PhysRevC.94.015503.

[121] Stephen Dolan. "Exploring Nuclear Effects in Neutrino-Nucleus Interactions Using Measurements of Transverse Kinematic Imbalance from T2K and MINERvA". In: (2018). arXiv: 1810.06043 [hep-ex].

[122] Kajetan Niewczas and Jan T. Sobczyk. "Nuclear Transparency in Monte Carlo Neutrino Event Generators". In: *Phys. Rev. C* 100.1 (2019), p. 015505. DOI: 10.1103/PhysRevC.100.015505. arXiv: 1902.05618 [hep-ex].

[123] S. Dolan et al. "Sensitivity of the upgraded T2K Near Detector to constrain neutrino and antineutrino interactions with no mesons in the final state by exploiting nucleon-lepton correlations". In: *Phys. Rev. D* 105 (3 Feb. 2022), p. 032010. DOI: 10.1103/PhysRevD.105.032010. URL: https://link.aps.org/doi/10.1103/PhysRevD.105.032010.

[124] P. A. Rodrigues et al. "Identification of nuclear effects in neutrino-carbon interactions at low three-momentum transfer". In: *Phys. Rev. Lett.* 116 (2016). [Addendum: Phys.Rev.Lett. 121, 209902 (2018)], p. 071802. DOI: 10.1103/PhysRevLett.116.071802. arXiv: 1511.05944 [hep-ex].

[125] P. Abratenko et al. "Differential cross section measurement of charged current ν_e interactions without final-state pions in MicroBooNE". In: *Phys. Rev. D* 106 (5 Sept. 2022), p. L051102. DOI: 10.1103/PhysRevD.106.L051102. URL: https://link.aps.org/doi/10.1103/PhysRevD.106.L051102.

[126] P. Abratenko et al. "Multi-Differential Cross Section Measurements of Muon-Neutrino-Argon Quasielastic-like Reactions with the MicroBooNE Detector". In: (2023). DOI: 10.48550/arxiv.2301.03700. URL: https://arxiv.org/abs/2301.03700.

[127] Taber De Forest. "Off-shell electron-nucleon cross sections: The impulse approximation". In: *Nuclear Physics A* 392.2 (1983), pp. 232–248. ISSN: 0375-9474. DOI: https://doi.org/10.1016/0375-9474(83)90124-0. URL: https://www.sciencedirect.com/science/article/pii/0375947483901240.

[128] Taber de Forest. "Inelastic nuclear electron scattering in the independent particle model". In: *Nuclear Physics A* 132.2 (1969), pp. 305–321. ISSN: 0375-9474. DOI: https://doi.org/10.1016/0375-9474(69)90486-2. URL: https://www.sciencedirect.com/science/article/pii/0375947469904862.

[129] J. J. Kelly. "Simple parametrization of nucleon form factors". In: *Phys. Rev. C* 70 (6 Dec. 2004), p. 068202. DOI: 10.1103/PhysRevC.70.068202. URL: https://link.aps.org/doi/10.1103/PhysRevC.70.068202.

[130] I. S. Towner and J. C. Hardy. "Currents and their couplings in the weak sector of the standard model". In: *Symmetries and Fundamental Interactions in Nuclei*. World scientific, Oct. 1995, pp. 183–249. DOI: 10.1142/9789812831446_0007. URL: https://doi.org/10.1142%2F9789812831446_0007.

[131] J.A. Caballero, T.W. Donnelly, and G.I. Poulis. "Scattering of polarized electrons from polarized targets: Coincidence reactions and prescriptions for polarized half-off-shell single-nucleon cross sections". In: *Nuclear Physics A* 555.4 (1993), pp. 709–751. ISSN: 0375-9474. DOI: https://doi.org/10.1016/0375-9474(93)90503-P. URL: https://www.sciencedirect.com/science/article/pii/037594749390503P.

[132] A.S Raskin and T.W Donnelly. "Polarization in coincidence electron scattering from nuclei". In: *Annals of Physics* 191.1 (1989), pp. 78–142. ISSN: 0003-4916. DOI: https://doi.org/10.1016/0003-4916(89)90337-0. URL: https://www.sciencedirect.com/science/article/pii/0003491689903370.

[133] Robert J. Perry. "Effects of the Dirac sea on finite nuclei". In: *Physics Letters B* 182.3 (1986), pp. 269–273. ISSN: 0370-2693. DOI: https://doi.org/10.1016/0370-2693(86)90088-2. URL: https://www.sciencedirect.com/science/article/pii/0370269386900882.

[134] P.G. Reinhard et al. "Nuclear ground-state properties in a relativistic Meson-Field theory". In: *Z. Physik A-Atomic nuclei* 323 (Mar. 1986), pp. 13–15. DOI: 10.1007/BF01294551. URL: https://doi.org/10.1007/BF01294551.

[135] Suk-Joon Lee et al. "Relativistic Hartree Calculations for Axially Deformed Nuclei". In: *Phys. Rev. Lett.* 57 (23 Dec. 1986), pp. 2916–2919. DOI: 10.1103/PhysRevLett.57.2916. URL: https://link.aps.org/doi/10.1103/PhysRevLett.57.2916.

[136] M.M. Sharma, M.A. Nagarajan, and P. Ring. "Rho meson coupling in the relativistic mean field theory and description of exotic nuclei". In: *Physics Letters B* 312.4 (1993), pp. 377–381. ISSN: 0370-2693. DOI: https://doi.org/10.1016/0370-2693(93)90970-S. URL: https://www.sciencedirect.com/science/article/pii/037026939390970S.